THEORETICAL STUDIES OF STRUCTURAL, ELECTRONIC AND OPTICAL PROPERTIES OF AMORPHOUS CHALCOGENIDE MATERIALS

A dissertation presented to

the faculty of

the College of Arts and Sciences of Ohio University

In partial fulfillment

of the requirements for the degree

Doctor of Philosophy

Xiaodong Zhang

March 2001

THEORETICAL STUDIES OF STRUCTURAL, ELECTRONIC AND OPTICAL PROPERTIES OF AMORPHOUS CHALCOGENIDE MATERIALS

BY

XIAODONG ZHANG

This dissertation has been approved

for the Department of Physics

and the College of Arts and Sciences by

David Drabold
Associate Professor of Physics

Leslie A. Flemming
Dean, College of Arts and Sciences

XIAODONG ZHANG, Ph.D. March 2001. Physics

THEORETICAL STUDIES OF STRUCTURAL, ELECTRONIC AND OPTICAL PROPERTIES OF AMORPHOUS AMORPHOUS CHALCOGENIDE MATERIALS

(193 pp.)

Director of Dissertation: David Drabold

In this thesis, we have presented structural models of elementary chalcogenide amorphous material, *a*-Se, binary glassy surface, *g*-$GeSe_2$ surface and tertiary amorphous materials *a*-$Ge_{0.2}As_{0.4}Se_{0.4}$ through *ab initio* molecular dynamic simulation. *a*-Se model and *g*-$GeSe_2$ models are by far the best models yet presented through the *ab initio* molecular dynamic simulation as evidenced by the uniform agreement with all the structural properties such as pair correlation function, static structure factors, vibrational spectrum and electronic density of state. We made a first try on the tertiary glassy $Ge_{0.2}As_{0.4}Se_{0.4}$ and obtained a reasonable structural model of this very complex tertiary amorphous material. For the *a*-Se, we unambiguously show that valence alternation , i.e., negative U, is the major mechanism to explain the exotic properties of *a*-Se. For the *g*-$GeSe_2$ surface, we show that ring formation is the major mechanism for the surface reconstruction. Through defect analysis of the bulk *g*-$GeSe_2$, *g*-$GeSe_2$ surface, bulk $Ge_{0.2}As_{0.4}Se_{0.4}$, we show that more than 30% of defects in those model can still make electronic structure of those materials have no mid-gap states. We also show that valence alternation is one of the possible mechanism for the nature to allow so many defects exist in the binary and tertiary chalcogenide glasses.

Having a reliable structural model available, we are able to study how this chalcogenide glass responds to light illumination from first principle. Using the 64- and 216-atom a-Se model we built, we show how light selectively attacks the defect sites in the materials. We describe the bond switching and rearrangement by the photo-excitation and explain the physical mechanism of the photo-structural change. We also show the possibility of fine-tuning the structure of the a material through light excitation. We further link our MD simulation to the recent experiment by Kolobov et al. [8] to explain the physical mechanism of the dynamical bond formation observed experimentally.

Approved _____

Associate Professor of Physics

For my wife, father and mother

Acknowledgments

I would like to express my thanks and appreciation to all the people who helped me throughout my academic career. I would especially like to thank my advisor, Dr. David Drabold, for his four years of continual patience, warmth, guidance, and perseverance. I was extremely lucky to find an advisor with a considerable patience and tolerance on his student. Dr. Drabold was so kind to give me the freedom to follow my own research path and correct my research direction when I was stuck somewhere.

I was encouraged with helpful discussions and hospitality from Prof. Normand Mousseau and Prof. Ron Cappeletti for their inputs to this dissertation. Their insight and experience were invaluable in the completion of this work.

I would also like to acknowledge my intern mentor Dr. Alex Demkov at Motorola INC. His sincere attitude and hands-on guidance benefit me a lot on my academic career.

I wish to thank Ohio University for giving me a supportive environment to study and do research, especially the physics department where I have received much encouragement from faculty, staff, and peers.

I am fortunate to have had my parents who educated me to be an honest and responsible man. Their support of my pursuit of science is the major source for me to attaining my goals. Most of all, I would like to thank my wife Xiaochun Wang for her love, encouragement, and support throughout this endeavor.

Contents

List of Tables

List of Figures

Chapter 1

Introduction

1.1 Chalcogenide Amorphous Materials

1.1.1 Classification of Amorphous Materials

Semiconductors are used in a wide variety of applications. Most practically useful semiconductors are made from crystalline materials. However, some non-crystalline materials also have useful semiconducting properties. There are two classes of amorphous semiconductors most commonly investigated: amorphous germanium, silicon and carbon with tetrahedral coordination and also amorphous semiconductors containing one or more of the chalcogenide elements, S, Se or Te. For tetrahedral

amorphous materials, the covalent network is macroscopically extended in three dimensions. In other words, paths of covalent bonds connect every atoms with every other atom in a macroscopic sample of the material. However, some solids are representable by disconnected covalent networks: they are molecular solids. Molecular solids are characterized by the coexistence of strong (primarily covalent) and weak (intermolecular, primarily "var der Waals") forces [1]. The chalcogen crystal materials are notable among the molecular solids. It is very important to notice that molecular solids are naturally classified into several distinct categories on the basis of the molecular network dimensionality. Zallen defined the network dimensionality as the number of dimensions in which the covalently bonded molecular unit is macroscopically extended. According to this definition, the zero-dimensional-network materials, for example S_8 and Se_8 etc, form the largest and most familiar class of molecular solids. The trigonal Se is one of the most famous one-dimensional-network crystals. Two-dimensional-network molecular solids include As_2Se_3 etc.

1.1.2 Special Characteristics of Chalcogenide Amorphous Materials

The properties of amorphous tetrahedral materials such as *a*-Si and *a*-Ge are well studied due to technological application. For example, laptop computer displays are all using *a*-Si:H TFTs these days. The best structural model is constructed using

the modified version of Wooten, Winer and Weaire's bond switching scheme[2, 3]. For a-Si or a-Ge model, it is generally accepted that these amorphous materials still preserve nearly perfect bonding or coordination. Almost everyone recognizes the dangling bond as the most important defect in a-IV material. It has a net spin and is a paramagnetic centre; in pure a-Si there are perhaps 10^{18} to 10^{20} cm^{-3} of them [4].

In chalcogenide glasses, as in a-IV materials, there are defects, but their nature and the properties they give rise to are different. There is evidence from electronic and optical phenomena that chalcogenide glasses have a significant density of gap states with E_F pinned near the center of the optical gap. Singly occupied states near E_F would be expected but no ESR or paramagnetism confirms their presence. A first attempt to give a model that pins the Fermi energy without producing unpaired spins was made by Anderson[5]. He suggested that the correlation energy required to overcome the mutual repulsion could be more than compensated by some other adjustment such as energetically favorable displacement of atoms. This was expressed in an effective Hubbard U which was attractive between electrons of opposite spin at a particular bonding location. Supported by Anderson's hypothesis of an effective electron-electron attraction in system with a strong degree of electron-phonon coupling, Street and Mott [6] argued that the negative U_{eff} results from the formation of an extra bond when an electron is removed from a dangling bond. This extra

bond is sufficient to overcome the Coulomb repulsion resulting from the addition of an extra electron to a different dangling bond. The dangling bond (DB) model of Street and Mott was highly successful in explaining many experimental results. However, the DB model could not explain why a large negative U_{eff} is needed for chalcogenide glasses, but does not ordinarily exist in amorphous tetrahedral bonded materials, which are found to contain high densities of spins. Kastner, Adler and Fritzsche(KAF) [7] made a step further and considered both the defect and those orbitals on its neighbors that participate in the chemical bond with the defect. In KAF model, it was assumed that the lowest-energy neutral defect is the three-fold coordinated atom C_3^0. It is an essential feature of this model that even the C_3^0 will spontaneously change by the exothermic reaction

$$2C_3^0 \rightarrow C_3^+ + C_1^- \tag{1.1}$$

which represents a bonding rearrangement into an associated, electrostatically attracting pair of defects C_3^+ and C_1^- called a valence-alternation pair(VAP). It has also been proposed that intimate pair (IVAP) for which the Coulomb attraction exists between positive and negative nearest neighbors may be energetically stable. Since the defect states involved are either doubly occupied or unoccupied, these defects do not carry a net spin. This explains why the low-temperature material is diamagnetic. The paramagnetic behavior at medium exists temperature is presumed

to arise from the electronic excitation of C_1^- and C_3^+ defects to form neutral C_1^0 and C_3^0 defects carrying net spins. The unusual properties of lone-pair semiconductors such as reversible photostructural changes, photoinduced diffusion, crystallization, phase separation and decomposition are all believed to be strongly connected to the bond switching and the chemical reactivity associated with the photoexcited VAP's. The VAP model has been verified by some experiments and especially the most recent electron spin resonance (ESR) experiment by Kolobov [8] gave the direct experimental evidence for the negative-U centers and valence alternation in amorphous selenium.

1.2 Methods to Generate Models Amorphous Materials

1.2.1 Properties of Realistic Models

One can not get very far along the road to understanding the properties of the materials without confronting the problem of the nature of the detailed structure of the material in question. For an amorphous solid, the essential aspect with which its structure differs with respect to that of a crystalline solid is the *absence of long-range order.* There is no translational periodicity. However, the amorphous solid

shows a high degree of local spatial or topological correlation. For most amorphous materials, each atom has the same number of nearest neighbors with nearly the same local structure as some crystalline phase. Thus, while lack of the long-range order in glasses implies randomness at large separations, the atomic scale structure is highly nonrandom for a few interatomic distances about any given atom. The lack of long-range order makes it very hard to extract atomistically detailed structural information about amorphous solids from diffraction experiments. Meanwhile, people believe that: (1) continuous random network(CRN) is appropriate to the structure of the covalent glasses; (2) random close packing is appropriate to the structure of simple metallic glasses; (3) random coil model is appropriate to the structure of polymeric organic amorphous materials. Although these models are idealizations, they represent the characteristic atomic structure of the main classes of amorphous solids. As Zallen indicated [1], this aspect of amorphous solids belongs in the realm of what may properly be called stochastic geometry.

1.2.2 WWW method

The most successful CRN model of amorphous material is the amorphous silicon model generated by using a modified version of Wooten, Winer and Weaire bond switching scheme[2]. The method generally involves the following steps: (1) randomize a crystalline network sufficiently so that subsequent annealing will not lead the

system back to the crystalline state; (2) perform the local rearrangement of bonds through "bond switching" to find the optimal structure of the amorphous materials in conjunction with (3) the simulated annealing scheme to prevent the system getting stuck in an unphysical local minimum. The WWW method is very successful in generating the amorphous tetrahedral models. An excellent *a*-Si model currently available is the 4096 atom model [9] generated by Djordjevic and Thorpe using the WWW method. Barkema and Mousseau recently used a variation of WWW approach and present 1000-atom and 4096-atom configurations with a degree of strain significantly less than the best computer generated CRN available at the moment and comparable to experimental results. [3] Very recently, Tu et al. extended the WWW method to study the *a*-SiO_2[10] and SiO_2/Si interface [11].

1.2.3 Molecular Dynamics Simulation

Although WWW method achieved large success in generating amorphous solids, the method now is only limited to the case of amorphous tetrahedral materials and the process of forming CRN model is *not* the physical glass forming process. The "standard" method to generate the amorphous materials is molecular dynamics (MD), where atoms are represented by point particles and the classical (Newton) equations of motion are integrated numerically. The molecular dynamic simulation superficially mimics the process of making amorphous materials experimentally. The

basic procedure for molecular dynamic process is so called "cook and quench" process. Usually one melts a crystal material at high temperature so that the system totally forgets its crystalline origin. Then one perform a simulated annealing process to bring the system to energy minimum state. Depending on the complexity of interaction, the molecular dynamic simulation is roughly classified into three categories: classical, tight-binding and *ab initio* molecular dynamic simulation.

Classical Molecular Dynamics Simulation

In classical molecular dynamics simulations, the classical interatomic potentials are used to crudely approximate the true quantum mechanical potentials since classical forces can be rapidly evaluated. State of the art classical molecular dynamics scheme can calculate the atoms with size up to multimillion atoms. Vashishta et al. [13, 14] constructed meaningful models of glassy $GeSe_2$ and other amorphous materials.

Tight-binding Molecular Dynamics Simulation

Tight-binding molecular dynamics (TBMD) is designed to run moderate molecular dynamics simulation within the *semi-empirical tight-binding* scheme. The electronic structure of the simulated system is calculated by a TB hamiltonian so that the quantum mechanical many-body nature of the interatomic forces is naturally

taken into account. Sankey and Allen used a tight binding Hamiltonian to do MD *first* in 1986 [12]. The best order N TBMD code now can calculate with size up to several thousand atoms.

Ab initio Molecular Dynamics Simulation

In mid eighties, Car and Parrinello [15] showed how to combine the accuracy of *ab initio* density functional methods with force calculations and molecular dynamics techniques. In *ab initio* MD, the nuclei are treated as classical particles which move in a potential determined by the atomistic force calculated by the density functional theory due to Kohn, Hohenberg and Sham [16]. Now, the state of art MD simulation can be applied for several hundred atoms. For *ab initio* method, the only information which must be provided are the atomic numbers and positions of the atoms within the system. In contrast, empirical or semi-empirical approaches require a model of the interactions between the atoms to be supplied. The parameters of these models are usually derived by fitting the outcome of simulations to experimental data. Problems with these techniques arise when one considers the range of their applicability. If the parameters of the models were derived from system A, what guarantee is there that they apply to system B with different chemical bonding and/or topology? In a disordered environment, it is very hard to find a universal set of parameters for the classical or semi-classical potentials. As a result, large

numbers of fitting parameters are usually needed for either empirical potentials or tight-binding models. In this respect, *ab initio* MD in which the interatomic potential is determined by the electronic structure of the system is the method of choice to model complex amorphous materials.

1.2.4 Computer Science Aspects

In terms of combinatorial optimization, constructing the amorphous materials can be regarded as the minimization of the energy functional of the atomic system. Of course, a crystalline structure is definitely the energy minimum state. However, once the system is completely randomized, the probability of returning to the crystal structure via simulation is essentially zero. In most cases, the system will reach to an amorphous local minimum state during the minimization process. We can formulate the problem of *searching the crystal structure from a random configuration* as *selecting the best structure from the possible conformations the number of which is exponentially increasing with the size of the system.* So, in terms of computational science, this problem is NP hard problem. Here, the NP means non-deterministic polynomial time. It is generally accepted that NP hard problem can not be exactly solved by the polynomial time algorithm. One of the famous example of NP hard problem is the traveling salesman problem (TSP)[18]. Although it has not been shown that constructing the amorphous materials is a NP hard problem or

not, some methods used to build the amorphous materials is very similar to some approximation algorithms for solving the NP hard problems.

Similarity between the n-opt algorithm of TSP problem with WWW bond-switching scheme

Since NP hard problem cannot be exactly solved, various approximation algorithms were proposed to get approximate solution of the problem. One of the famous examples is to use the 2-opt and 3-opt algorithm combined with simulated annealing to solve the TSP problem [19]. In the TSP problem, we are given a set of cities and for each pair of distinct cities i, j a distance d_{ij}, the problem is to find an ordering of the cities to minimize the tour which only visited each cities exactly once. The 2-opt operation first deletes two edges thus breaking the tour into two paths, then reconnects those paths in the other possible way. This operation is exactly equivalent to the bond switching scheme used by the WWW method to constructing the *a*-Si. Of course, simulated annealing scheme is used to guide the system to the optimization state. The 2-opt and 3-opt algorithms are one of the most successful approximation algorithm for the TSP problem. In some sense, WWW method is also one of the most successful method to model the *a*-Si. The possible reason for the success of this kind of heuristic local search algorithm is that this kind of algorithm provides a way for system to visit some "rare" events in reasonable time.

Activation Relaxation Technique

As we know, the major problem of the MD method to model the amorphous materials is that most of the computer time is spent in following local vibrations, waiting for the infrequent bond-switching events because there is a large barrier to breaking and reforming bonds in these systems. The structure produced by the MD simulation can be regarded as a local minimum state of unphysically high energy. Due to the cost of the *ab initio* MD simulation, it is usually not affordable for the simulation to wait for the system to get out of this local minimum. Realizing this problem, Mousseau and Barkema [20] proposed the activation-relaxation technique (ART) to focus on significant changes in the microscopic structure (events). The ART technique allows the system to evolve following well-defined paths between local energy minima. The activation step involves moving the configuration from one local minimum to a local saddle-point and the system will be relaxed to another local minimum state.

The ART technique has already been applied with considerable success to *a*-Si, *v*-SiO_2 and other systems. The reason for the success of ART technique is that it provides an especially effective way to get out of the local minimum during the combinatorial optimization problem. However, up to now, ART technique has employed only a classical interatomic potential. We can foresee that this technique

will be combined with density functional theory to make an even larger impact on modeling amorphous materials.

1.3 Photo Structural Change

There is a fascinating range of phenomena connected with light exposure which occurs in glasses, especially the chalcogens (S, Se, Te), either in elemental form or alloyed with atoms from columns III, IV or V. Some of the most important light-induced processes include: photofluidity "photomelting" of certain chalcogenide glasses such as *a*-Se[22] and *g*-As_2S_3[24]; in which weak light (even sub gap) shone on the glass leads to a viscosity change of *several* orders of magnitude. This process has been demonstrated to *not* be a thermal heating effect (in As_2S_3 for example the effect is *larger* at lower temperatures[24]). There is also the related property of giant photoexpansion[25]; large volume changes in light-exposed thin films; some chalcogenide films change thickness when light-soaked by *several percent*. A final light-induced effect is the well known phenomenon of photodarkening[26] (contraction of the optical gap with light soaking). The understanding of these effects is at present extremely incomplete and unknown in disordered forms of matter. Closely associated with the light-induced effects are the structural changes which acrue from light exposure. In some cases it is plausible that this is a local phenomenon in accordance with accepted models. On the other hand, photomelting and giant

photoexpansion are manifestly nonlocal and there is no atomistic understanding of these unique effects.

More recently, Poborchil et al. [22] reported that trigonal and amorphous selenium can be melted by illumination with bandgap light at a temperature of ~77K. The photo-melting phenomenon is pure optical (athermal) and is associated with light-induced breaking of the interchain (intermolecular) bonds in selenium. It is known from several other experiments[23] that surface chemistry can sometimes affect the photo-induced changes (especially light-induced oxidation at a surface layer). To our knowledge there have been very few if any studies of amorphous surfaces of a any kind. Clearly a microscopic model of these glass surfaces is required to study surface reactivity.

1.4 The Major Issues of Our Work

A systematic understanding of the structural, electronic and vibrational properties of chalcogenide amorphous materials, the method of making the amorphous materials and the mechanism of light induced effects are the major tasks in this thesis. Of course, it is not possible to solve all the details of those important problems. But we will make some significant contribution to these problems.

1.4.1 Valence Alternation Model

For the properties of chalcogenide materials, we will put our focus on the valence alternation model. For *a*-Se, the VAP defect can be formed by the transfer of an electron from one dangling-bond selenium to another:

$$2Se^0(z=1) + U_{eff} \rightarrow Se^+(z=3) + Se^-(z=1), \tag{1.2}$$

where z refers to coordination. In the above reaction, there is an e^2/r_{12} potential energy cost which is the price to pay for bringing an electron (initially alone in a nonbonding orbital on another chain-end atom) to join its lone-pair partner on the chain-end atom which receives the electron and becomes Se^-. However, there is also an energy benefit which occurs as a consequence of the bond switching that takes place around the Se which supplied the electron and becomes Se^+, eager to form three bonds. The bond switching (actually, bond formation) converts two non-bonding electrons into bonding electrons, thus lowering their energy substantially. It is possible, therefore, that the net energy cost U_{eff} be negative. This is believed to be the case for multicomponent chalcogenide glasses[1]. The VAP defects would be those lowest in energy relative to the ideal CRN covalent network. Because of the low creation energy, a large concentration of these defects should be present

in thermodynamic equilibrium at T_g and these native defects would be frozen in during the melt-quenching formation of the glass.

The negative U_{eff} and VAP model for chalcogenide amorphous materials has been known for almost 30 years [7]. Even now, there are debates on this issue [27]. In our work, we explicitly show that valence alternation model is the key to understanding most of the special phenomena of the amorphous selenium. Staring from a random configuration, we construct a 64 atom amorphous selenium model [28] which contains only one IVAP defect without any *a priori* knowledge of the structure of *a*-Se. This model is consistent with valence alternation pair hypothesis both structurally and electronically. Further, we studied the electronic structure and defect structure of the amorphous $GeSe_2$ surface, the electronic structure at the band edge of this binary chalcogenide $GeSe_2$[31] glass still shows the characteristic of valence alternation pair defect. Even for a tertiary chalcogenide glass we recently constructed [32], the electronic structure can still be described by the valence alternation model.

1.4.2 Modeling Methodology

It is sometimes implied that employing the "best" Hamiltonian (eg most realistic interatomic interaction) leads automatically to the best structural model. The work of Djordjevic, Thorpe and Wooten[9] and Mousseau and Barkema[20] has made it

clear that a thoroughly program of annealing and thoroughly probing configuration space is more important than having the most accurate Hamiltonian. In particular, a simple Keating[21] potential leads to the most realistic (that is, agreeing with all the experiments) models of *a*-Si in existence in large part because the scheme constrains the final model to be four-fold coordinated, as strongly suggested by experiments. No cell formed with empirical or *ab initio* MD is as accurate for electronic structure simply because the *a priori* information about four-coordination is not externally imposed (and MD cannot work this out for itself in part because of short time scales). Also, accurate *ab initio* methods are typically unable to directly provide a model as large as 1000 atoms, which is necessary for some studies (particularly of band tail states).

WWW and the ART approach achieves great success in constructing tetrahedral amorphous materials but people have not proposed a comparable bond switching scheme for amorphous selenium and it is also not known whether ART can show the same success for chalcogenide amorphous materials. Current ART computational technique for modeling amorphous materials has not advanced to the glassy chalcogenide amorphous, but good structural model of chalcogenide material is required to understand the unusual properties of those materials. Realizing that imposing the *a priori* information is the key to the success of the WWW, we think we could impose this *a priori* information when building *a*-Se.

In our approach, we first use a "random walk" algorithm to build a selenium chain in which every atom is two-fold coordinated. Then we use an *ab initio* molecular dynamic approach to anneal and quench the initial system with the *a priori* information built in. We made a 216 atom model[29] with only one VAP defect. The pair correlation function, static structure factor, vibrational density of state and electronic structure are simultaneously in agreement with experiments. For the tertiary chalcogenide glass, even the *a priori* information about the preferred bonding of each species of the atom is not exactly known, we first use the *ab initio* MD to thoroughly anneal a small cell, and then use the knowledge of this small cell to build a large network. We obtained the satisfactory result for the pair correlation function and static structural factor of the tertiary chalcogenide glasses $Ge_{0.2}As_{0.4}Se_{0.4}$ and $AsGe_{0.8}Se_{0.8}$ [32]. We hope in the future, we can combine the ART technique with our *ab initio* MD to realistically model tertiary chalcogenide glasses.

1.4.3 Light Induced Effects

For chalcogenide glasses, insight into the microscopic origin of the light induced effects emerged in the seventies and eighties thanks to the work of several authors[33, 6, 34, 7, 35, 36, 37]. It is quite impressive how much progress can be made without detailed microscopic calculations. For a proper discussion of the experimental and theoretical situation, we recommend the review of Shimakawa[38] and coworkers.

We use a quite unique approach to simulate the light-induced effects in amorphous materials. The approach was first proposed by Drabold et al [39] to study the consequences of light-induced occupation changes on amorphous Si. In our approach, the photo excitation was simulated by transferring the electron occupied at the highest occupied molecular level (HOMO) to the lowest unoccupied molecular level (LUMO) during the MD simulation. This change in the charge of a localized state is imagined as a simple model of an electron ejected from the valence band to the conduction band by the photon. Using this approach, we did the first *ab initio* calculation of photostructural effects in a glass [29]. We showed that the major structural change for the *a*-Se occurs near the defect sites and that the photo excitation will anneal the defect or cause the defect diffusion. Latter, we also investigated the physical mechanism of dynamical bond formation, light-created defect centers and fast-slow components in the amorphous selenium observed in the experiment [30]. It is now possible to use the *ab initio* MD to directly explain the experiment at the atomistic level.

1.5 Organization of Dissertation

The work is organized according to the following scheme: In Chapter 2 we give a detailed description of the density functional theory, pseudo-potential method,

Mulliken charge analysis, property of the density functional in the LDA hamiltonian. In Chapter 4 we show various form of structure factor and pair correlation function for analysis of the properties of amorphous materials. In Chapter 5, taking elemental selenium as an example, we show how to use the density functional methods to study the crystal structure and electronic band structure of crystal selenium. We also describe the structural, vibrational, and electronic properties of a 64 atom a-Se model and 216 atom a-Se model. Chapter 6 introduces the method of simulating the photo-structural change by the *ab initio* MD simulation. We describe the bond switching and rearrangement by the photo-excitation and explain the physical mechanism of the photo-structural change. We further link our MD simulation to the recent experiment by Kolobov et al. [8] to explain the physical mechanism of the dynamical bond formation. We also explore a new application of the "photo excitation" method: photo-assisted surface reconstruction. We show that it is possible to explore some new reaction channels by the photo-excitation. In Chapter 7 we study the structural, electronic properties of binary chalognenide glass $GeSe_2$. For this binary glass, we put our focus on the surface construction for amorphous materials. We made the first glass surface by the *ab initio* MD simulation. Especially, the FSDP in the concentration-concentration structure factor is observed in both our bulk model and surface model. We explicitly show that the ring formation is the major mechanism in this surface reconstruction. In Chapter 8 we describe a method to construct the tertiary chalcogenide glass $Ge_{0.2}As_{0.4}Se_{0.4}$ and

$AsGe_{0.8}Se_{0.8}$. This is a very challenging project and a good structural model has never been reported before. But the pair correlation function and structural properties in our model gives a satisfactory agreement with experiment. Our preliminary models give the gap width around 0.8 eV. Through the study of the a-Se, g-$GeSe_2$ surface, g-$Ge_{0.2}As_{0.4}Se_{0.4}$, we found that valence alternation model plays important roles in understanding the electronical properties of those chalcogenides materials. We believe our study gives the first systematic evidence of the valence alternation, negative-U of chalcogenide material at the atomistic level. The concluding remarks are given in Chapter 9.

Chapter 2

Theoretical Foundation

2.1 Density Functional Theory

Density Functional Theory (DFT) is based on the notion of the single particle electron density as a fundamental variable. The Hohenberg-Kohn Theorem[16] states that for any system of electrons in an external potential $V_{ext}(\vec{r})$, the Hamiltonian is fully determined by the ground state density. As a consequence, if the ground state density is determined, ground state properties of the system such as total energies, equilibrium positions or magnetic moments are completely determined. The ground state electron density $n_0(\vec{r})$ is determined by minimizing the

energy functional

$$E[n(\vec{r})] = F[n(\vec{r})] + \int n(\vec{r}) V_{ext}(\vec{r}) d^3r \tag{2.1}$$

where

$$F[n(\vec{r})] = < \Psi | (\hat{T} + \hat{V}_{ee}) | \Psi > \tag{2.2}$$

is a *universal* functional in the sense that that does not depend on the external potentials and

$$V_{ext}(\vec{r}) = -\sum_{\alpha} \frac{Z_\alpha}{|\vec{r} - \vec{R}_\alpha|} + \frac{1}{2N} \sum_{\alpha\beta} \frac{Z_\alpha Z_\beta}{|\vec{R}_\alpha - \vec{R}_\beta|} \tag{2.3}$$

is the external potential which contains the contribution of electron-ion interactions and ion-ion interactions. Ψ is the unknown many electron wave function. $\vec{R}_\alpha$ is the position of αth ion. This is an *exact* result. Unfortunately, the proof of the Hohenberg-Kohn theorem is not constructive, hence the form of the functional $F[n(\vec{r})]$ in Equation 2.1 is not known. $F[n(\vec{r})]$ may be decomposed as

$$F[n] = T[n] + U_H[n] + E_{xc}[n]. \tag{2.4}$$

In equation 2.4, T[n] is written in a form for noninteracticing electron. The Hartree term $U_H[n]$ may be written as

$$U_H[n(\vec{r})] = \frac{e^2}{2} \int \int \frac{n(\vec{r}) n(\vec{r'})}{|\vec{r} - \vec{r'}|} d^3r d^3r' \tag{2.5}$$

but the expressions for the kinetic energy, T, and the exchange-correlation energy E_{xc}, are not obvious functionals of n in the way U_H is. The simplest approximation to the kinetic term comes from Thomas Fermi theory [17]

$$T[n] = \gamma \int n(\vec{r})^{\frac{5}{3}} d\vec{r} \tag{2.6}$$

but this treatment of the kinetic energy is not accurate and even the shell structure of atoms is not reproduced properly.

2.1.1 The Kohn-Sham scheme

Kohn and Sham provided a paradigm for treating the kinetic term by introducing a set of orthonormal orbitals as a basis for the charge density:

$$n(\vec{r}) = 2 \sum_i |\psi_i(\vec{r})|^2 \tag{2.7}$$

where $\psi_i(\vec{r})$ is the Kohn-Sham orbital. These orbitals are only employed as a tool for expanding the charge density and strictly speaking cannot be interpreted as the single particle states. However, there are many computations that show that the Kohn-Sham orbitals can be useful[102]. The kinetic energy (T_s) expressed by the

Kohn-Sham orbitals may be written

$$T_s[n(\vec{r})] = \sum_i -\frac{\hbar^2}{2m_e} \int \psi_i^* \bigtriangledown^2 \psi_i d^3\vec{r}, \tag{2.8}$$

By introducing the Kohn-Sham orbitals, we can first solve the following set of Schrödinger-like equations

$$\left(-\frac{\hbar^2}{2m_e} \bigtriangledown^2 + V_{eff}(\vec{r})\right) \psi_i(\vec{r}) = \epsilon_i \psi_i(\vec{r}) \tag{2.9}$$

where V_{eff} is an effective potential

$$V_{eff}(\vec{r}) = V_{ext}(\vec{r}) + \int \frac{e^2 n(\vec{r'})}{|\vec{r} - \vec{r'}|} d^3r' + V_{XC}(\vec{r}) \tag{2.10}$$

and

$$V_{XC}(\vec{r}) = \frac{\delta E_{XC}}{\delta n(\vec{r})} \tag{2.11}$$

is the exchange-correlation potential. The set of Kohn-Sham equations 2.9 needs to be solved self-consistently since effective potential $V_{eff}(\vec{r})$, is a functional of the single particle density $n(\vec{r})$ but $n(\vec{r})$ is determined by $V_{eff}(\vec{r})$. Once the self-consistent solution of the Kohn-Sham equation has been obtained, the exact value of the non-interacting kinetic energy can be evaluated by equation 2.8. The major advantage

of introducing the N orbitals is: the Kohn-Sham equations deal with $T_s[n]$, the dominant part of the true kinetic energy T[n] indirectly but exactly. The price for this gain in accuracy is that there are now N one-electron equations to solve as opposed to just one equation for the total density derived from a direct approximation to T[n] of a Thomas-Fermi type.

2.1.2 Exchange-correlation energy

We have seen that HKS scheme maps the problem of a system of interacting electrons onto a system of non-interacting electrons moving in an effective potential given by equation 2.10. The Kohn-Sham DFT approach to the solution of the many-body Schrödinger equation has not required any approximation so far. However, the exchange-correlation $E_{XC}[n(\vec{r})]$ is unknown. Some approximation must be used for E_{XC}.

The simplest approximation is the Local Density Approximation (LDA). In LDA, E_{XC} is defined as

$$E_{XC} = \int \epsilon_{XC}[n(\vec{r})]n(\vec{r})d^3r \tag{2.12}$$

where $\epsilon_{XC}[n(\vec{r})]$ is the exchange-correlation energy per unit volume of a homogeneous electron gas of density $n(\vec{r})$. The exact values of $\epsilon_{XC}[n(\vec{r})]$ were calculated by Ceperley and Alder using the Quantum Monte Carlo [40] technique.

Considering the fact that exchange and correlation are not really local, people also consider $\epsilon_{XC}[n(\vec{r})]$ as a function of the density and gradient of the density at each point. This approximation is usually termed as Generalized Gradient Approximations (GGAs). GGAs do not offer a consistent improvement over LDA in all types of system, but they have been shown to improve on the LDA for calculations of only total energy and bond length of molecular structures [41]. Nowadays the GGA due to Perdew and Wang [42] is widely used.

In cases where the external potential is spin dependent, an approximation must be made to E_{XC} which depends on both the total electronic density $n(\vec{r}) = n_{\uparrow}(\vec{r}) + n_{\downarrow}(\vec{r})$ and the polarization

$$\xi(\vec{r}) = \frac{n_{\uparrow}(\vec{r}) - n_{\downarrow}(\vec{r})}{n(\vec{r})} \tag{2.13}$$

where $n(\vec{r}) = n_{\uparrow}(\vec{r})$ and $n_{\downarrow}(\vec{r})$ are the densities of spin up and spin down electrons respectively. This kind of the approximation is termed as Local Spin Density Approximation (LSDA).

2.2 Pseudopotential Method

2.2.1 Introduction

If all of the electrons in a system were explicitly included when performing a calculation, the computational cost would still be prohibitive for atoms as heavy as Se. Fortunately, many chemical and physical processes are governed by the valence states but only indirectly involve the core states. Thus, the core electron states may be assumed to be fixed and a "pseudopotential" may be constructed for each atomic species which takes into account the effects of the nucleus and core electrons in an effective manner[43]. In the norm-conserving pseudopotential approach, only the chemically active valence electrons are dealt with explicitly. The chemically inert core electrons are eliminated within a frozen-core approximation. All electrostatic and quantum-mechanical interactions of the valence electrons with the ion cores (the nuclear Coulomb attraction screened by the core electrons, Pauli repulsion and exchange correlation between core and electrons) are accounted for by angular momentum dependent pseudopotentials.

2.2.2 Basic Idea

If we have obtained the real core $|\phi_c\rangle$ and valence $|\phi_v\rangle$ electron wavefunctions, we can construct the pseudo-wavefunction

$$|\chi_v\rangle >= |\phi_v\rangle + \sum_c |\phi_c\rangle\langle\phi_c|\chi_v\rangle \tag{2.14}$$

The energy eigenvalue equation satisfied by a valence-band state is

$$\hat{T}|\phi_v\rangle + \hat{V}(\vec{r})|\phi_v\rangle = \epsilon|\phi_v\rangle. \tag{2.15}$$

We want the pseudo-wave function

$$\hat{T}|\chi_v\rangle + \hat{V}^{ps}(\vec{r})|\chi_v\rangle = \epsilon|\chi_v\rangle. \tag{2.16}$$

to also have the same form as 2.15. From equation 2.14, $|\phi_v\rangle$ can be written as

$$|\phi_v\rangle = (1 - \sum_c |\phi_c\rangle\langle\phi_c|)|\chi_v\rangle = (1 - \hat{P})|\chi_v\rangle \tag{2.17}$$

where the projection operator $\hat{P}$ is defined as

$$\hat{P} = \sum_c |\phi_c\rangle\langle\phi_c| \tag{2.18}$$

which projects any state onto the core states. Plug equation 2.17 to equation 2.15, we can obtain

$$\hat{T}|\chi_v\rangle + [\hat{V} + (\epsilon - \hat{T} - \hat{V})P]|\chi_v\rangle = \epsilon|\chi_v\rangle. \tag{2.19}$$

Comparing equation 2.19 with 2.16, we can get the pseudo-potential

$$\begin{aligned} \hat{V}^{ps} &= V + (\epsilon - \hat{T} - \hat{V})P \\ &= V + \sum_c (\epsilon - \hat{T} - \hat{V})|\phi_c\rangle\langle\phi_c| \\ &= V + \sum_c (\epsilon - \epsilon_c)|\phi_c\rangle\langle\phi_c|. \end{aligned} \tag{2.20}$$

The pseudo-Schrödinger equation provides the same eigenvalues as the original Schrödinger equation 2.15 for the valence electrons but it also considers the effects of the core to atoms without explicitly calculating the core wave functions. This is a big advantage for the bulk material (or even molecule system) calculation since we can construct the pseudo potential from the the exact all electron calculation of the single atom system, and use the constructed pseudopotential to calculate the bulk properties without considering the core electrons for the all atoms in the bulk system.

2.2.3 Practical Example: pseudopotential of selenium

If all-electron potential and valence states have been obtained, the pseudo wavefunction with angular momentum is first derived by using the following four conditions[43]:

1. The pseudo wavefunction and the all-electron wavefunction corresponding to the same eigenvalue and their logarithmic derivatives agree beyond a chosen core cutoff radius r_l^c.

2. The radial pseudo wavefunction has the same amplitude as the all electron wavefunction beyond the core cutoff radius r_l^c and is normalized

3. The pseudo wavefunction contains no radial nodes.

4. The all-electron and pseudo valence eigenvalues are identical for a particular atomic configuration.

The pseudopotential components then correspond to an inversion of the Schrödinger equation for the respective pseudo wavefunctions. Fig. 2.1 shows the pseudopotentials for selenium atom. This pseudopotential used in our calculation to obtain the correct crystal structure for t-Se was constructed using Troullier-Martins scheme [45]. The price to pay for the pseudopotential is that they are non-local, angular momentum dependent. This is very different from normal potential such as

Coulomb potential. We can see that each pseudopotential of angular momentum exactly matches the the true potential beyond the core cutoff radius r_l^c.

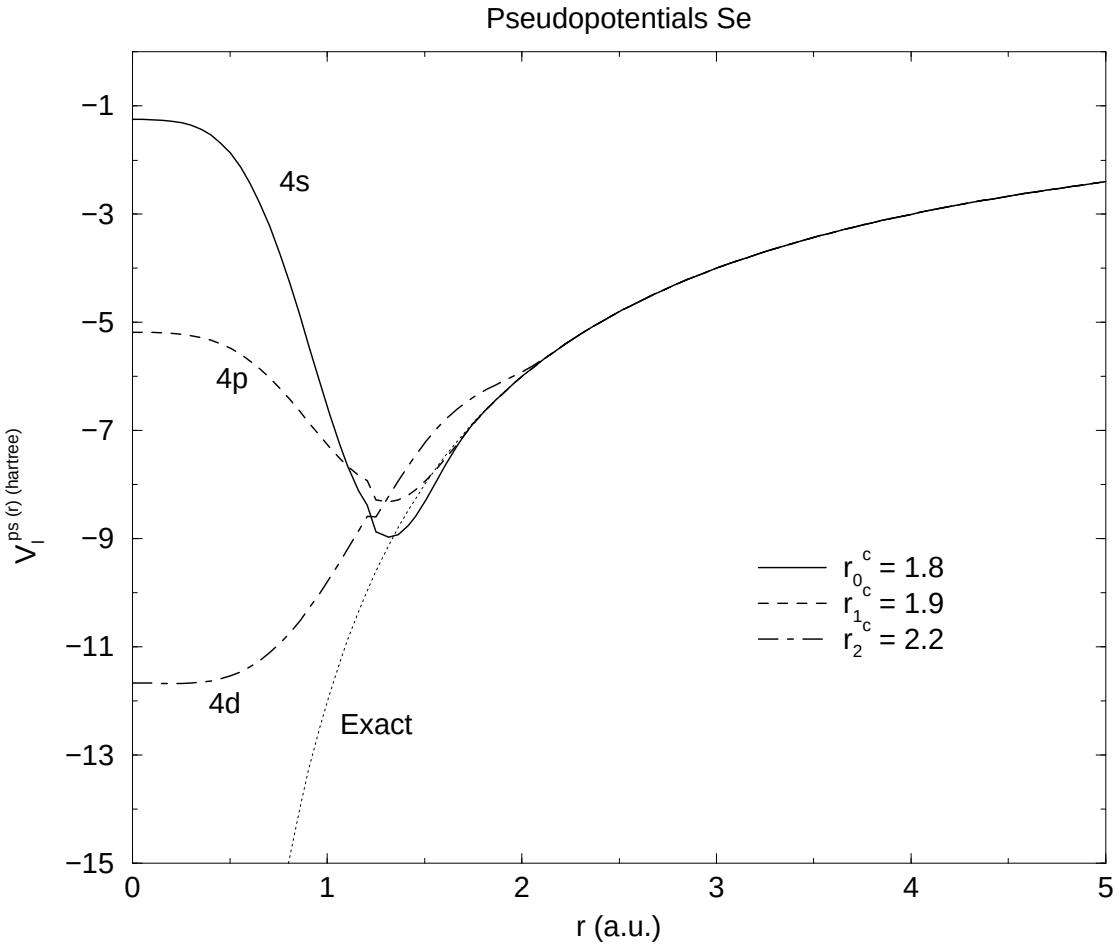

Figure 2.1: The pseudopotentials for selenium atom.

Similar to pseudopotential, pseudo wavefunction should also exactly match the true wavefunction beyond the r_l^c. Usually, the exact wavefunction near the core shows a rapid oscillation due to strong potential in the region and orthogonality

requirement between different states. Rapid oscillation means more Fourier components are required in the momentum space and require the very large plane wave cut-off energy in the real calculations. Since the pseudo wavefunctions only consider the valence electrons, it need not exhibit the rapid oscillations of the true wavefunctions associated with the core. Fig. 2.2 shows the comparison between the true wavefunction and pseudo wavefunction for selenium atoms. We can see that these pseudo wavefunctions match the true wavefunction beyond the r_l^c and does not show oscillation in the core region.

The core cutoff radium r_l^c is a key parameter for constructing the pseudopotentials. The Hamann scheme [44] accomplishes the matching exponentially beyond the core cutoff radium radium r_l^{c-H}, while in the Troullier-Martins scheme [45] this matching is exact at and beyond r_l^{c-TM}. Usually, in the Hamann scheme the core cutoff radii are smaller $r_l^{c-H}/r_l^{c-TM} \approx 0.25-0.75$. But the pseudo wavefunctions and pseudopotentials converge to the all-electron wavefunctions and potentials within a similar range as for the Troullier-Martins scheme. Researchers have tabulated the default core cutoff radium r_c^l for most atom species[43]. In general, increasing r_c^l yields soft pseudopotentials especially suited to plane wave calculations, which converge more rapidly in calculations. However, these will become less transferable as the pseudo wavefunctions become less accurate at radii relevant to bonding.

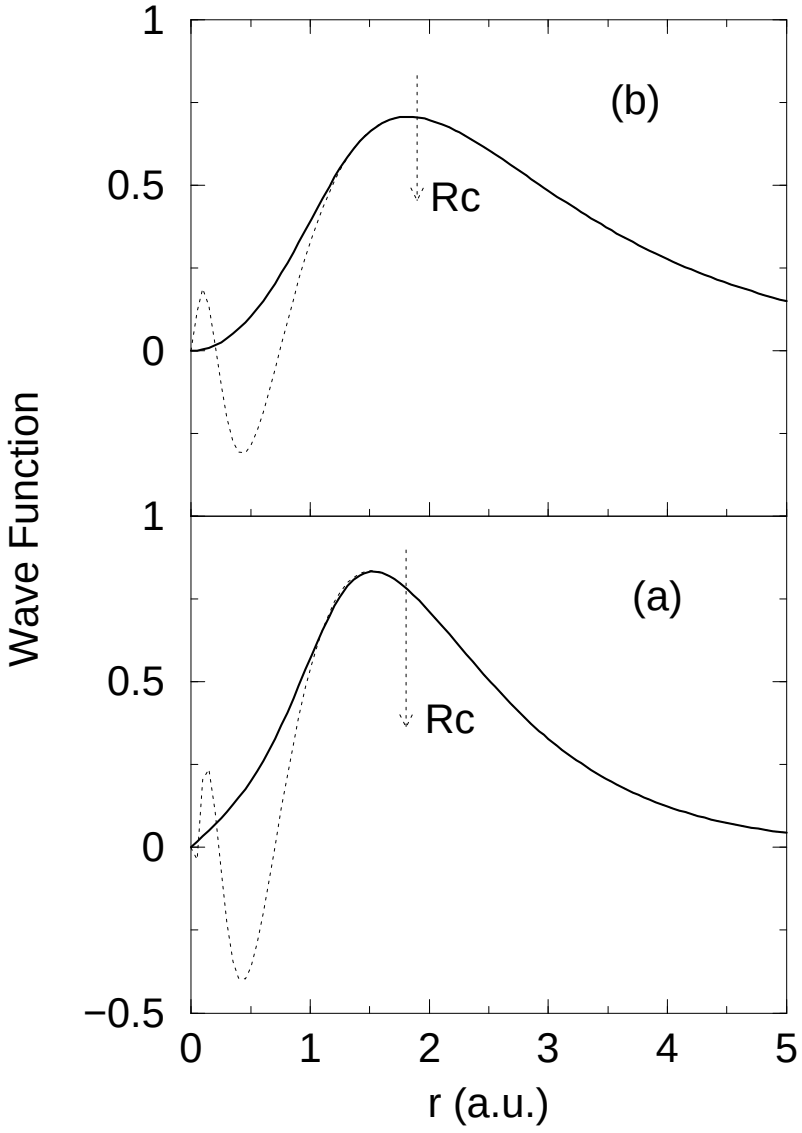

Figure 2.2: The comparison of pseudo wavefunctions (solid line) and true wavefunction (dotted line) for selenium atom. (a) is for the 4s orbital and (b) is for the 4p orbital.

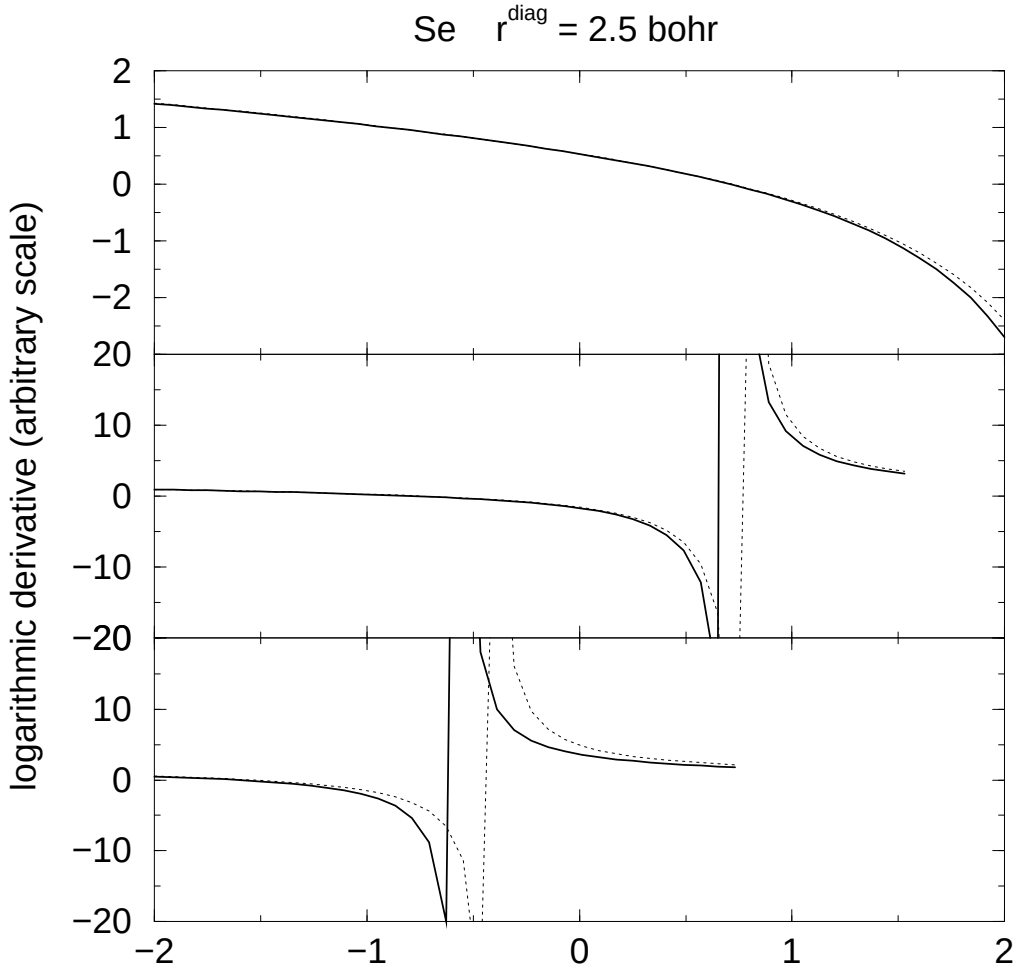

Figure 2.3: The comparison of logarithmic derivatives for the pseudo (solid) and all-electron (dashed) selenium. (a), (b), (c) are for 4s, 4p, 4d respectively.

By construction, a pseudopotential reproduces the valence states of the free atom in the reference configuration. In applications, it needs to perform correctly in a wide range of environments, say free molecules, bulk crystals and amorphous materials. This transferability depends the choice of core cutoff radii and other parameters [43]. The logarithmic derivatives of the radial wavefunctions are mostly used to test the transferability of the pseudopotentials. The pseudopentials should be constructed such that the logarithmic derivatives of the radial wavefunctions,

$$D_l(\epsilon, r^{diag}) = \frac{d}{dr} \ln \mu_l(\epsilon; r)|_{r=r^{diag}} \tag{2.21}$$

agree for the pseudo and all-electron atom, as a function of the energy at some diagnostic radius r^{diag} outside the core region, usual half of a typical interatomic distance. Fig. 2.3 shows the comparison of the logarithmic derivatives for the pseudo and all-electron selenium atom. Since in this calculation, we try to make r_l^c as big as possible to accelerate the convergence of the bulk calculation, the logarithmic derivatives for pseudo potentials has a small deviation with that for all electron potentials. But through the careful test on the bulk calculation on other bulk properties (we will discuss in next section) of selenium atoms, the pseudopotential can reproduce most properties of selenium atoms.

2.3 Electronic Structure Analysis in Tight-Binding Basis

The one particle eigenfunctions of the system can be expressed as the linear combination of atomic basis orbitals in the form:

$$\Psi_n(\vec{k},\vec{r}) = \frac{1}{\sqrt{N}}\sum_{i\alpha} C^n_{i\alpha}(\vec{k}) e^{i\vec{k}\cdot\vec{R}_i}\mu_\alpha(\vec{r}-\vec{R}_i) \tag{2.22}$$

where i is the index of the atom ranging from 1 to N and α is the atomic orbital such as s, p etc.

The eigenfunction for the solid with periodic boundary condition must satisfy Bloch's Theorem. We can show that above wavefunction satisfies Bloch's theorem:

$$\Psi_n(\vec{k},\vec{r}+\vec{R}_n) = \frac{1}{\sqrt{N}}\sum_{i\alpha}^{N} C^n_{i\alpha} e^{i\vec{k}\cdot\vec{R}_i}\mu_\alpha(\vec{r}+\vec{R}_n-\vec{R}_i) = e^{i\vec{k}\cdot\vec{R}_n}\Psi_n(\vec{k},\vec{r}) \tag{2.23}$$

The next task is to convert the Hamiltonian in the many body solid system into matrix representation. Starting from

$$\hat{H}\Psi_n(\vec{k},\vec{r}) = E_n(\vec{k})\Psi_n(\vec{k},\vec{r}), \tag{2.24}$$

i.e.

$$\frac{1}{\sqrt{N}}\sum_{i\alpha} C^n_{i\alpha}(\vec{k})e^{i\vec{k}\cdot\vec{R}_i}\hat{H}\mu_\alpha(\vec{r}-\vec{R}_i) = \frac{1}{\sqrt{N}}\sum_{i\alpha} C^n_{i\alpha}(\vec{k})e^{i\vec{k}\cdot\vec{R}_i}E_n(\vec{k})\mu_\alpha(\vec{r}-\vec{R}_i) \quad (2.25)$$

Using $\int d\vec{r}e^{-ik\cdot\vec{R}_j}\mu^*_\beta(\vec{r}-\vec{R}_j)$ to multiply both sides of the equation, we can get the matrix representation of the Hamiltonian:

$$\begin{array}{ll} & \sum_{i\alpha} \quad [\int d\vec{r}e^{-ik\cdot(\vec{R}_i-\vec{R}_j)}\mu^*_\beta(\vec{r}-\vec{R}_j)\hat{H}\mu_{i\alpha}(\vec{r}-\vec{R}_i)]C^n_{i\alpha}(\vec{k}) \\ = E_n(\vec{k}) & \sum_{i\alpha} \quad [\int d\vec{r}e^{-ik\cdot(\vec{R}_i-\vec{R}_j)}\mu^*_\beta(\vec{r}-\vec{R}_j)\mu_{i\alpha}(\vec{r}-\vec{R}_i)]C^n_{i\alpha}(\vec{k}) \end{array} \quad (2.26)$$

Now, we can define Hamiltonian matrix as

$$\begin{aligned} H_{\beta j,i\alpha}(\vec{k}) &= e^{-ik.(\vec{R}_i-\vec{R}_j)}\int d\vec{r}\mu^*_\beta(\vec{r}-\vec{R}_j)\hat{H}\mu_{i\alpha}(\vec{r}-\vec{R}_i) \\ &= e^{-ik.(\vec{R}_i-\vec{R}_j)}\int d\vec{r}\mu^*_\beta(\vec{r})\hat{H}\mu_{i\alpha}(\vec{r}+\vec{R}_j-\vec{R}_i) \end{aligned} \quad (2.27)$$

and the overlap matrix is

$$\begin{aligned} S_{\beta j,i\alpha}(\vec{k}) &= e^{-ik\cdot(\vec{R}_i-\vec{R}_j)}\int d\vec{r}\mu^*_\beta(\vec{r}-\vec{R}_j)\mu_{i\alpha}(\vec{r}-\vec{R}_i) \\ &= e^{-ik\cdot(\vec{R}_i-\vec{R}_j)}\int d\vec{r}\mu^*_\beta(\vec{r})\mu_{i\alpha}(\vec{r}+\vec{R}_j-\vec{R}_i) \end{aligned} \quad (2.28)$$

So, the original equation can be written in a compact form

$$\sum_{i\alpha} H_{\beta j,i\alpha}(\vec{k})C^n_{i\alpha}((\vec{k}) = E_n(\vec{k})\sum_{i\alpha} S_{\beta j,i\alpha}(\vec{k})C^n_{i\alpha}((\vec{k}) \quad (2.29)$$

or in operator form

$$H(\vec{k})C(\vec{k}) = E(\vec{k})S(\vec{k})C(\vec{k}) \tag{2.30}$$

2.3.1 Density Matrix

The density operator is usually defined as

$$\hat{\rho} = \sum_{n\ occ} |n\rangle\langle n| \tag{2.31}$$

where n means eigenstate. The density matrix needs to be defined in some specific basis. If we set the matrix element of the density matrix in the LCAO basis,

$$\rho_{\beta j,\alpha i} = \sum_{n\ occ} \langle \phi_{j\beta}|n\rangle\langle n|\phi_{i\alpha}\rangle, \tag{2.32}$$

the total charge Q must be redefined (due to the non-orthogonal basis) as

$$Q = Tr[\hat{\rho}] = Tr[S^{-1}\rho] \tag{2.33}$$

We can define another density matrix operator ρ' whose matrix elements is calculated as

$$\rho'_{i\alpha,j\beta} = \sum_{n} C^{n}_{i\alpha}(\vec{k})C^{n}_{j\beta}(\vec{k}). \tag{2.34}$$

The real density matrix in this non-orthogonal space can be represented by

$$\rho = S\rho' S \tag{2.35}$$

The total charge Q is simply

$$Q = Tr[S\rho'] \tag{2.36}$$

2.3.2 Mulliken Charge Analysis

Now, we can express the charge

$$Q = \sum_{i\alpha} \sum_{j\beta} S_{i\alpha,j\beta} \rho'_{j\beta,i\alpha} \tag{2.37}$$

in the local basis. The above expression can be written as

$$\begin{aligned} Q &= \textstyle\sum_i Q_i \\ Q_i &= \textstyle\sum_\alpha \sum_{j\beta} S_{i\alpha,j\beta} \rho'_{j\beta,i\alpha} \end{aligned} \tag{2.38}$$

The Q_i can be understood as the charge localized on the atom site i. By the same spirit, we can also define the charge localized on the atomic orbital α

$$Q_\alpha = \sum_{i} \sum_{j\beta} S_{i\alpha,j\beta} \rho'_{j\beta,i\alpha} \tag{2.39}$$

and charge localized on the atomic orbital α at site i

$$Q_{i\alpha} = \sum_{j\beta} S_{i\alpha,j\beta}\rho'_{j\beta,i\alpha} \tag{2.40}$$

2.3.3 Inverse Participation Analysis

If we explicitly show the contribution of the eigenstates to the density matrix of the system, we can define

$$\rho'^{n}_{j\beta,i\alpha} = C^{n}_{i\alpha}(\vec{k})C^{n}_{j\beta}(\vec{k}). \tag{2.41}$$

The charge Q can now be re-expressed as

$$\begin{aligned} Q &= \textstyle\sum_i \sum_n Q(i,n) \\ Q(i,n) &= \textstyle\sum_\alpha \sum_{j\beta} S_{i\alpha,j\beta}\rho'^{n}_{j\beta,i\alpha} \end{aligned} \tag{2.42}$$

Actually, Q(i,n) physically means the contribution to eigenstate n from atom site i. This point can be easily understood by a special case - orthogonal basis case. In an orthogonal basis,

$$S_{i\alpha,j\beta} = \delta_{ij}\delta_{\alpha,\beta} \tag{2.43}$$

So,

$$Q(i,n) = \sum_\alpha \sum_{j\beta} \delta_{\alpha,\beta}\rho'^{n}_{j\beta,i\alpha} = \sum_\alpha \rho'^{n}_{i\alpha,i\alpha} = \sum_\alpha C^{n}_{i\alpha}(\vec{k})^2 \tag{2.44}$$

A.P.

$$\sum_i Q(i,n) = 1. \tag{2.45}$$

We can define the spatial fluctuation of the eigen-energy state

$$IPR(n) = \sum_i Q(i,n)^2 \tag{2.46}$$

where IPR means "Inverse Participation Ratio". It can be easily verified that IPR(n) = 1/N for totally extended state and IPR=1 for totally localized state (the charge totally contributes from one site). Actually, the bigger the Q(i,n), the more localized the eigenstate n is on site i. This is also the basis for visualization of the eigenstate.

2.3.4 Local Density of State

The density matrix is very useful to calculate other variable in the many body system. The first example is the energy density of states in the system which is defined in operator form is

$$\hat{\rho}(E) = \delta(E - \hat{H}) \tag{2.47}$$

$\hat{\rho}$(E) can be expressed in the occupied space as

$$\hat{\rho}(E) = \sum_n \delta(E - E_n)|n><n| \tag{2.48}$$

The variable we are interested in is the state density

$$\rho(E) = Tr[\hat{\rho}(E)] = \sum_{n\ occ} \sum_{i\alpha} \sum_{j\beta} \delta(E - E_n) \rho'^{n}_{i\alpha,j\beta} S_{i\alpha,j\beta} \tag{2.49}$$

So, we can isolate the density of state contribute from the atomic site i

$$\rho_i(E) = \sum_{n} \delta(E - E_n) \sum_{\alpha} \sum_{j\beta} \rho'^{n}_{i\alpha,j\beta} S_{i\alpha,j\beta} \tag{2.50}$$

from general expression of density of state.

Chapter 3

Properties of the density matrix from realistic calculations[46]

3.1 Introduction

There is a continuing effort to improve the efficiency of single electron methods for modeling materials. The most accurate of these are density functional approaches, and also simple but efficient tight-binding schemes. A unifying feature of these efforts is the need for a real-space localized representation for the one electron states (Kohn-Sham orbitals in a density functional computation), or almost equivalently a real space localized density matrix (DM). While there have been many

calculations exploiting a real space local representation[47, 48], there have been few serious attempts to study the spatial decay of the DM in real materials and with realistic Hamiltonians (for linear alkanes however, see Ref. [50]). The DM is expected to provide a lower bound on how well localized the Wannier states may be (a useful explicit recipe for building these states to minimize their extent has recently been given[49]). In this paper, we directly compute the DM for a metal (Al), crystalline and amorphous phases of Si and C. Among other things, we show that Al is *very* free electron-like, and discuss the significant anisotropies in the DM in insulators, and compare the computed spatial decay to available predictions.

Single-particle density operator $\hat{\rho} = [\exp(\beta(\hat{H}-\mu)+1]^{-1}$ probes the spatial locality of electrons, which enables a spatially local formulation of the electronic structure problem (β is an inverse temperature, μ is the chemical potential). Kohn[51] has stated this clearly, and called the dependence of ground state properties on the local environment "the principle of nearsightedness", and observed that it: "is generally a consequence of wave-mechanical destructive interference". It is difficult to perform analytical calculations of $\rho(\vec{r},\vec{r}') = \langle\vec{r}|\hat{\rho}|\vec{r}'\rangle$ in all but the most simple cases. As such, it is convenient to provide empirical insight from relatively realistic computations.

Li, Nunes and Vanderbilt[52] and Daw[53] recognized that using a truncated $\rho(\vec{r},\vec{r}')$ could lead to a linear scaling total energy and force method. In an atom-centered local representation $|\mu\rangle$, the band energy (for example) is just:E_{bs} =

$Tr(\hat{\rho}\hat{H}) = \sum_\nu \sum_{\mu_\nu} \rho_{\nu\mu} H_{\mu\nu} \equiv \sum_\nu \Gamma_\nu$. Here, the sum index μ_ν emphasizes that only a finite number of terms (independent of system size and only from the local environment of basis functions near the site associated with ν) needs to be computed. Then the CPU time for computing E_{bs} scales as $N\tau_\Gamma$; the desired linear scaling, if τ_Γ is the average time to compute the "local" band energy for the "ν locale" Γ_ν. For a proper discussion, see the reviews of Goedecker[56] and Ordejón[57].

3.2 Elementary estimates of the density matrix

For the free electron gas at zero temperature, the DM is given in standard textbooks[54]:

$$\rho(\vec{r},\vec{r}') = 2(2\pi)^{-3} \int_{k<k_F} d^3k \; e^{-i\mathbf{k}\cdot(\vec{r}-\vec{r}')} \;=\; 3n[sin(\zeta) - \zeta cos(\zeta)]/\zeta^3 \qquad (3.1)$$

where $\zeta = k_F|\vec{r}-\vec{r}'|$, k_F is the Fermi wavevector.

The DM for this system has long range at $T = 0$, with that range determined by k_f^{-1} (arising here only from symmetry requirements since the electrons are non-interacting); the DM (and electron pair distribution function) wiggles and decays as a power law for $\zeta \to \infty$[54]. The analytic origin of the slow decay is the abrupt cutoff at the Fermi surface, and is mathematically nothing more than a case of "Gibbs' phenomenon"[59] as seen in the theory of Fourier series. Of course it is

quite *physical* in this case and is similar in origin to the Freidel oscillations and the oscillatory RKKY interaction. For finite temperature the decay envelope is exponential because of the smooth cutoff of the Fermi function.

It is generally believed that the real space DM shows an exponential decay behavior at zero temperature for insulators[60]:

$$\rho(\vec{r},\vec{r}') \propto exp\left(-\gamma|\vec{r}-\vec{r}'|\right). \tag{3.2}$$

Kohn[61] proved the exponential decay behavior in the case of one-dimensional model crystal. Stephan et al.[64] observed that the exponential decay of orthogonalized Wannier function in the crystalline and amorphous systems with similar local topological order (and a similar *mobility* gap) appears to be close.

Some simple predictions for the asymptotic decay of the DM are available. Ismail-Beigi and Arias[58], predicted that for insulators in the weak binding limit, one should observe an exponential decay with rate:

$$\gamma_{wb} = aE_{gap}m/\hbar^2, \tag{3.3}$$

whereas Kohn[61] suggested that in the tight binding limit:

$$\gamma_{tb} = (2E_{gap}m/\hbar^2)^{1/2}, \tag{3.4}$$

We compare these to our numerical calculations below. Units for all decay rates are $\mathring{A}^{-1}$.

3.3 Calculations

In this paper we implement reasonably realistic calculations, with an approximate density functional Hamiltonian due to Sankey and Niklewski[84]. This Hamiltonian has four basis functions (pseudoatomic orbitals) per atom, employs the Harris functional and nonlocal pseudopotentials. The basis is nonorthogonal and the method has been well tested for the systems we describe here. We compute the DM as:

$$\rho(\vec{r},\vec{r'}) = 2\sum_{n\ occ} \psi_n^*(\vec{r})\psi_n(\vec{r'}) \tag{3.5}$$

in which $\psi_n(\vec{r})$ is the nth eigenvector of the Sankey Hamiltonian. All calculations reported here were performed using exact diagonalization on 500 atom (Al) and 512 atom (Si, C) cells. Beside crystal phases, we use realistic models of a-Si and amorphous diamond (a-D) due to Djordjevic, Thorpe and Wooten[9]. Calculations are restricted to the Γ point of the Brillouin zone: the models are large enough to avoid additional **k** sums beside the band sums. Occupations are computed for $T = 0$. The DMs reported in this paper always adopt the midpoint between two

atoms as origin. While not especially significant in metals, this is of course the bond center in the tetrahedral insulators we discuss later.

3.3.1 Metals

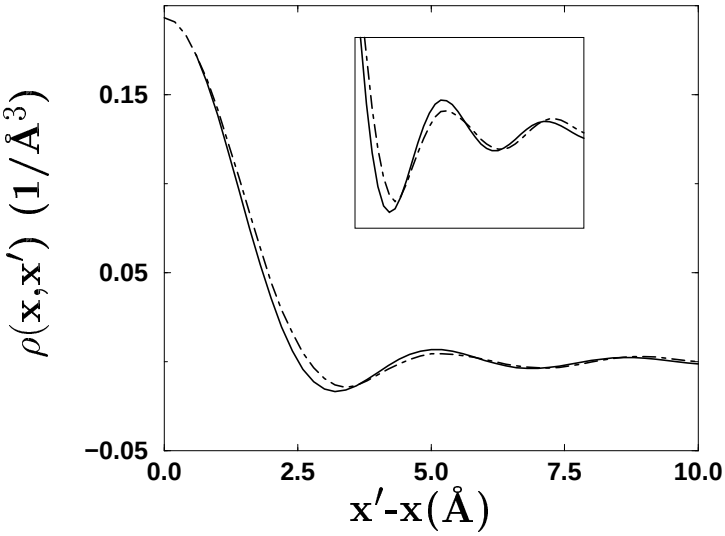

Figure 3.1: The real space density matrix for the 500 atom Al system. The inset is a blow-up of the density matrix for the tail region to show the oscillatory behavior. The dot-dashed line represents the calculation and solid line is from Equation 1.

Equation 3.1 is derived from the free electron gas. It is not clear to what extent the electrons in a real metal mimic the free electron gas. To study the decay properties in a real metal, we extract the DM for a 500 atom model of FCC Al (the supercell is 20.25 $\mathring{A}$ on a side) . The DM is calculated from equation 3.5. Fig. 3.1 gives the decay of the DM in this metal. Clearly, the electrons behave much like free

particles in view of the near coincidence of the analytic result and the calculation from Equation 3.5. The electron density used for Eq. 3.1 is n=0.185$\mathring{A}^{-3}$ (the actual density of valence electrons) which leads to the Fermi vector $k_F = 1.763\mathring{A}^{-1}$.

To check the origin of the ringing in Fig. 3.1 , we also considered a "heavily p-doped" insulator (c-Si) (by shifting the Fermi level well into the valence states), and a power-law decay and ringing was observed as for Al.

3.3.2 Insulators

We have seen that the DM for Al is quite isotropic due to the delocalization of the valence electrons. For Si and C, we calculate the DM along several directions including parallel and orthogonal to the bond direction. As we show in Fig. 3.2, there is a large degree of anisotropy in the decay of the DM for a 1000 atom model of (a) diamond-Si and (b) amorphous Si. The decay appears to be most rapid and monotonic along directions significantly different than the bond direction or the direction orthogonal to it. The decay is slowest in the longitudinal (bond parallel) direction. This result is in qualitative agreement with results for orthonormal Wannier functions reported in Ref. [64]. The box size for the 1000 atom c-Si model is 27.15$\mathring{A}$, for a-Si, 27.694$\mathring{A}$.

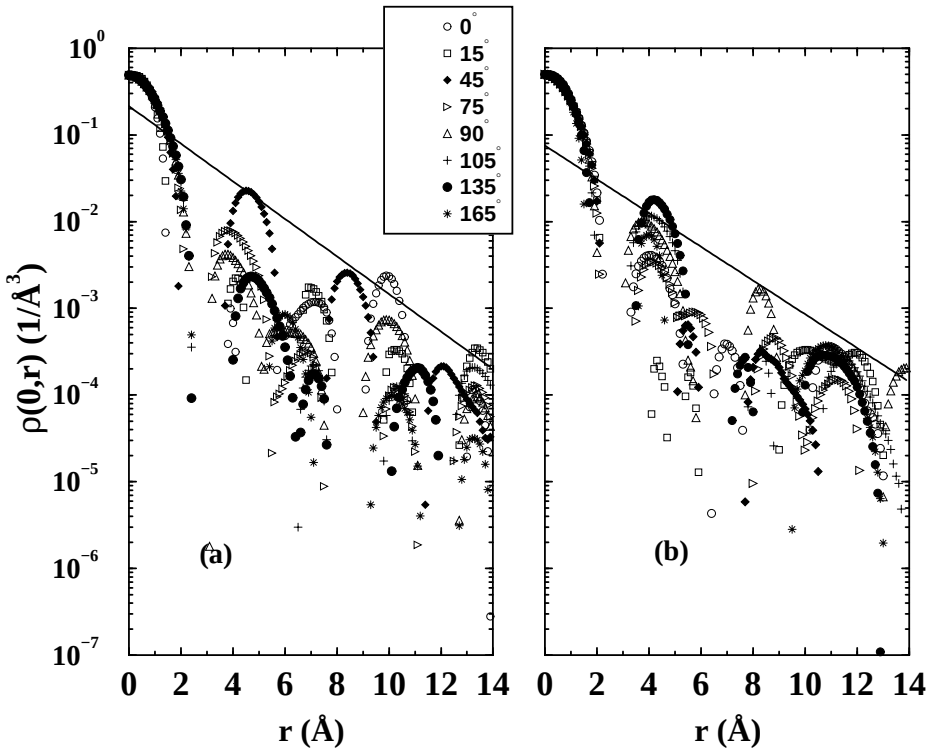

Figure 3.2: a) Real space density matrix for 1000 atom model of diamond Si, b) amorphous Si, both plotted on a log scale. The curves indicate the decay of the density matrix for different directions from a bond center. Here 0° refers to the bond direction, 90° is orthogonal to the bond etc. The lines plotted are intended to be representative of the overall decay, and have slope $\gamma = 0.49\mathring{A}^{-1}$ for the crystal and $\gamma = 0.45\mathring{A}^{-1}$ for amorphous.

We have checked the formula of Ref. [58]. Using experimental values for a and E_g, they obtain $\gamma_{wb} \approx 0.8\mathring{A}^{-1}$ and $2.5\mathring{A}^{-1}$, for c-Si and c-C respectively. Kohn's prediction[61] for the tight-binding regime (Eq. 3.4) yields $\gamma_{tb} \approx 0.54\mathring{A}^{-1}$ for Si, and $\gamma_{tb} \approx 1.19\mathring{A}^{-1}$ for C. Evidently these two approaches give reasonably similar results for Si, but very different rates for C. Best fits from our calculations give $\gamma \approx 0.49\mathring{A}^{-1}$ for c-Si, $\gamma \approx 1.34\mathring{A}^{-1}$ for c-C in rather good agreement with the estimate of Kohn for both materials and in reasonable agreement with Ismail-Beigi and Arias[58] for Si. In fairness to the authors of Ref. [58], they would not expect C to be well described by their expression (Eq. 3.3). We should note that there is such an important effect from directional anisotropy that there is some significant uncertainty (of order 0.05 $\mathring{A}^{-1}$ in the decays reported. The rates reported here are from a calculation on a 1000 atom model of c-Si and a 512 atom model of diamond (box size $14.24\mathring{A}$).

Next, we discuss the DM for a 1000 atom model of amorphous Si[65] and 512 atom model of a-diamond[9]. These disordered networks have much of the local (tetrahedral) character of diamond albeit without long range order. We observe that the asymptotic decay rates for c-Si and a-Si are not very different. Stephan et al.[64] conjectured that the decay of the WF's (as well as DM) is related to separation of the *extended* occupied and unoccupied states (similar for these amorphous and crystalline models), i.e., the width of the mobility gap, a statement consistent with our work. While there is minor variation in decay rates, within fitting uncertainty,

all decay rates for a-Si are similar (and approximately equal to the result for the crystal), independent of whether a strained bond or "typical" bond is selected, within the uncertainty due to anisotropy. The same is true for a-D. We emphasize that the *short range* character of the DM depends strongly on the choice of bond, but not the behavior of the tail of the DM. One can interpret this a consequence of the work of Rehr and Kohn[66] and Kohn and Onffroy[67], who show long range decay of the DM is very similar for "ordinary" or highly defective sites. We observed a similar insensitivity in the tail when we introduced artificial defects in c-Si. We also note that Stephan, Martin and Drabold[64] noted that orthogonalized Wannier functions for a-Si have an intricate non-spherical structure depending on the disorder in the material, which is consistent with our work.

From Fig. 3.3, we report contour plots for the DM starting at a bond center. The figure shows the DM for the crystal (Fig. 3.3a), and two sites (tetrahedral and defective) for Figs. 3.3b and c. Notice that the DM shows a clear tendency to become non-spherical in all cases, reflecting the directionality of the covalent bond. In a disordered environment, this symmetry is retained near the origin for a normal (tetrahedral) environment and destroyed at larger correlation length (Fig. 3.3b). In a-Si, even the structure near the origin for the non-tetrahedral environment is distorted, producing a rather irregular structure in the whole space (Fig. 3.3c). The anisotropy which we have discussed is made quite apparent in these figures.

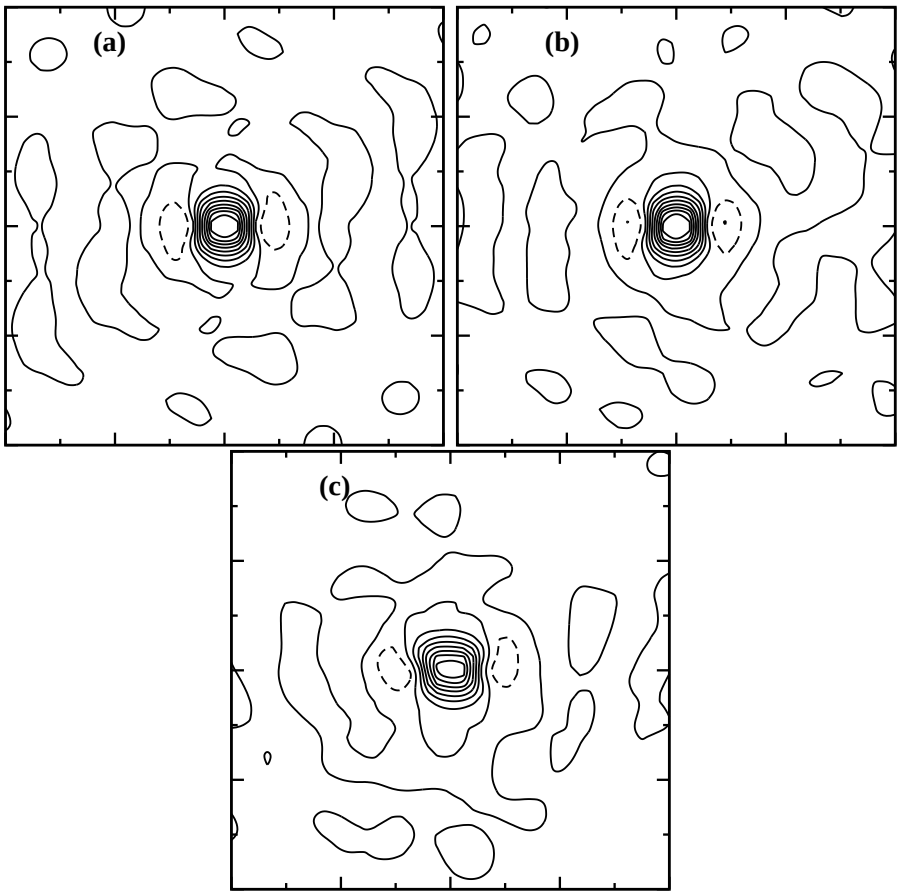

Figure 3.3: Contour plot for (a) real space density matrix for c-Si (b), a-Si at tetrahedral bond, (c) and a-Si from a badly strained bond. Abscissa means longitudinal and ordinate describes transverse direction relative to bond. Box edge is $20\mathring{A}$ (these cells have 512 atoms). The dashed line indicates region for which the density matrix becomes negative.

3.4 Conclusion

We compute the single particle density matrix in large (500, 512 and 1000 atom) models of FCC aluminum, crystalline (diamond) and amorphous silicon and carbon. We use an approximate density functional Hamiltonian in the local density approximation. The density matrix for FCC aluminum is found to closely approximate the results for jellium, and the crystalline and amorphous insulators exhibit exponential decay albeit with pronounced anisotropy. We compare the computed decays to existing predictions of the fall off of the density matrix in insulators and find that the "tight-binding" prediction of Kohn [W. Kohn, Phys. Rev. **115** 809 (1959)] provides the best overall fit to our calculations for Si and C.

Chapter 4

Structural analysis methods

4.1 Introduction

Once we have a model for an amorphous material, the next thing is to evaluate the model to see whether it is consistent with the experimental data. The most direct experimental observable are pair correlation function and static structure factor. In the next subsection, I will give a short review of these two important observables.

4.2 Pair Correlation Function

Amorphous materials are many-particle systems. For N-particle systems, one can define the n-body density function,

$$\rho^n(\vec{r}_1, \vec{r}_2, ..., \vec{r}_n) = \frac{1}{Z_N} \frac{N!}{(N-n)!} \int exp(-\beta U_N) d\vec{r}_{n+1} ... d\vec{r}_N \tag{4.1}$$

which describes the probability of any n particles of this N-particle system will be find at positions $\vec{r}_1, \vec{r}_2, ..., \vec{r}_n$. Equation 4.1 is usually written in another form

$$\rho^n(\vec{r}_1, \vec{r}_2, ..., \vec{r}_n) = \rho(\vec{r}_1)\rho(\vec{r}_2)...\rho(\vec{r}_n) g(\vec{r}_1, \vec{r}_2, ..., \vec{r}_n) \tag{4.2}$$

in which $g(\vec{r}_1, \vec{r}_2, ..., \vec{r}_n)$ is called n-particle correlation function. For most material we studied, the one particle density function $\rho(\vec{r}_i)$ are constant and equal to $\rho_0 = N/V$. One can write the correlation function in the following form

$$\begin{aligned} g(\vec{r}_1, \vec{r}_2, ..., \vec{r}_n) &= \frac{1}{\rho^n} \rho^n(\vec{r}_1, \vec{r}_2, ..., \vec{r}_n) \\ &= \frac{V^n}{Z_N N^n} \frac{N!}{(N-n)!} \int e^{-\beta U_N(\vec{r'}_1, ..., \vec{r'}_N)} \delta(\vec{r}_1 - \vec{r'}_1) ... \delta(\vec{r'}_n - \vec{r'}_n) d\vec{r'}_1, ..., d\vec{r'}_N \\ &= \frac{V^n}{N^n} \frac{N!}{(N-n)!} \langle \prod_{i=1}^{n} \delta(\vec{r}_i - \vec{r'}_i) \rangle \end{aligned} \tag{4.3}$$

where $\langle ... \rangle$ means average over all configurations. The simplest n-body density function is the 2-body density function $\rho_2(\vec{r}_1, \vec{r}_2)$. The 2-body density function for

the ions in the amorphous material is

$$\rho^{(2)}(\vec{r}_1, \vec{r}_2) = \rho(\vec{r}_1)\rho(\vec{r}_2)g^{(2)}(\vec{r}_1, \vec{r}_2) \tag{4.4}$$

in which $\rho(\vec{r})$ is the one particle density function and $g(\vec{r}_1, \vec{r}_2)$ is the pair distribution function. Usually $\rho^{(2)}(\vec{r}_1, \vec{r}_2) \neq \rho(\vec{r}_1)\rho(\vec{r}_2)$ since the probability of occupying $\vec{r}_1$ may be affected by another particle occupying $\vec{r}_2$. So, if $r_1 - r_2 \to \infty$, we expect $g^{(2)}(\vec{r}_1, \vec{r}_2) \to 1$. The 2-body correlation function is

$$g^{(2)}(\vec{r}_1, \vec{r}_2) = \frac{N(N-1)}{\rho_0^2}\langle\delta(\vec{r}_1 - \vec{r'}_1)\delta(\vec{r}_2 - \vec{r'}_2)\rangle \tag{4.5}$$

In general, for homogeneous systems in equilibrium, there are no special points in space, so that $g^{(2)}$ should depend only on the relative position of the particles or the difference. In this case, it proves useful to introduce the change of variables

$$\vec{R} = \frac{1}{2}(\vec{r}_1 + \vec{r}_2) \quad \vec{r} = \vec{r}_1 - \vec{r}_2 \tag{4.6}$$

so g^2 can be written as

$$g^2(\vec{R}, \vec{r}) = \frac{N(N-1)}{\rho_0^2}\langle\delta(\vec{R} + \frac{1}{2}r - \vec{r'}_1)\delta(\vec{R} - \frac{1}{2}r - \vec{r'}_2)\rangle \tag{4.7}$$

The pair correlation function is defined as

$$\begin{aligned} g(\vec{r}) &= \frac{1}{V}\int d\vec{R} g^2(\vec{R},\vec{r}) \\ &= \frac{N(N-1)}{\rho_0^2 V}\langle\delta(\vec{r}-\vec{r}_{12})\rangle \end{aligned} \tag{4.8}$$

Notice that average means that we are averaging over all the possible distance between two ions. If we treat all the ions as a point particles, the $g(\vec{r})$ can be written as

$$\begin{aligned} g(\vec{r}) &= \frac{N(N-1)}{\rho_0^2 V}\frac{1}{N(N-1)}\sum_{i\neq j}\delta(\vec{r}-\vec{r}_{ij}) \\ &= \frac{1}{\rho_0 N}\sum_{i\neq j}\delta(\vec{r}-\vec{r}_{ij}) \end{aligned} \tag{4.9}$$

If the angular distribution is not the information needed, we can take angular average to obtain the radial pair correlation function $g(r)$

$$\begin{aligned} g(r) &= \frac{1}{4\pi}\int g(\vec{r}) sin(\theta) d\theta d\phi \\ &= \frac{1}{4\pi\rho_0 N}\sum_{i\neq j}\int d\theta d\phi \frac{1}{r r_{ij}}\delta(r-r_{ij})\delta(\theta-\theta_{ij})\delta(\phi-\phi_{ij}) \\ &= \frac{1}{4\pi r^2\rho_0 N}\sum_{i\neq j}\delta(r-r_{ij}) \end{aligned} \tag{4.10}$$

The function $g(r)$ carries information on the structure of the system. For a crystal, it exhibits a sequence of peaks at positions corresponding to shells around a given system. For amorphous materials and liquid, $g(r)$ exhibits its major peak close to the

average atomic separation of neighboring atoms, and oscillates with less pronounced peaks at larger distances. The magnitude of the peaks usually decays exponentially with distance as $g(r) \to 1$. In most cases, $g(r)$ vanishes below a certain distance where atomic repulsion is strong enough to prevent pairs of atoms from getting too close.

4.2.1 Information from the pair correlation function

The pair correlation function directly connects to many properties of the systems to be studied. In the following, I list the thermodynamic functions calculated from the pair correlation function. Most of them are from ref. [69]

Average potential energy for the pairwise interactions:

$$U^{(2)} = \frac{N^2}{V} \int d\vec{r} v(\vec{r}) g(\vec{r}) \tag{4.11}$$

Pressure:

$$P = \rho k_B T - \frac{2\pi\rho^2}{3} \int_0^\infty r \frac{dv(r)}{dr} g(r) r^2 dr \tag{4.12}$$

Compressibility:

$$\alpha_T = \frac{1}{k_B T \rho} + \frac{1}{k_B T} \int (g(\vec{r}) - 1) d\vec{r} \tag{4.13}$$

where compressibility α_T is defined as

$$\alpha_T = \frac{1}{k_B T} \frac{\langle (\Delta V)^2 \rangle}{V} \tag{4.14}$$

4.3 Static Structure Factors

Usually, the information of the pair correlation function derives from the scattering experiment. Researchers usually measure the structure factor of the material from X-ray or neutron scattering experiment. Consider the sample of liquid, solid, glass, etc., containing N atoms, irradiated by X-rays, or neutrons, or light, or electrons, etc., with a wave vector of $\vec{k}_0$. The detector is set to measure the radiation scattered at angle ϕ. The intensity of the radiation scattered at angle ϕ with the wave vector $\vec{k}_f$, and $\vec{Q} = \vec{k}_f - \vec{k}_i$ is

$$\begin{aligned} \frac{I(\vec{Q})}{|f_a(\vec{Q})|^2} &= \left| \sum_{i=1}^{N} exp(i\vec{Q}\vec{r}_i) \right|^2 \\ &= \sum_{i=1}^{N} exp(i\vec{Q} \cdot \vec{r}_i) \sum_{j=1}^{N} exp(-i\vec{Q} \cdot \vec{r}_j) \\ &= \sum_{ij}^{N} exp(i\vec{Q} \cdot \vec{r}_{ij}) \end{aligned}$$

$$
\begin{aligned}
&= \sum_{i=j}^{N} exp(i\vec{Q}\cot\vec{r}_{ij})) + \sum_{i\neq j}^{N} exp(i\vec{Q}\cdot\vec{r}_{ij}) \\
&= N + \int d\vec{r}\sum_{i\neq j}\delta(\vec{r}-\vec{r}_{ij})exp(i\vec{Q}\cdot\vec{r}) \\
&= N + \rho_0 N\int d\vec{r}g(\vec{r})exp(i\vec{Q}\cdot\vec{r}) \qquad (4.15)
\end{aligned}
$$

So, the static structure factor is defined as

$$S(\vec{Q}) = \frac{I(\vec{Q})}{Nf_a(\vec{Q})|^2} = 1 + \rho_0\int d\vec{r}g(\vec{r})exp(i\vec{Q}\cdot\vec{r}) \qquad (4.16)$$

Since

$$\delta(\vec{Q}) = (2\pi)^{-3}\int exp(i\vec{Q}\cdot\vec{r})d\vec{r} \qquad (4.17)$$

The $S(\vec{Q})$ in our equation contains events which are not affected by the presence of the materials studied and this contribution is denoted by the $\delta(\vec{Q})$, so, one usually subtract $(2\pi)^3\rho_0\delta(\vec{Q})$ from the $S(\vec{Q})$. This leads to the following general used expression for the static structure factor

$$S(\vec{Q}) = \frac{I(\vec{Q})}{N} = 1 + \rho_0\int d\vec{r}(g(\vec{r})-1)exp(i\vec{Q}\cdot\vec{r}) \qquad (4.18)$$

For an isotropic material, which most disordered substances are, $S(\vec{Q}) \rightarrow S(|\vec{Q}|)$ which is often written S(Q)

$$S(Q) = 1 + 4\pi\rho_0\int_0^\infty (g(r)-1)\frac{sin(Qr)}{Qr}r^2dr \qquad (4.19)$$

4.3.1 Structure Factor for binary system

4.3.2 Faber-Ziman structure factors

For a binary system, the scattering amplitude can be written as

$$I(\vec{Q}) = \left| \sum_k f_A(\vec{Q}) exp(i\vec{Q} \cdot \vec{r}_k(A)) + \sum_l f_B(\vec{Q}) exp(i\vec{Q} \cdot \vec{r}_k(B)) \right|^2 \tag{4.20}$$

we can define the partial structural factor

$$S_{\alpha\beta} = 1 + 4\pi\rho_0 \int_0^\infty (g_{\alpha\beta}(r) - 1) \frac{sin(Qr)}{Qr} r^2 dr \tag{4.21}$$

such that the scattering amplitude $I(Q) = NF(Q)$ can be expressed as

$$F(Q) = f_A^2(c_A c_B + c_A^2 S_{AA}(Q)) + f_B^2(c_A c_B + c_B^2 S_{BB}(Q)) + 2 f_A f_B c_A c_B (S_{AB}(Q) - 1) \tag{4.22}$$

where $c_\alpha = N_\alpha/N$ and α, β=A,B. The structure factor defined in equation 4.21 is usually termed as Faber-Ziman structure factors [114]. From equation 4.21, it can be seen that these structure factors are directly linked to partial pair correlation functions. Experimentalist usually uses Faber-Ziman structure factors to extract the pair correlation functions.

4.3.3 Bhatia-Thornton structure factors

In the multi-component amorphous materials and liquid alloys, the concentrations of some components and total particle number are statistical variables, i.e. there are concentration and particle number fluctuations. In particular Krishnan and Bhatia [116] showed that the observed strong temperature dependence of the resistivity of an order-disorder type of alloy near its critical point may be attributed to the corresponding temperature dependence of the concentration fluctuations. Bhatia and Thornton [115] proposed another set of structure factor which can directly link to the thermodynamic properties of the alloy. The connection between the Bhatia-Thornton structure factors and Faber-Ziman structure factors can be seen from rewriting equation 4.22 as

$$F(Q) =< f >^2 S_{NN} + (\Delta f)^2 S_{CC} + 2\Delta f < f > S_{NC} \tag{4.23}$$

where $< f >= (f_A + f_B)/2$ and $\Delta f = f_A - f_B$ and

$$\begin{aligned} S_{NN} &= c_A^2 S_{AA} + c_B^2 S_{BB} + 2c_A c_B S_{AB} \\ S_{NC} &= c_A c_B [c_A (S_{AA} - S_{AB}) - c_B (S_{BB} - S_{AB})] \\ S_{CC} &= c_A c_B [1 + c_A c_B (S_{AA} + S_{BB} - 2S_{AB})] \end{aligned} \tag{4.24}$$

are Bhatia-Thornton structure factors. Bhatia and Thornton showed that at large Q, S_{NN} oscillates and tends to one, S_{NC} behaves similarly about zero and S_{CC} about $c_A c_B$. In the long-wavelength limit ($Q \to 0$), S_{NN} and S_{CC} represent, respectively, the mean square thermal fluctuations in the particle number and concentration, and S_{NC} the correlation between these fluctuations. Especially, Bhatia and Thornton gave the thermodynamic formulas for these fluctuations as:

$$\begin{aligned} S_{CC}(0) &= Nk_bT/\left(\frac{\partial^2 G}{\partial^2 c_A}\right)_{T,P,N} \\ S_{NN}(0) &= (N/V)k_BT\kappa_t + \delta^2 S_{CC}(0) \\ S_{NC}(0) &= -\delta S_{CC}(0) \end{aligned} \tag{4.25}$$

where κ_T is the isothermal compressibility, G is the Gibbs free energy, P is the pressure, and δ is a dilation factor defined by

$$\delta = \frac{N}{V}(v_A - v_B) \tag{4.26}$$

where v_A and v_B are the partial molar volumes per atom of the two species.

Since the Bhatia-Thornton structure factors and the Faber-Ziman structure factors are mutually interconvertible it is a matter of convenience which is used. The Bhatia-Thornton ones connect more directly with fluctuations and the Faber-Ziman

ones may be thought to arise more naturally in scattering discussions and in connection with the partial pair correlation functions. As Cusack [4] discussed: $S_{CC}(0)$ has featured in much discussion of liquid mixtures because, if $S_{CC}(0) \approx 0$, fluctuations are negligible and this signifies a stable compound; on the other hand if $S_{CC}(0)$ becomes very large then the large concentration fluctuations imply a tendency to phase separation or liquid immiscibility. Since scattering observations becomes impossible at very small Q, $S_{CC}(0)$ has to be obtained by extrapolating the intensity to Q=0. The $S_{CC}(0)$ from thermodynamic measurements can be used as a test to see whether the extrapolation results are satisfactory or not.

4.3.4 Obtaining structure factors from the structure models

The experimental pair correlation functions are usually obtained from Fourier transform of the structure factors. However, it is relatively easy for us to obtain the pair correlation functions directly from the structure models as we have seen in equation 4.10. Starting from equation 4.19, we can see that

$$S(Q) = 1 + 4\pi\rho \int_0^{r_{max}} dr(g(r) - 1)\frac{sin(Qr)}{Qr}r^2 \tag{4.27}$$

where where ρ is the density of the material and r_{max} is the maximum correlation length in the model. In the sense of super-cell, r_{max} is taken to be half of the box

length. If we plug equation 4.10 to equation 4.19, the S(Q) can be calculated by

$$\begin{aligned} S(Q) &= I(Q) + R(Q) \\ I(Q) &= 1 + \frac{1}{N}\sum_{i\neq j}\frac{sin(Qr_{ij})}{Qr_{ij}} \\ R(Q) &= 4\pi\rho\left(\frac{cos(Qr_{max})r_{max}}{Q^2} - \frac{sin(Qr_{max})}{Q^3}\right) \end{aligned} \tag{4.28}$$

where R(Q) reflects the strong scattering intensity in the forward direction with $Q = 0$. This peak would fall in the incident beam and can not be observed in practice. For binary glassy materials, the partial pair correlation function are usually calculated as

$$g_{\alpha\beta}(r) = \frac{1}{4\pi r^2 \rho N c_\alpha c_\beta}\sum_{i\neq j}\delta(r - r_{ij}). \tag{4.29}$$

so the total pair correlation function can be expressed as

$$g(r) = \sum_\alpha\sum_\beta c_\alpha c_\beta g_{\alpha\beta} \tag{4.30}$$

where α and β run over A and B. The Faber-Ziman structure factors can be easily calculated as

$$A_{\alpha\beta} = 1 + \frac{1}{N c_\alpha c_\beta}\sum_{ij}\frac{\sin(Qr_{ij})}{Qr_{ij}} - R(Q). \tag{4.31}$$

The Faber-Ziman structure factors and Faber Ziman structure factor presented in chapter 7 are calculated from equation 4.31 and equation 4.24.

Chapter 5

Ab initio simulation of amorphous selenium

5.1 Introduction

Liquid and amorphous selenium(a-Se) have been the subject of intense study for more than half a century. Selenium is the element with the most allotropes, many of which are fascinating from a structural point of view. There are also five crystalline forms of selenium under normal pressure and temperature condition: Trigonal Se(t-Se), the stable form at 300K and 1.013 bar, and α, β, γ monoclinic Se and rhombohedral Se. t-Se consists of the parallel helical chains and the other forms

are molecular crystals with building blocks of Se_8 and Se_6, respectively. The atomic electronic structure is s^2p^4, with an s band lying well below the Fermi Level and not participating in the bonding. Two p electrons form covalent σ bonds and the remaining p electrons enter the nonbonding lone pair (LP) state. LP states are the highest filled states and form the valence band, while empty antibonding σ^* states form the conduction bands. Hence the crystalline t-Se behaves as a semiconductor under normal pressure. Under high pressure, the p-bonding mechanism tends form a simple-cubic crystal causing an increase of the coordination number from 2 to 6 [70]. The structure is then a rhombohedral distortion of a simple-cubic lattice and, under these conditions, Se should become metallic.

Amorphous selenium has unique photoelectronic properties which make it a natural candidate for photoreceptor in the photocopying process [71]. a-Se is also highly sensitive to X rays. This made a-Se one of the first x-ray photoconductors tested for use in digital radiography [72]. The photoconducting and semiconducting properties of amorphous Se are connected with the nature and concentration of the defects present. In spite of the the accumulation of much experimental data, the atomic structure of a- and l-Se remains controversial. Henninger et al. [73] concluded that a-Se consisted of Se chains in random orientation and "liquidlike atomic assemblage" on the basis of early x-ray and neutron scattering data. Kaplow et al. [76] were led by the their data to conclude that a-Se is a molecular solid made up of disordered

Se_8 molecules. Robertson [74] and Lucovsky and Wong [75] were among the first to note that radial distribution functions from scattering experiments alone are insufficient to distinguish between the various models. They developed a static model for the structure of *a*-Se based on the additional information from XPS/UPS and infrared(IR) spectra and comparison with parameterized calculations for the electronic density of state(DOS) and the IR response. In this model, the vast majority of atoms are in chains and the five- or six-atom ring content is low ($< 5\%$). Misawa and Suzuki [77] proposed a similar disordered chain model for liquid selenium, and computed ring and chain fractions as functions of temperature. Enderdy and Barnes [78] concluded that the structural properties of liquid Se were correctly represented by a model of a freely rotating chains. The question of the relative role of rings versus chains in l- and *a*-Se is still unsettled. The chain model should be confirmed by simulations that do not rely upon the assumption that chain already exist. In other words, the existence of a chemical bond should be the result of an *ab initio* quantum mechanical calculation.

There is evidence from electronic and optical phenomena that *a*-Se have a significant density of gap states with E_F pinned near the center of the energy gap (Mott and David 1979). Singly occupied states near E_F would be expected but no ESR or paramagnetism confirms their presence. To explain these unusual properties, Anderson, Street, Kastner suggested that there is a change of the topology of defect site

due to the electron phonon coupling which allows the relaxation. The coordination defects in chalcogenide glass such as selenium take the form of valence alternation pairs [7]. Such defects are characterized by a different atomic configuration in the different charge states. The positive defects are overcoordinated and the negative defects are undercoordinated. It is even noted that the doping properties of *a*-Si:H can be understood by valence alternation [79]. The valence alternation model has been verified by some experiments and especially the most recent electron spin resonance (ESR) experiment by Kolobov [8] gave the direct experimental evidence for the negative-U centers and valence alternation in amorphous selenium.

The early pioneering first principles MD simulation by Hohl and Jones [80] using Car-Parrinello(CP) method [81] crudely reproduced the pair distribution function and static structure factor for *a*-Se. This gave useful new insights into the structure of the liquid. Bichara et al. [82] have performed a tight-binding Monte Carlo simulation of liquid Se, using a short-range soft sphere repulsion and a moment approximation to the local tight-binding density of state. They found that the Se chains are comparatively short, and a large number of three-fold coordinated Se atoms compensates the number of chain ends, leading to an average coordination number of two. Compared to the results of Hohl and Jones, better agreement of structural properties were achieved in this tight-binding Monte Carlo simulation. However, these theoretical models have contained an unphysical concentration of

well over 10% coordination defects, so that the defects cannot be easily analyzed as isolated entities. Such samples bear only limited relevance to real *a*-Se, in part because this artificial defect-defect interaction causes an unphysical reduction in the localization of the defect wave function. To better connect to experiment, it is necessary to form networks with only a few percent coordination defects and radial distribution function in agreement with experiment. Recently, Kresse et al. [86] made a first principles molecular dynamics investigation of l-Se, with fewer coordination defects than previous theoretical calculations. But the charge associated with the defect was not well defined in their simulation so that it is hard to interpret the dynamics of the energy spectrum with the VAP defect. Our approach is quite novel. We first used the program of Demkov et al. "fireball96" to [84, 83] construct 64-atom network. The pair correlation function, $g(r)$, and structure factor, S(Q), were computed and are in reasonable agreement with experiment. A mixed long chain and Se_6 model naturally emerged from a first principles simulation. This gives strong support for the generally accepted mixed chain and ring model of amorphous selenium since we did not use any *a priori* information about the structure of *a*-Se. More importantly, only one IVAP defect appears in our model and this realistic property helps us not only to understand the electrical density of state and localization of electrical eigenfunction but also to interpret the thermal-disordered and optical induced defect state in the gap in first principles way. It leads to direct confirmation of VAP model.

Realizing that chain structure accounts for the most structural properties of a-Se, we build a zig-zag chain of 216 amorphous selenium model; we use the "fireball96" to refine this chain, namely, we use the standard "cook and quench" method to get the final geometrical structure of a-Se. All the structural properties such as static structural properties $S(Q)$, pair correlation functions $g(r)$ and vibrational density of states (VDOS) are in excellent agreement with experiment data where available. The only defect type for this large system is a valence alternation pair. Based on our model, we found the optical excitation had very significant effect on the structural change in a-Se. All the structural changes in a-Se by thermal disorder and optical excitation can be explained by the VAP model.

5.2 Modeling Methodology

5.2.1 Hamiltonian

We used the program of Demkov, Ortega, Sankey and Grumbach [83] "fireball96" to construct our network. This model generalizes the non-self-consistent local basis Harris functional local density approximation (LDA) scheme of Sankey and co-workers [84] to an approximate self-consistent form. Spherical charged atom densities are used as Harris input fragments, and these charges are self-consistently determined. A minimal basis (one s and three p's per site) is employed. The

method is very efficient combining the advantages of charge transfer with a fixed atom-centered basis (and therefore efficient look-up for matrix elements). The basis functions are slightly excited pseudoatomic orbitals with confinement radii of $.4.63a_B$ for Se. We tried a non-self-consistent (Harris functional) calculation but found that self-consistency was essential to obtain a realistic network because of charged defects. This method has been successful for simulating several other disordered systems: $GeSe_2$[88], a-Si[89], a-GaN[90] and tetrahedral a-C[91].

5.2.2 "Cook and Quench" method to simulate the amorphous system

For the 64 atom amorphous selenium system, we can use the standard "Cook and Quench" method to get a very good small model of amorphous selenium. A cubic supercell of 12.90 Å with 64 atoms placed randomly inside the cube was chosen for the initial configuration of our model. This number gave us a density of 3.91 g/cm^3 corresponding to the liquid Se at ambient pressure at T=573 K. After a thermal equilibration at $T = 300K$ (a-Se), a steepest descent quench was applied to quench the system to $T = 0K$ and therefore a local minimum on the potential energy surface. All of our calculations were done at constant volume using only the Γ point the sample the Brilliouin zone.

A key challenge for first-principles molecular dynamics modeling of the amorphous material is the size of the supercell. Due to the intrinsic order N^3 algorithm for *ab initio* MD calculations, the plane wave *ab initio* MD (due to its *huge* basis set) calculation can only simulate about 100 atoms. From the previous research on the $g - GeSe_2$ [88], the model with several hundred atoms is essential to study the first diffraction peak of structure factor (S(Q)) and vibrational density of state (VDOS). For amorphous selenium, charge transfer played the key role in forming the network structure. This makes full *ab initio* molecular dynamics simulation more difficult since the self-consistency is hard to achieve. To get a larger network (216 atoms) with only a few percent coordination defects and structural properties in agreement with experiment, we built a chain on a lattice random walk as the initial configuration for our model. The algorithm to build the chain is the following: (1) An atom is chosen randomly on a simple cubic lattice. (2) For the second atom of the chain one of the six nearest-neighbor is chosen at the random. (3) Further atoms are added in one of the four nearest-neighbor position of the head atoms that give rise to a bond angle of $\pi/2$ until no appropriate position can be found. (4) Repeat the procedure (1)-(3) until the longest chain was found. (5) Repeat the procedure (1)-(4) for the remaining atoms in the simple cubic cell to find the second largest chain so that the total number of atoms on the chosen chains is equal to the desired number. By using above algorithm, we got two chains with 199 atoms and 17 atoms as our initial model. The standard "cook and quench " method was applied to this

initial model. The initial temperature of the cell was about $4000K$, it was then equilibrated to $2000K$ over approximately 600 fs. The cell was then cooled to $720K$ and equibrated at this temperature for approximately $2ps$. As a final step, the system was slowly cooled to $300K$ over $4ps$ and then quenched to $T = 0K$. Again, we only used the Γ point to sample the Brillouin zone. It also should be noticed that the melting temperature for selenium is between 443 K $\sim$ 490 K and glass transition temperature is 390 K. The supercell with lattice constant 19.35 Å was chosen for the 216 atom model.

5.3 Structural Properties

We now compare our computed short- and intermediate-range correlation functions with available experiment data. The two body correlation functions [pair distribution function g(r) and static structure factor S(Q)] are compared with available experimental data. The three-body [bond-angle, $A(\Theta)$] and four-body [Dihedral angle distribution, $D(\gamma)$] are used to assess the validity of our method modeling the 216 atom amorphous selenium.

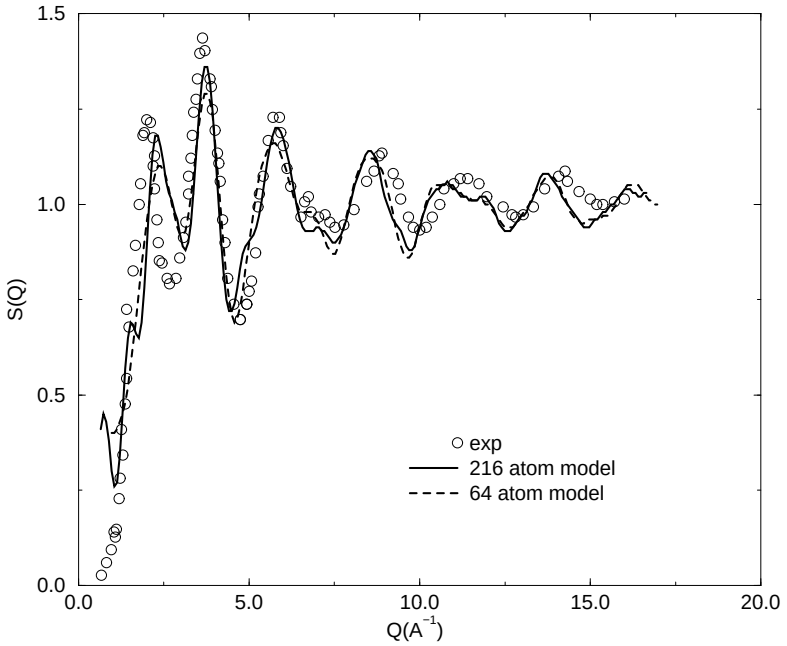

Figure 5.1: Comparison of theoretical and experimental (Ref. [85]) static structure factors S(Q) for 64- and 216-atom *a*-Se model.

5.3.1 Static Structure factor

The structure factor is usually calculated from the Fourier transform of the pair correlation function $g(r)$. In this work, the static structure factor (Fig. 5.1) is computed as

$$S(Q) = 1 + \frac{1}{N}\sum_{i\neq j}^{N}\frac{sin(Qr_{ij})}{Qr_{ij}} \quad (5.1)$$

$$+ 4\pi\rho\left(\frac{r_{max}cos(Qr_{max})}{Q^2} - \frac{sin(Qr_{max})}{Q^3}\right) \quad (5.2)$$

where r_{max} is equal to the half of the side length of the supercell and N is the number of atoms. The term (5.2) is the correction for the scattering in the forward direction with $Q = 0$ which does not contain information about the structure. The $S(Q)$ of the 64-atom and 216-atom model is in reasonable agreement with experiment measurements taken from Ref.[85]. For both these models, the location of principal peaks and intensities are close to the measured ones and even the oscillation between third and fourth peak in the experimental curve is exactly reproduced. The only important discrepancy is the first diffraction peak (FDP). But we can see that the peak position (2.25 Å^{-1}) in the 216-atom model is a little closer to the measured one ($1.91\mathring{A}^{-1}$) compared to the 64-atom model. Compared to the earlier Hohl and Jones' model [80] which gives the position about 2.55 Å^{-1}, our model gave better agreement in position and intensity of the FDP. There is a systematic shift to the

smaller Q value after the third peak in the $S(Q)$ curve, we believe that this shift is related to the position of the first-neighbor peak of pair correlation function. The peak position in our model is about 2.37 Å which is a little bit larger than the commonly accepted value 2.32 Å. Even for this value, there is some inconsistency among different experiments. In fact, the position agrees very well with the experimental $g(r)$ we used from Ref. [85]. Both our 64-atom model and 216-atom model give the reasonable static structure factor for a-Se.

The Hohl and Jones model contains many more defects than our model but the two models yield a similar S(Q). The conclusion is that the $S(Q)$ is little affected by the defect concentration. Recent calculation by Kirchoff et al. [86] indicated that Generalized Gradient Approximation (GGA) may improve the agreement. In a latter section, we will show that a relaxed structure obtained from an expensive but more "accurate" hamiltonian [93] did not show an improvement with respect to the position of FDP.

5.3.2 Pair distribution functions

In Fig. 5.2 we compare the pair correlation function $g(r)$ of our 64-atom model and 216-atom model with the experimental curve. From $g(r)$ the nearest neighbor (average chemical bond length) and next nearest-neighbor peaks are easily determined. The average coordination radii are determined from the position of the first

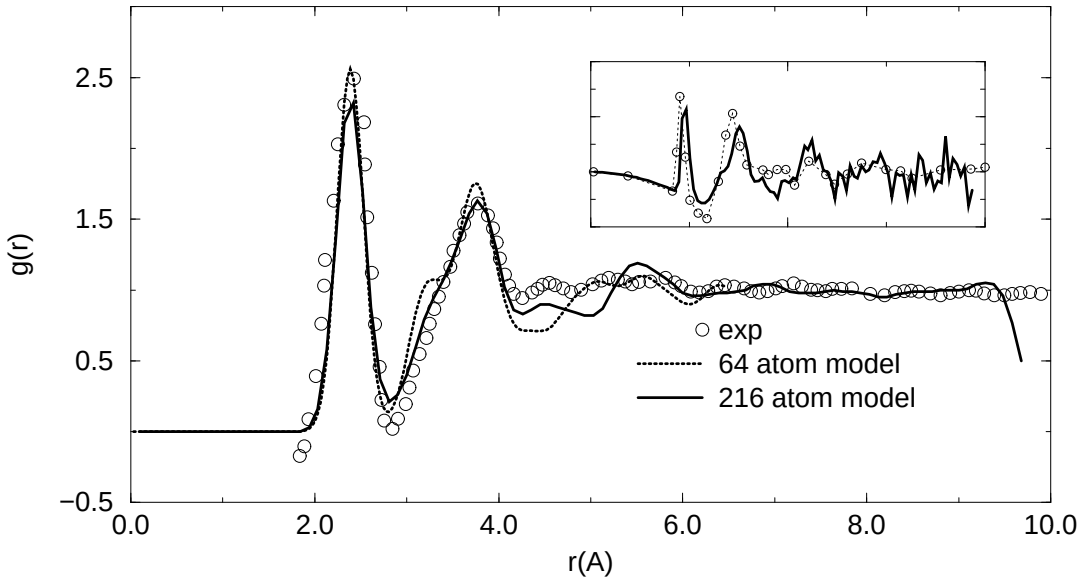

Figure 5.2: Pair correlation function g(r) obtained from MD simulation and experiment for amorphous selenium. The inset shows the $4\pi r^2\rho_0(g(r)-1)$ of 216-atom model compared with experimental curve from Ref. [85, 103, 96]. In the inset, the solid line denotes our calculation and circle is the experimental data. ρ_0=0.02981 $\mathring{A}^3$ is the number density.

minimum. From Fig. 5.2 it is apparent that the average Se-Se bond length of 2.37 Å is quite close to the crystal bond length of 2.32 Å. In our 64-atom model, there appears a shoulder between the first and second peak and this shoulder becomes less apparent in our 216-atom model. We noticed that the shoulder also seen in the Hohl and Jones' calculation as well as Kirchoff et al.'s calculation. A new peak around 5.7 Å which is absent in the experimental curve is shown up clearly in the 216-atom model. However, in the recent X-ray and neutron diffraction study [95], the peak at 5.7 Å is clearly appeared in their result although they did not give any comment. If we plot the pair correlation function in another form which is shown as the inset of the fig.5.2, the major peak positions are in close agreement with the experiment of W. Wei et al. [96]. In table 5.1, we list the principal correlation peaks in our simulation and the experimental data from Ref.[73] and Ref.[76].

Peak number	Henninger et al.[73] X-ray	neutron	Kaplow et al.[76]	our simulation
1	2.33	2.33	2.34	2.37
2	3.73	3.71	3.75	3.77
2a			4.3	4.37
2b			4.7	
2c			5.1	
3´	4.62			
3	5.8	5.74	5.8	5.70
4	7.2	7.25	7.2	7.36

Table 5.1: Principal correlation peaks of a-Se in our simulation and the experimental data. The unit for the reported data is Å

It can be seen from table 5.1, the short range correlation (peak 1 and 2) as well as intermediate range correlation are correctly reproduced in our 216-atom model. The correlation beyond the first two nearest neighbors come from the three-, four- and five-bond neighbors. To our knowledge, our calculation is the first *ab initio* simulation which correctly gives the structure property beyond the first two nearest neighbors.

5.3.3 Bond-angle and dihedral angle distributions

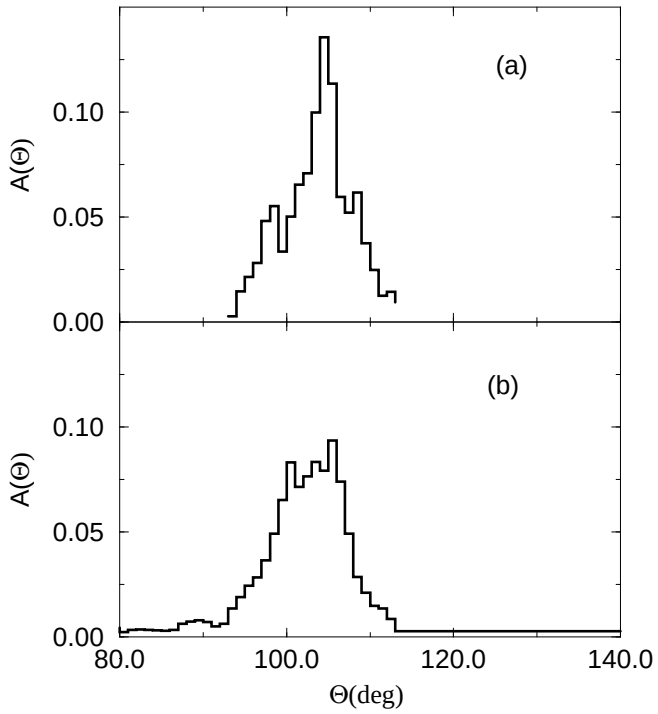

Figure 5.3: Bond-angle distribution function in 64-atom *a*-Se (a) and 216-atom *a*-Se (b).

Fig. 5.3 (a) and (b) depict the bond-angle distribution functions for our 64- and 216- atom model respectively. The first and second peaks in pair distribution functions derived from scattering experiments can be exploited to give a average value of $\sim 105^\circ$ for the bond angle in amorphous Se. The bond-angle distribution in Fig. 3 are consistent with this value. The average bond angle found in our simulation is essentially identical to the bond angle found in the helical chain of t-Se. The result reflects the fact that the amorphous state looks similar to the crystalline from inside a radius of 4 Å. The calculation by Kirchhoff et al. [86] and Hohl et al. [80] showed the similar bond angle distribution function.

We now turn to four-body correlations, which are partly characterized by the dihedral-angle distribution $D(\gamma)$ shown in Fig. 5.4. Both for the 64- and 216-atom model, the dihedral angle γ can assume all values 0° to 180°, with 90° being the most frequent value. Since the dihedral angle cannot be determined directly from experiment, there has been considerable controversy about the possible values of γ in a-Se. The empirical models such as nearly free rotating chains model [77] and tight-binding simulations [82] tended to give the uniform distribution of γ but the first principle investigation by Kirchhoff et al. and Hohl et al. supported the prominent maximum at $\gamma \sim 90^\circ$. The reason is probably that the empirical models only fit the pair correlation function only at the the second nearest-neighbor levels and can not describe the fourth neighbor correlation. The pair correlation functions in

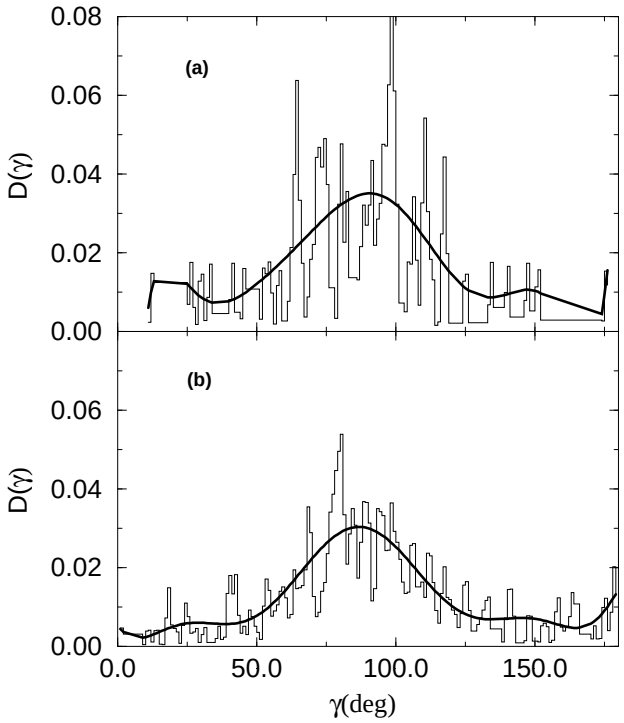

Figure 5.4: Computed dihedral angle distribution $D(\gamma)$ for 64-atom a-Se (a) and 216-atom a-Se (b). The histogram is normalized to the same arbitrary number and the lines are a guide to the eye.

our simulation gives the correct peak positions beyond the second nearest-neighbor distance and thus is more plausible with respect to the dihedral angle distribution.

5.3.4 Atomistic Structure

The comparison of computed g(r) and S(Q) functions with experimental data shows that our simulation gives an accurate picture of local order and distance correlation in *a*-Se. So, we provide the snapshots configurations of our 216-atom network in Fig. 5 to give a micropicture of the structure of *a*-Se. The result of 64-atom network has already briefly reported in Ref. [28]. For the 64-atom model , only two constituents existed in the calculations, a large ring with 56 atoms one of which is a three-fold coordinated defect connecting with another one-fold coordinated defect and one isolated six atom ring. We find that the "distance" between the ring and chain is about 3.05 Å where the shoulder in g(r) appears. The more accurate experimental data of g(r) around 3.05Å is expected to test the correlation between the chain and ring. It is more surprising for our 216-atom model. There are four components in this big model, a very long chain (159 atoms), two shorter chain/ring (28 and 24 atoms respectively) and one 5-atom ring. The long chain connects with a short chain by a three-fold coordinated defect. Recalling that the 216-atom model initially consists of a 199- and 17-atom chain with four dangling bonds, the

appearance of five-atom member ring in this model gives another strong evidence that coexistence of long chain and isolated ring is the right physical picture of a-Se.

The defect atoms are those atoms whose coordination number differs from two. The coordination number of an atom means the number of neighboring atoms within a chosen cutoff distance r_c of the atom. The r_c is taken as the position of the first minimum of pair correlation function g(r) after the nearest neighbour maximum. The defect type in 64-atom model is a bonded pair consisting of a three-fold coordinated atom and one-fold coordinated atom (IVAP) and there are one three-fold coordinated and one-fold coordinated pair (VAP) in 216-atom model. This results in average coordination number of exactly 2 in both of these two models. This also agrees with the diffraction measurements which showed that the atomic coordination number is almost exactly 2 in the low-temperature liquid Se and amorphous Se [85].

5.3.5 Electronic Properties

The electronic density of states diagram is another key to understanding the properties of a-Se. Experimentally, it is believed that there are localized states which induce the shallow electron and hole traps and deep electron and hole traps. The amorphous selenium as well as other chalcogenide semiconductors are free from

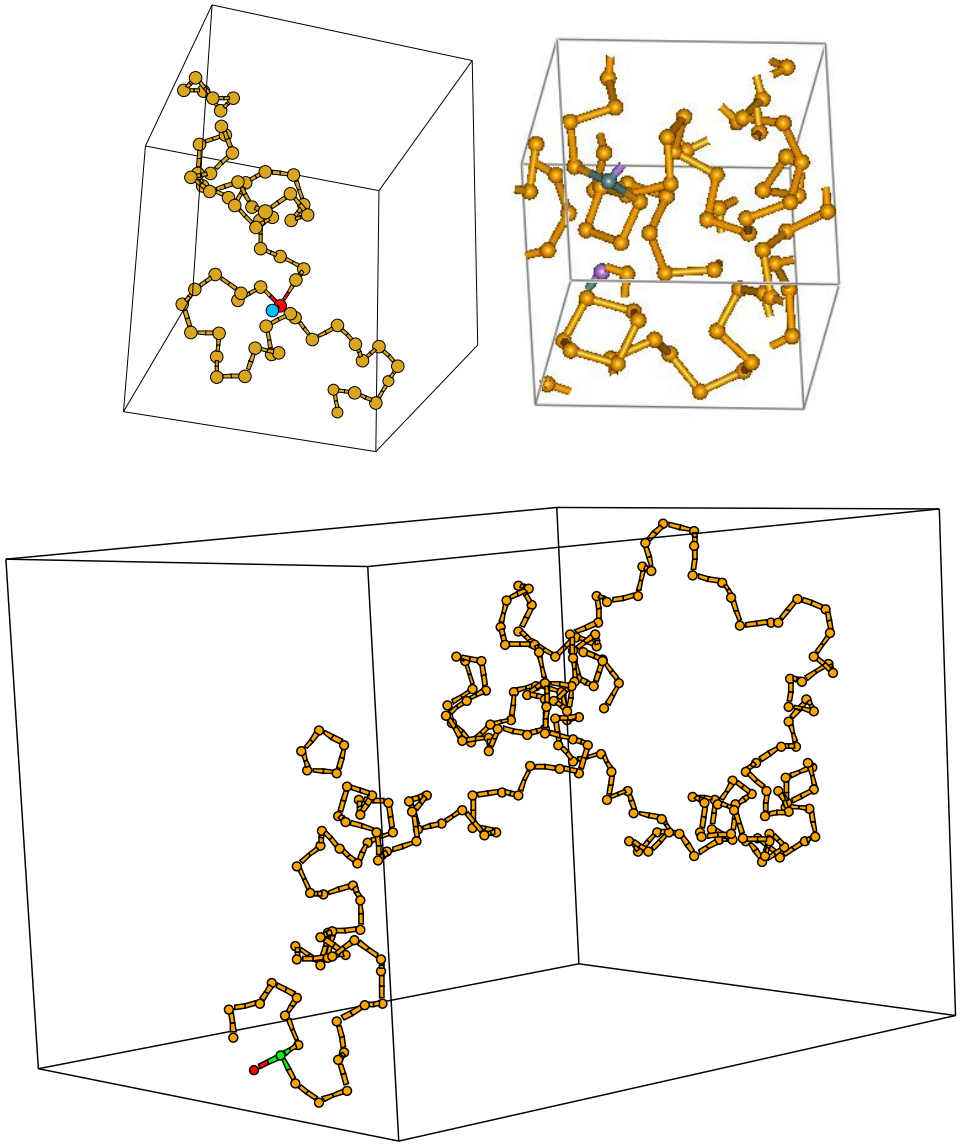

Figure 5.5: Views of typical spatial configuration for 64-atom (top) and 216-atom amorphous (bottom) selenium model. For 64-atom cell, an unfolded structure is also shown to see the correct density. All the bonds are drawn between atoms with separation of $\leq$ 2.7 Å. Bonds to atoms in neighboring cells are readjusted to be connected together so that the topology can be seen.

dangling bonds but suffer from the thermodynamic presence of the valence alternation pair defects. The structural properties and vibrational properties we discussed in previous section showed that our model reproduces the topology of a-Se. More importantly, we will show that the electronic properties in our model can give "first-principle" evidence for valence alternation.

5.3.6 Electronic density of states and inverse participation ratios

The electronic density of states and inverse participation ratio for our 64-atom model has already been published [28]. In our 64-atom model, there is only one IVAP pair. The localized state at the top of the valence band comes almost from the singly coordinated states. The localization at the conduction band edge involves the three-fold site and its nearest neighbors. The important observation for IVAP defect in the 64-atom model is that singly coordinated defect is more localized. This localization agrees with the early tight-binding calculation by Vanderbilt and Joannopoulos [35]. Fig. 5.6 shows the electronic density of states (EDOS) and inverse participation ratio (IPR) of our 216-atom model. The shape of the EDOS for our 216-atom model is quite similar to that of the 64-atom model. There are new features in this big model. Recalling the microscopic picture of the 216-atom model, the two chains are connected by a three-fold coordinated defect leaving one

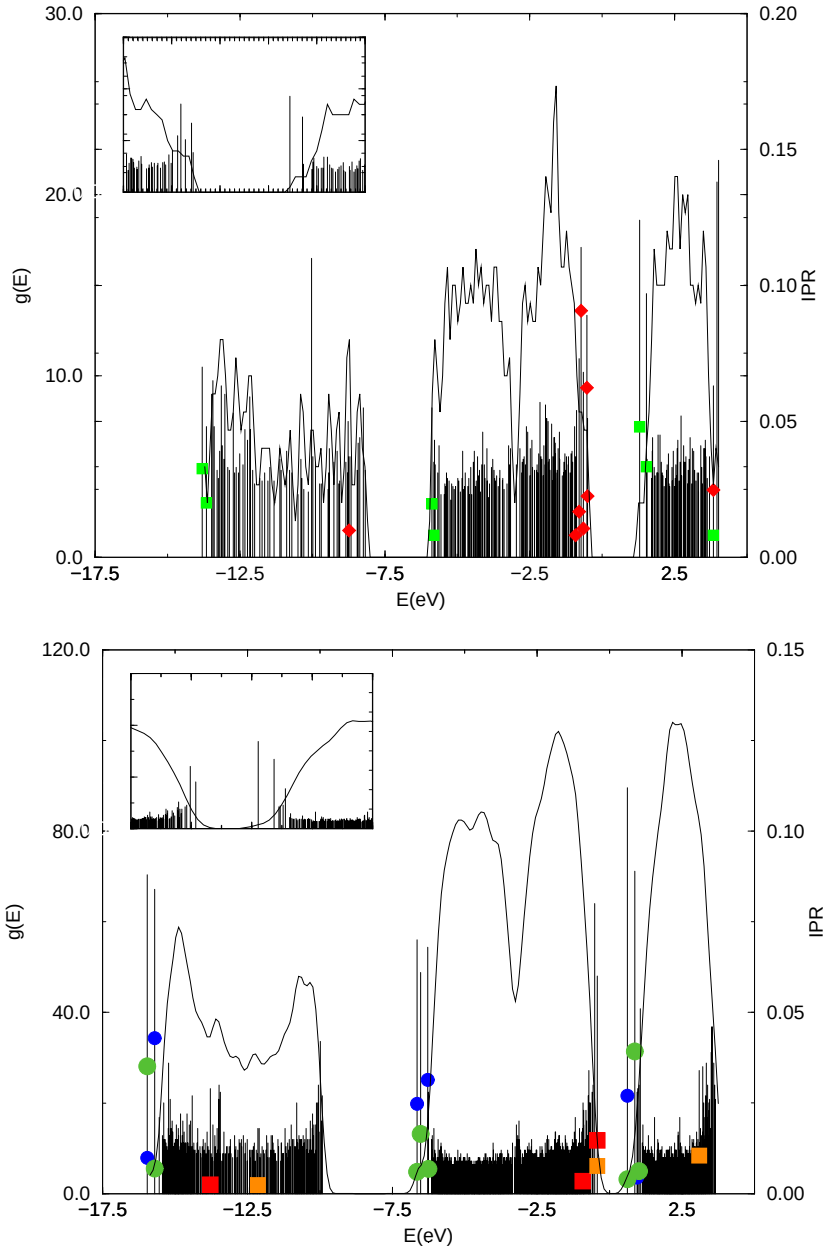

Figure 5.6: Electronic density of states and the inverse participation ratios of 64- and 216-atom *a*-Se models. The inset shows that EDOS and IPR at band gap region. For 64 atom model (a), the diamond stands for the $Q_2(n, E)$ for C_1^- atom and the square stands for the $Q_2(n, E)$ for C_3^+ atom. For 216 atom model, The square shows the $Q_2(n, E)$ for C_1^- atoms and circle stands for $Q_2(n, E)$ for C_3^+ atoms. The $Q_2(n, E)$ are introduced in equation 2.42.

end of the chain as a one-fold coordinated defects. The defect type is a VAP. The localization for the one-fold coordinated defect denoted by the dark-colored square is not as localized as that of the 64-atom model. In our simulation, we found that this one-fold coordinated defect is easy to convert into an atom in another chain to a three-fold coordinated defects and the three-fold coordinated defects can dynamically "decouple" from another chain leaving one atom in another chain as one-fold coordinated defect. This conversion periodically occurs if we consider finite temperature. Geometrically, only one VAP defect appears in our model but actually there are two *dynamically produced VAPs defects* with respect to the role which the defects play in the EDOS. This dynamical conversion of the defects makes it harder for some less realistic models to give a defect analysis. We believe this is the reason why Hohl and Jones concluded that three-fold coordinated defects are the dominant type in the *a*-Se.

The characteristic EDOS can be interpreted by the chemical bonding configuration of selenium. Selenium, having 34 electrons, has six electrons outside of closed shells: two 4s and four 4p electrons. For valence energies, a 4s-like band is fairly well separated from three 4p-like bands. Interactions between nearest neighbors split the p orbital into bonding (σ), lone pair (LP) and antibonding (σ^*) bond orbitals. Interactions between different bond orbitals yield bands which give rise to the conduction and valence bands in the solid [35]. For the case of singly coordinated defect sites, at

least 3 electrons (3 for neutral defect and 4 for negatively charged defects) are in the LP orbital. The stronger direct π interaction will give rise to localized states above and below the lone pair band edges. If the defect is charged, the defect state above the valence band will be filled. Analogous to that for one-fold coordinated defect, *for three-fold coordinated defect* this time there is a pair of σ^* orbitals (and a pair of σ orbitals) which are connected by direct π interaction. The splitting exceeds the band width, and we expect a pair of threefold degenerate localized states [$\pi^*(\sigma^*)$ and $\pi(\sigma^*)$ in our notation] to emerge from the conduction bond edges, and similarly for the valence band. In the case of IVAP defect, the onefold and threefold defects are neighbors. The defect states associated with the two defect sites remain but are shifted closer to the band edges. In our calculations, the distribution of IVAP defect in the EDOS and IPR nicely fit into above analysis. Our first principle calculations of EDOS agrees with the descriptions of IVAP defect state by Vanderbilt and Joannopoulous et al. [35] given in their simple tight-binding models.

5.3.7 *Ab-initio* simulation of defect dynamics with thermal disorder

The EDOS discussed in the previous section is the "zero" temperature energy spectrum. The real EDOS are all measured at some finite temperature. At finite temperature, some states at the middle of the gap were observed and they were

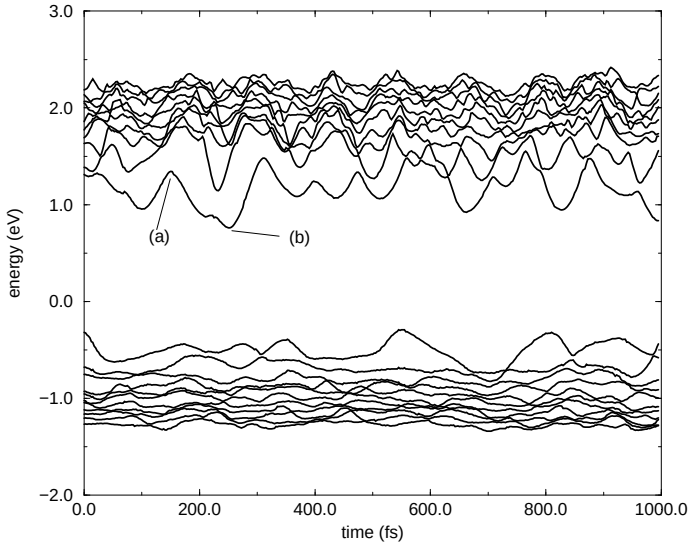

(a) The time dependence of the eigenvalues in the vicinity of the optical gap

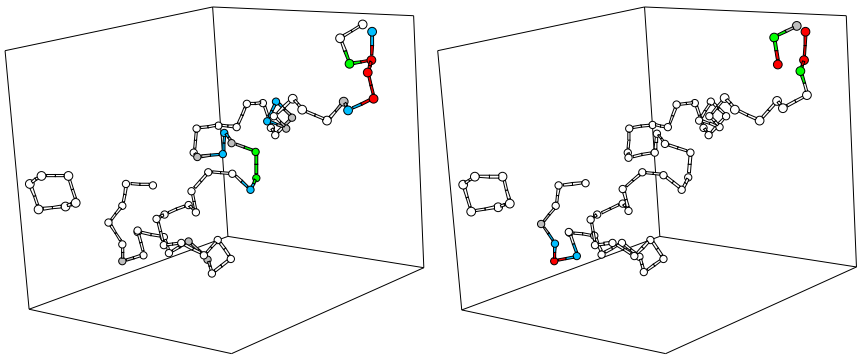

(b) The topological configuration of the supercell and representation of LUMO energy eigenstate at time (a)

(c) The topological configuration of the supercell and representation of LUMO energy eigenstate at time (b)

Figure 5.7: Simulation of the structural change by thermal disorder for 64-atom a-Se model. Color coding reflects different amount of electron charge on a site: Red($q > 0.1$), blue ($0.05 < q < 0.1$), green($0.01 < q < 0.05$) and white ($q < 0.01$). q is the total charge on the site. This charge summed over all sites is unity in all cases.

assigned as deep trap states. These dynamically derived states are studied from the thermal fluctuation of the energy level fluctuation near the band gap and the associated structural change from thermal fluctuation. Fig. 5.7(a) is the time dependence of the eigenvalues in the vicinity of the optical gap for our 64-atom model. The Fermi level is near the middle of the gap. The Lowest Unoccupied Molecular Orbital (LUMO) fluctuates in time by about 0.8 eV (the difference between the maximum value and minimum value), much larger than the thermal energies ($\sim$ 10 meV). The eigenvalue of LUMO at time (a) is mostly derived from the three-fold coordinated defect and the eigenvalue at time (b) is less localized. Fig. 5.7(b) and (c) are the supercell and the representation of the LUMO energy eigenstate at time (a) and (b) respectively. It can be clearly seen that the energy fluctuation is correlated with lattice dynamics. This relaxation is conveniently understood by the charge transfer during the thermal disorder. At zero temperature, we find that the atoms at the singly coordinated defect site and three-fold coordinated site carry $-0.2e$ and $0.2e$ net charge, respectively. The net charge of the IVAP pair is zero. At time (a), the LUMO is mostly obtained from positively charged three-fold coordinated defects. However, if this C_3^+ defect traps an electron without relaxation, the energy will not fluctuate. In real situation, if the C_3^+ defect atom obtains an electron, the C_3^+ defect environment cannot be maintained and it will relax to the structure optimum to the C_3^0 defect environment. Our simulation clearly reveals this structure relaxation as indicated in Fig. 5.7(b) and (c). To further enhance our point, in

Fig. 5.8(a), we plot the charge associated with the C_3^+ defects against simulation time and the corresponding LUMO as a function of time. The fluctuations between the LUMO and the C_3 defect charge are almost in phase. The increase of the charge ($C_3^+ \rightarrow C_3^0$) causes the LUMO to extend to the middle of the gap. Similarly, for the case of one-fold coordinated defect, the C_1^- defect will emit an electron and this will make the highest occupied molecular orbital (HOMO) shift to the middle of the gap. This gap state will be observed in the real situation if the sample is quenched fast enough and the "not completely" annealed stated will be frozen in the final structure. Since the lattice relaxation for three-fold coordinated defect involves more atoms, the fluctuation for LUMO is larger than that for HOMO.

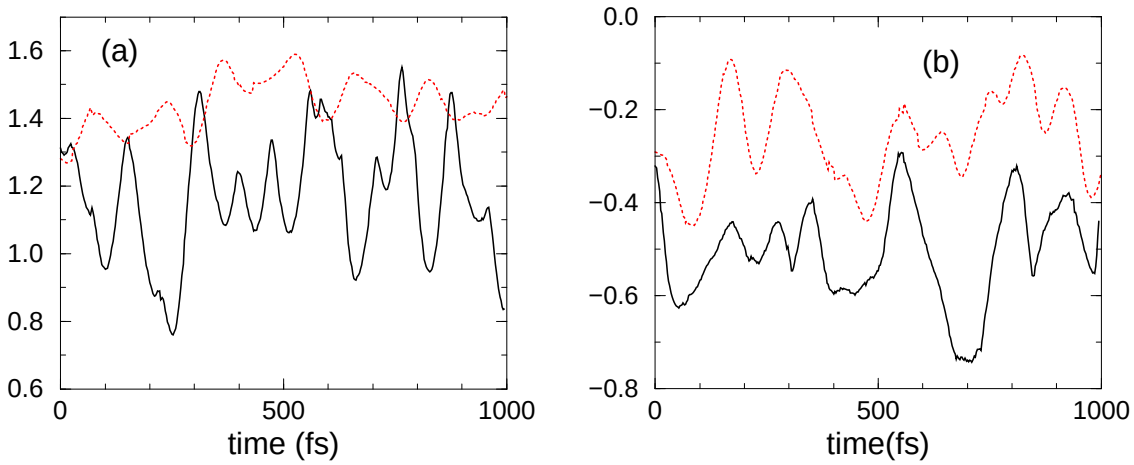

Figure 5.8: The correspondence between charge fluctuation and energy eigenvalue fluctuation. (a) The solid line denotes energy for LUMO and dotted line represents the charge (net charge+1) associated with three-fold coordinated defect. (b) The solid line denotes energy for HOMO and dashed line represents the charge associated with one-fold coordinated defect.

5.3.8 Vibrational denstity of states

The dynamical properties of our model are analyzed through the vibrational density of state(VDOS). Here, I just give the VDOS compared with experimental data to assess the quality of model.

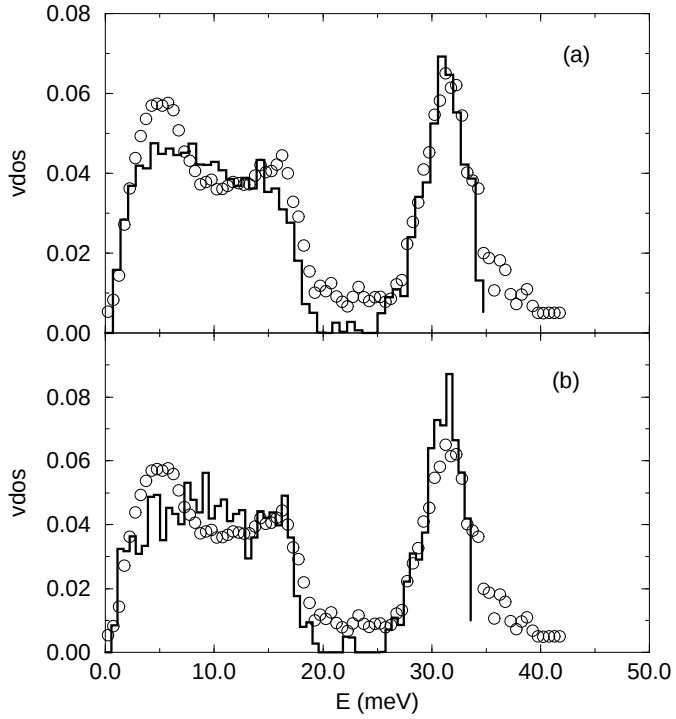

Figure 5.9: Vibrational density of states: histogram theoretical model; open circles experimental data from Ref. [35]; (a) for 216 atom model and (b) for 64-atom model

The vibrational energies were obtained from the dynamical matrix. The dynamical matrix is determined by displacing each atom by 0.03 Å in three orthogonal directions and then performing *ab initio* force calculations for all the atoms for

each such displacement. Each such calculation yields a column of the force constant matrix[97]. The vibrational eigenvector and eigenvalues of the supercell was then easily obtained. Only the Γ point of the phonon Brillouin zone is sampled. The VDOS was determined from the eigenvalues by summing Gaussians centered at each eigenvalue; each Gaussian had a full width half maximum corresponding to the energy-dependent experimental resolutions [98] The vibrational density of states of a-Se has been studied using inelastic neutron scattering by Kamitakahara et al. [98]. and in fig. 5(a) and (b) we compare our VDOS with their experimental measurement. The agreement between the experiment and our simulation is very good. Even the spectrum at the $20-30meV$ region is reproduced in our simulation. The lowest frequency modes (less than $6meV$) are acoustic. Phillips et al. [99] associated them with bond torsion excitation. The high frequencies are due to the bond stretching and the frequencies in the middle of the spectrum are due to bond bending.

5.4 Discussion

5.4.1 Structural properties

The static structure factors in both our 64-atom model and 216-atom model agree reasonably well with experiment values. The 216-atom model is a little bit

better. There is still some discrepancy with measured one in the position of the first diffraction peak. The recent generalized gradient approximation (GGA) calculation [86] gave a better agreement with experiment for the liquid selenium. So, it is assumed by Kirchoff et al. that GGA is essential to mitigate these problems primarily by getting the proper interatomic distance. We have verified that our Hamiltonian gives a dimer bond length of 2.18 Å which is close to the experimental length 2.17 Å. We noticed that the improvement from GGA calculation by Kirchoff et al. is from decreasing the depth of the first minimum in the pair correlation function $g(r)$ which is much higher in the LDA calculation as well as the in the Hohl and Jones calculation. To verify this point, we did two studies. First, we use a steepest descent quench to fully relax Hohl and Jones' network with our Hamiltonian [83]. To our surprise, quenching decreases the first minimum of $g(r)$ and the resulting $g(r)$ is in improved agreement with experiment. The static structure factor does not change significantly especially in the first diffraction peak region. The relaxed model only contains a bonded $C_3 + C_1$ IVAP pair and a pair C_3 and C_1 (VAP). This structure results in an average coordination number of 2, a strong signature of dominance of VAP type defect in a-Se. Second, we use the "full blown" first principle MD program, SIESTA, [93] to relax our 64-atom model. We include the GGA correction, double-zeta and polarized orbitals to quench our 64-atom model. However, we did not observe the improvement to the structural properties of our model by this expensive calculation.

Ours is the first calculation to compare the structural properties beyond the second nearest neighbor distance. These correlations beyond the second nearest neighbor in amorphous selenium need to be studied with large models. In our simulation, the 216-atom model has already shown the better description for the correlation beyond the second neighbor compared with 64-atom model. In fact, Kaplow pointed out that the experimental correlation function exhibits correlations at distance up to about 10 Å[76] for *a*-Se. Wei et al. [96] showed that the correlation in *a*-Se extending out to a radius for 13 Å has contribution to intensity of the first diffraction peak. The agreement with the experimental data for our 216-atom model indicate that using some *a-priori* knowledge of the amorphous material is of key importance for modeling the amorphous material. To completely fit the experimental structure factor, a supercell with a side length about 24 Å which corresponding 400-atom model is needed. To our knowledge, the first principles simulation using the plane wave as basis is impossible for such a large system. The empirical tight-binding simulation give the uniform dihedral angle distribution for *a*-Se indicating the tight-binding simulation gave a poor account four body correlations.

The mixed ring and chain model now is generally accepted as the microscopic model for *a*-Se. The ring and chain components in *a*-Se naturally appeared in our first principles simulation without any *a priori* information about the existence of ring in *a*-Se. The important question here is: what is the ring-chain ratio in *a*-Se?

The difference between the chain length in our 64 atom model and 216 atom model indicate that a larger model is needed to answer this question.

5.4.2 Electronic Properties

Since we use self-consistent methods with charge transfer properly accounted for, the charge on the defect atoms are properly described in our model. In our 64-atom model, we find that the atoms at the singly coordinated defect site and three-fold coordinated site have $-0.2e$ and $0.2e$ net charge respectively. The net charge of the IVAP pair is neutral. This agrees with the prediction of Kastner et al. In the process of forming the a-Se, in addition to the atomic rearrangements accompanying the above configuration changes, there are relaxation effects associated with a change in charge state. Self-consistency with charge transfer plays key role on forming defects in a-Se. In our 216-atom model, the only defect pair is VAP rather than IVAP. We observed that one-fold coordinated defect and three-fold coordinated defects have $-0.14e$ and $0.14e$ net charge, respectively. The charge of the defect atom for VAP is less than that of IVAP. This is not surprising since the one-fold coordinated defect in the VAP pair can interact with other atoms in another chain and convert to the three-fold coordinated defect. We believe that IVAP and VAP both exist in the a-Se depending on the different preparation condition.

The large fluctuations for the LUMO and HOMO are explained by the charge fluctuation. The charge fluctuation will cause the defect sites to adjust its configuration to accomadate the charge gain or loss. Very recently, Drabold et al. [100] found that localized electronic states are very sensitive to moderate amounts of thermal disorder for amorphous silicon. The pattern in the energy fluctuation in our model is quite similar to that of amorphous silicon. But the thermal effect is much larger in *a*-Se since this thermal variation will cause the topological structure change for the network.

5.5 Does a more accurate Hamiltonian result in a better structural model?

5.5.1 Introduction

We have seen in the introduction: the most realistic amorphous silicon model was built using the very *simple* Keating potential [9] and recent progress on obtaining better model for *a*-Si by Barkema and Mousseau was also based on a rather inaccurate Stiilinger-Weber potential [3]. WWW method and ART technique aim at the bottleneck of the computer simulation of the material - time scale problem. In

this sense, ample annealing and careful quenching during process of modeling amorphous material is more important than selecting the most accurate Hamiltonian. The advantage of the Fireball simulation shows the advantage in these respects: (1) Fireball is an *ab initio* method so it does not require additional parameters. (2) The real space method and Fireball basis makes the simulation of Fireball more like a tight-binding simulation allowing large system to be modeled. (3) For some system, especially chalcogenide amorphous materials, there is evidence showing that constraint of perfect local coordination may be broken. As a consequence, the empirical potential is very hard to construct and even the ART technique needs the force between atoms evaluated by the density functional theory calculation. In this section, we want to show that once a structural model was built by the Fireball calculation, the structural model has very little room to be improved by more accurate Hamiltonian.

5.5.2 Crystal Structure of t-Se by SIESTA[93]

t-Se has a hexagonal Bravais lattice, with three atoms in the primitive cell. Let a is the hexagonal basal edge and c is the vertical edge of the prism. The atoms are arranged along helicoidal chains, which wind an angle of 120° between first neighbors. The atoms in a given chain are covalently bond to a third atom (second neighbor) on a parallel chain. So, the atom on t-Se has a strong covalent bond with

first neighbour and weak bond with second neighbour. Some literature suggests this is a kind of exotic bond and t-Se serves as a benchmark for testing the performance of theoretical model.

SIESTA[94] can use both LDA and GGA functionals, including spin polarization. The one-particle problem is solved using linear combination of atomic orbitals (LCAO). There are no constraints either on the radial shape of these orbitals which are treated numerically or on the size of basis, allowing for the full quantum chemistry knowing multiple-ζ, polarization, diffuse orbitals. To calculate the Hamiltonian matrix elements, SIESTA uses "fireball" basis orbitals which strictly vanish beyond a cut-off radius (R_C).

To model t-Se with SIESTA, the first step is to construct a reliable pseudo-potential. I chose the TM2 scheme to construct the pseudo-potential. The pseudo-potential has been discussed in the chapter 2.

Table 5.2 indicates that SIESTA can calculate the t-Se property with the same accuracy as the plane wave calculation. Especially, the more accurate the Hamiltonian is (larger plane wave cut-off, DZP basis), the closer the result it to experiment. We found if we choose the plane wave cut-off for three-center integrals 200 Ry, R_c=7.4 Bohr and DZP basis, SIESTA can almost reproduce all the crystal properties of t-Se. This is a converged calculation. We also plot the band structure of t-Se with those parameters. Fig. 5.10 shows the band-structure and density of state

Model	Plane Cut-off(Ry)	$\Omega(\mathring{A}^3)$	c/a	a($\mathring{A}$)	c ($\mathring{A}$)	
EXP		27.27	1.136	4.36	4.96	
LDA-DZP	150	23.58	1.3	3.96	5.15	
LDA-DZP	200	23.24	1.27	3.98	5.06	
GGA-DZP	50	27.92	1.23	4.19	5.16	distorted
GGA-DZP	100	25.54	1.14	4.42	5.06	distorted
GGA-DZP	150	28.25	1.19	4.33	5.15	
GGA-DZP	200	27.96	1.15	4.37	5.06	
GGA-SZP	200	27.01	1.19	4.27	5.09	
GGA-SZ	200	27.88	1.31	4.17	5.48	
LDA-VJ[a]		22.40	1.24			
LDA-ACA[b]		24.84	1.21			
LDA-NC[c]		23.59	1.29			
LDA-US[d]		23.16	1.30			
PB-US[e]		29.11	1.14			

Table 5.2: t-Se crystal properties calculated by SIESTA and comparison with experiment as well as other theoretical calculations. Results[abcde] are compiled in Ref. [101]. [a] LDA with Wigner exchange-correlation functional. [b] LDA with Perdew-Zunger exchange-correlation functional. [c] norm-conserving pseudopotentials and LDA with Perdew-Zunger exchange-correlation functional. [d] ultrasoft pseudopotentials and LDA with Perdew-Zunger exchange-correlation functional. [d] ultrasoft pseudopotentials and Perdew-Becke (PB) generalized gradient corrections.

for t-Se. The indirect band gap in our calculation is 1.04 eV which is very close to the experimental value 1.20 eV. To our knowledge, the crystal structure and band structure for t-Se in our calculation is one of the most accurate calculations to date. So, we are confident that we have a very reliable Hamiltonian for a-Se to perform a very accurate calculation for selenium.

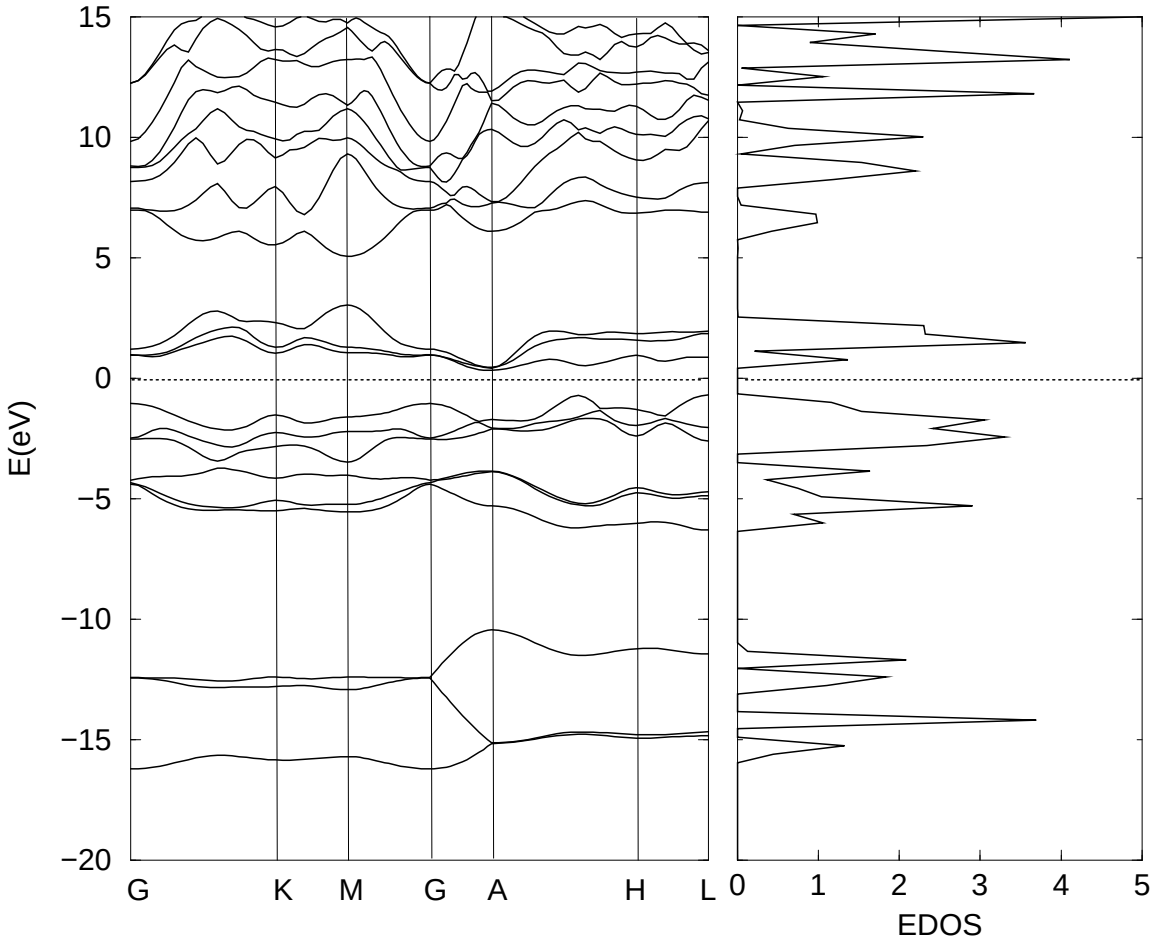

Figure 5.10: band structure and electronic density of state for t-Se.

5.5.3 *a*-Se model from SIESTA

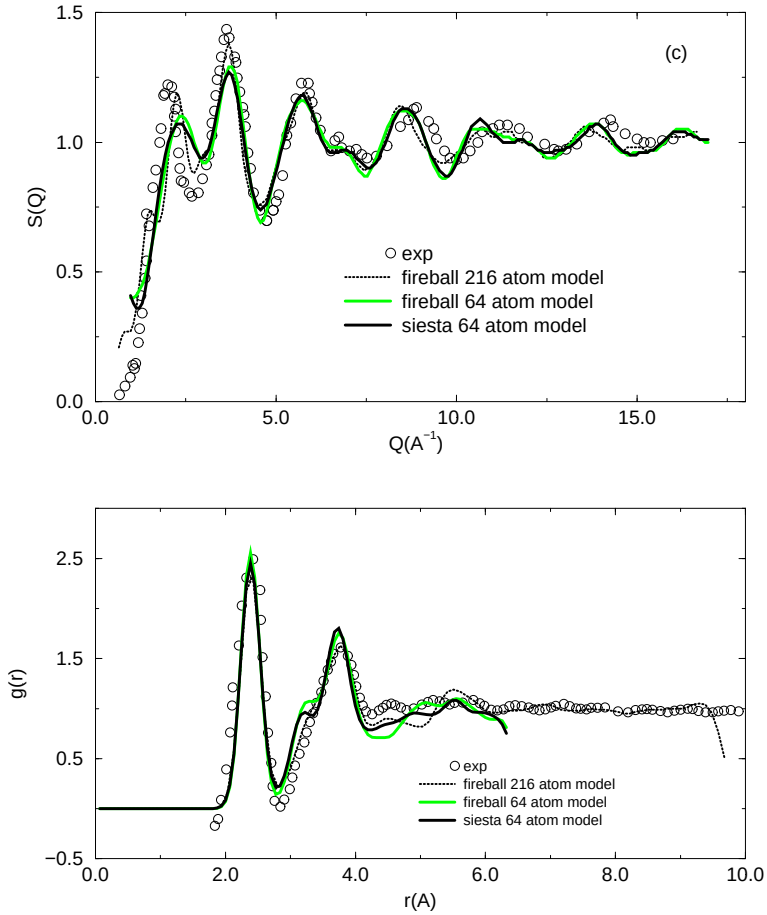

Figure 5.11: The static structure factor (a) and pair correlation function(b) of 64 atom *a*-Se from siesta, 64 atom *a*-Se from fireball and 216 atom *a*-Se model from fireball and experimental value

After we obtained the parameters to calculate the t-Se, we can employ the Hamiltonian to relax our *a*-Se model. Fig. 5.11 illustrates the structure factor and pair correlation function for a 64 atom model got from SIESTA and the comparison with the experiment and 216 atom model and 64 atom model from Fireball. We found

this expensive calculation with more accurate Hamiltonian achieves very little for the structural properties of t-Se. However, the CPU time spent on this calculation is more than 10 times longer than the time using fireball. In this respect, we again assert that "accurate" Hamiltonian is not the most important issue in modeling the amorphous materials. The key issue is the infinite time spent on searching the optimal structure from the possible configurations which increase exponentially with the size of the system.

5.5.4 VAP defects are spin-unpolarized charged defects

Although there is no gain for the structural properties of *a*-Se using the state of art density functional code SIESTA, some important questions of defect properties of *a*-Se can be answered by SIESTA. In our 64 atom model, there is an IVAP defect. The question is whether three-fold coordinated defect is positive charged and one-fold coordinated defect is negative charged and if they are charged defects, whether they carry net spins. To answer these questions, we perform a spin-polarized calculation for the 64 atom *a*-Se model. To develop our point, we also did a spin polarized calculation on a 17 atom cluster selenium model with an IVAP defect. Table 5.3 shows the charges of the atoms at defect sites. For comparison, we also list the charges of atoms (number 1 for 64 atom *a*-Se and number 1 for 17 atom selenium cluster) at normal region. It is quite clear from table.5.3 that the the

Config.	atom	coord.	total	spin up	spin down	net polarization
64 atom	44	3	5.890	2.945	2.945	0.
a-Se	29	1	6.118	3.059	3.059	0.
	1	2	6.006	3.003	3.003	0.
17 atom	6	3	5.864	2.932	2.932	0.
cluster	17	1	6.154	3.076	3.076	0.
	1	2	6.014	3.007	3.007	0.

Table 5.3: Mulliken charge, spin polarization of the defect for 64 atom a-Se model and 17 atom selenium cluster

positive defects are overcoordinated and the negative defects are undercoordinated. Moreover, the charged defects carry no net spin as evidenced by the same amount of spin-up and spin-down component at the defect sites.

5.6 Summary

We performed a first principles molecular dynamics simulation for 64-atom and 216-atom amorphous selenium. The resulting structure factor and pair correlation function are in good agreement with experiment data where available. The method to modeling the 216-atom model is quite unique. We first use some *a priori* information of a-Se and build a zigzag chain as the initial configuration. The final network turns out to be in excellent agreement with available experiment data including the vibrational density of states. In both our model, the ring component in a-Se was naturally came out indicating mixed ring and chain structure is the microscopic structure for a-Se. Both in our 64-atom and 216-atom model, the only defect is VAP

and IVAP. The calculation gives the strong evidence of valence alternation pairs in amorphous selenium.

The thermal disorder was studied in our 64-atom model. The thermal disorder can cause charge transfer among the atoms in the network and this charge transfer will cause the topological structure change for defect sites.

Chapter 6

Direct molecular dynamic simulation of light induced structural change in amorphous selenium

6.1 Introduction

In this section, we report the first *ab initio* study of light induced effects for *a*-Se. Our study of these important properties is made possible by use of *ab initio* MD

in conjunction with a new algorithm for obtaining a model of *a*-Se. The resultant *a*-Se structure contains only one VAP defect and the structural properties including static structural properties S(Q), pair correlation function, electronic and vibrational density of states are in good agreement with experiment [85, 98]. Bond breaking and recombination of the structure due to optical excitation are directly simulated using this model. The signatures of photostructural change are in impressive agreement with the VAP model and recent experiment, though the process is less local than one usually imagines with the VAP model.

6.2 Method to simulate the photo-structural change

We used the program of Demkov, Ortega, Sankey and Grumbach [83] "Fireball96" to construct our network and use approximate Kohn-Sham orbitals as if they were "genuine" electron states. For the details of this method, the reader is referred to Ref. [83],[84]. The method has been used previously to form a small model of *a*-Se[28]. The use of Kohn-Sham states is not fundamentally justified, though there are many computations that show that this can be useful[102]. Indeed, it is of some independent interest that these approximate and generously interpreted orbitals capture the physics quite well as we show below. We think this is because the effects we report here do not depend on particularly subtle features of the electronic structure.

We have discussed our method to construct *a*-Se model and the structural properties such as pair correlation function, static structural factor and vibrational properties in chapter 5. We stress that our model is in *uniform* agreement with structural, vibrational and electronic measurements. For comparison, we also discuss light-induced effects in our earlier 64 atom model[28]. In our 64-atom model [28], there is only one IVAP. The localized state at the top of the valence band comes almost soley from the singly coordinated sites. The localization at the conduction band edge is predominantly on the three-fold site and its nearest neighbors. The important observation for IVAP defect in the 64-atom model is that the singly coordinated defect is more localized. This agrees with the early tight-binding calculation by Vanderbilt and Joannopoulos [35]. The density of electron states and the localization of defect eigenvectors of our 216-atom model is similar to that of the 64-atom model[28].

The photostructural changes in chalcogenide glasses have been the subject of numerous investigations but the microscopic mechanism of such changes still remains unclear. If a model contains too many defects, it is hard to disentangle the structural change induced by optical excitation or other factors such as thermal disorder etc. In fact the whole process does not happen without states nearly localized in the gap. Our models contain the fewest defect sites and as such, provide a suitable starting point for modeling the light-induced structural changes in *a*-Se.

We use the method developed by Fedders, Fu and Drabold[39] to simulate the light-induced structural change. First, we transfer the electron occupied at the HOMO to the LUMO level[104]. In the real material, this change in the charge state of a localized state could be due to an electron ejected from the valence band to the conduction band by a photon. Then we let the system evolve freely without either adding or taking away energy. We found that the initial local disturbance of the atoms kept propagating outward. We let the supercell evolve for $400fs$ and observe how the topology change during this optical excitation. $400fs$ was found to be adequate for the network to relax in order to accommodate the change in charge state. We also repeated all this with constant temperature MD (300K) and found that the results were essentially identical.

6.3 Simulation of photostructural change in a-Se

Fig. 6.1(a) and (b) show the structural change during simulation for 64 atom model. We found that the one-fold coordinated defect was converted to a three-coordinated defect in the region where defect sites are located. The structural change was nonlocal. Adjacent to the initial IVAP, two bonds were broken and two of the resulting defect atoms formed a new bond. One of the new defects converted to a three-fold coordinated defect and the other remained a one-fold coordinated defect. The fact that the original one-fold coordinated defect site was converted

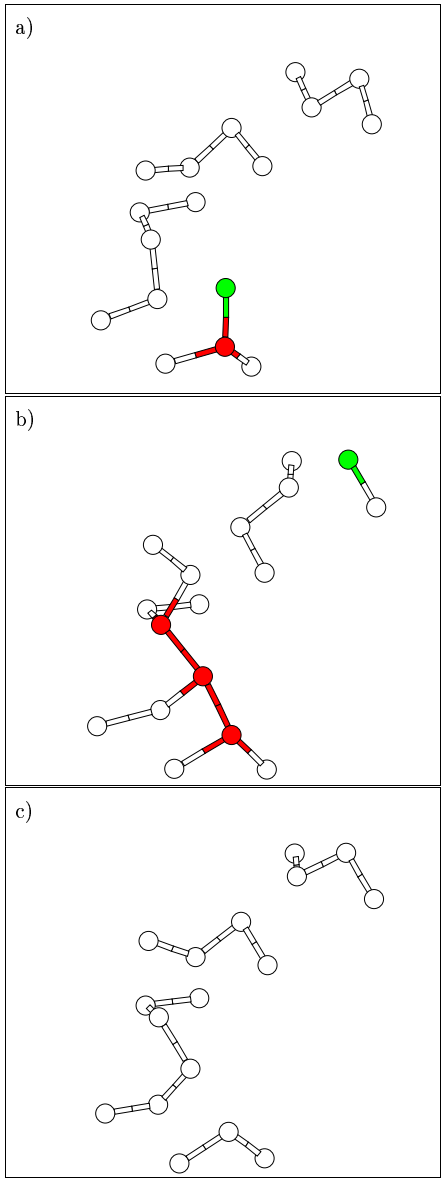

Figure 6.1: Simulation of the structural change by optical excitation. The atoms involved the structural change (a) before the optical excitation (b) at the end of the optical excitation and (c) after quenched back to the energy minimum. The gray scale in this figure represents the types of coordination of each atom: white, two-fold coordinated atom; light dark, three-fold coordinated atom; deep dark, three-fold coordinated atom.

to the three-fold coordinated defect site is just another prediction by VAP model. Since the negatively charged one-fold coordinated defect atom become neutral C_1^0 by the optical excitation, this C_1^0 is not very stable and it tends to convert to C_3^0. The change in the other region is also easy to understand if we assume the C_3^0 defect to be the most probable neutral defect in *a*-Se. *The local disturbance in the defect region will first cause bond breaking producing some* C_1^0 *defects, these* C_1^0 *defects have tendency to become* C_3^0 *defects.* Thus, it appears that the key to understand the structural change by optical excitation is to admit the assumption that C_3^0 is the most stable defect in *a*-Se. This is probably the most important assumption in the VAP model by Kastner et al. [7]. We computed atomic charges using a Mulliken analysis and find that one-fold atoms are negatively charged (depending somewhat on the local environment, a charge of 0.07-0.1e is transferred); three-fold atoms are positively charged and by a similar amount. Two-coordinates sites have a typical charge of magnitude less than $\approx$ 0.02e. We performed tests with DMOL[105] and found semiquantitative agreement with fireball charges for a 17 atom Se molecule with an IVAP.

Fig. 6.2(a) and (b) shows the photostructural change for 216-atom model. Similar to 64-atom model, the one-fold coordinated defect converts to a three-fold coordinated defect. A majority of photo-created defects are three-fold coordinated suggesting that these are the most probable neutral defects in *a*-Se. It is interesting

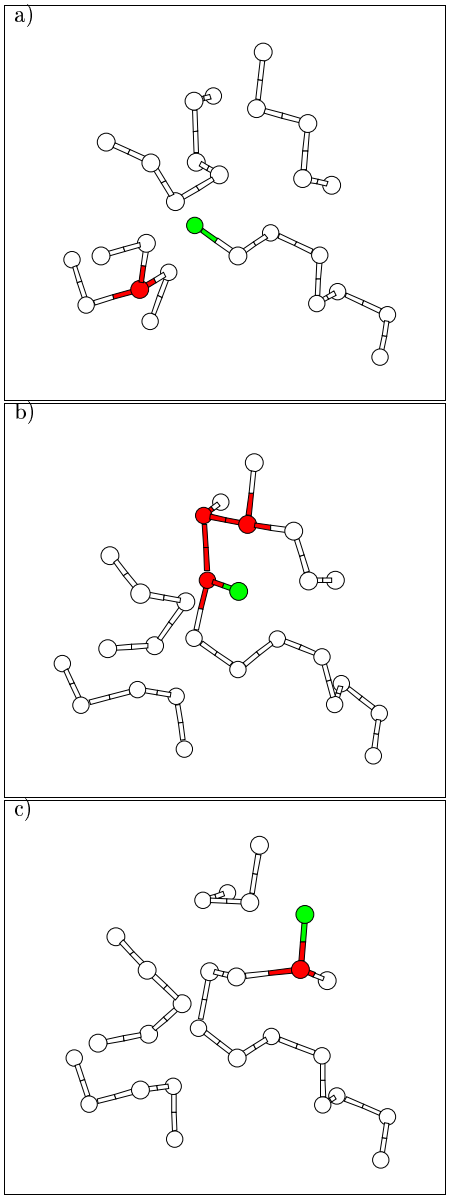

Figure 6.2: Simulation of optical excitation for 216 atom model. Same grey scale as Fig 2.

that three-fold coordinated defects tend to cluster together. This phenomenon was also observed in the calculation of Hohl et al. [80]

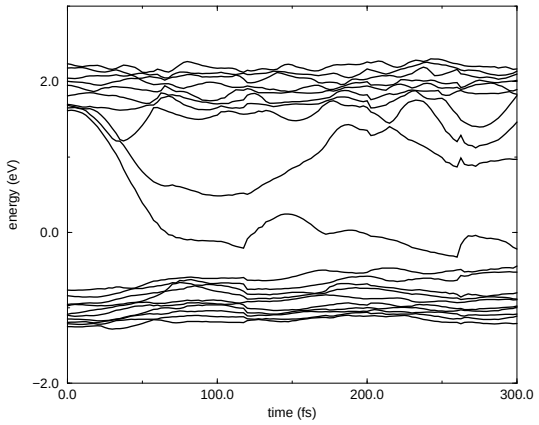

Figure 6.3: The time dependence of the eigenvalues in the vicinity of the optical gap during the process of optical excitation

We have found that in both the 64 and 216 atom models, that the HOMO and LUMO levels move into the middle of the gap during the photoexcitation process. This is readily explained by the VAP model.

The next step is to de-excite the electron and then quench the sample. It is striking that all the defects disappear after we quench the system to an energy minimum for 64-atom model. This structural change is shown in Fig. 6.1(c). This structural change then reveals one possible outcome, an interesting "optical annealing", rather akin to light-induced crystallization. For 216-atom model, as shown in Fig. 6.2(c), the original VAP defect disappears and a new IVAP defect is formed.

We repeated the same MD simulations for above processes without optical excitation. We use the same parameters, time step and quench rate except that we did not remove the electron from our system. After we let the system freely evolve for $400fs$ and quench it back. The structure is the same as the original structure. This indicates that the structural change in our first simulation is really induced by optical excitation.

The optical excitation has a profound effect on the structural and electronic states of a-Se. One important implication in our light induced effects is that neutral C_3^0 defect is easy to form. These C_3^0 defects will be frozen in the material if the system was quenched with very fast rate. This result can explain why most of the theoretical calculation and some experiment showed that the coordination number for a-Se is slightly larger than 2.

6.4 Dynamical Bond Formation and Light induced Electron Spin Resonance in a-Se [30]

Recent experiments on optically induced ESR by Kolobov et al. [8] gave strong support for the negative U. They observed that the ESR-active defect centers were

created by breaking the inter-chain bonds under photo-excitation. They also observed fast and slow ESR signals for the film previously irradiated for several hours and then annealed at low temperature.

In previous section, we showed that major structural change for a-Se occurs near the defect site and that the photo excitation will anneal the defect or cause defect diffusion. This work also supports the idea of the "negative U". The defect sites are most sensitive to light exposure because it is states (near E_F) localized in their vicinity, which suffer light-induced occupation change (and therefore local change in forces). In this section, we want to further study how defects are created by light excitation. Particularly, we want to link our theoretical molecular dynamics simulation to the recent experiment by Kolobov et al. We first explain the physical mechanism of the dynamic inter-chain bonds formation under the photo-excitation. Then we study how the defect was created by photo-excitation which can help us understand the fast and slow LESR components observed experimentally.

We use two models to study light induced structural change for selenium. The first model consists of two infinite parallel chains of Se. The chain model was constructed by selecting two infinite chains from trigonal Se, breaking the periodic boundary condition perpendicular to the chain direction and relaxing this structure using *ab inito* MD simulation. The bond angle, dihedral angle and bond distances are consistent with other calculations. The second model is a defect free amorphous

selenium model. This 64 atom a-Se model was first constructed by doing "cook and quench" for a random 64 atom Se configuration by *ab inito* MD simulation. The initial model contains a intimate valence pair (IVAP) defect. The model was further annealed by light excitation and *became a defect free model [29, 28].*

Photo excitation was simulated by using the same approach as that introduced before[29, 106]. During the MD simulation, we transfer the electron occupied at the highest occupied molecular level (HOMO) to the lowest unoccupied molecular level (LUMO). We imagine this change in the charge (or occupation) of a localized state as a simple model of an electron promoted from the valence band (in this paper just the HOMO level) to the conduction band (LUMO level) by the photon.

The process of the photo-structural change of the parallel chain is shown in Fig. 6.4. The process can be understood in two stages. The first step is the defect creation process. This process lasts around 250 fs as indicated by Fig. 6.4a - e. The second step is the process of stabilization of the defect as seen by Fig. 6.4e-f. The dynamical inter-chain bond formation is clearly seen in Fig. 6.4b. To our knowledge, this is the first direct simulation to confirm this dynamical inter-chain bond observed in experiment [8]. The dynamical bond formation during the early stage of the photo excitation is contrary to *a priori* intuition. Conventionally, breaking the bond in the chain is expected. Here, we want to explore what physical mechanism makes the dynamical inter-chain bond formed by analyzing the *ab inito* MD simulation.

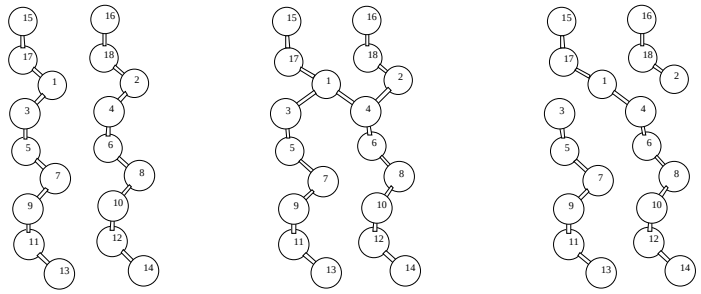

(a) 0 fs (b) 150 fs (c) 154.5 fs

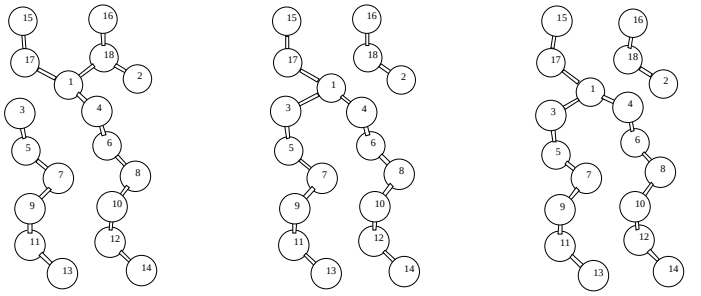

(d) 180 fs (e) 225 fs (f) 1500 fs

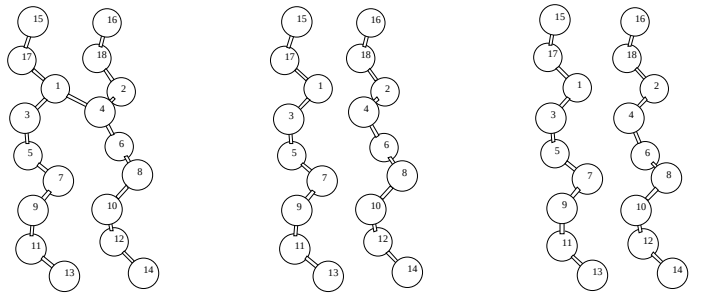

(g) 1845 fs (h) 1860 fs (i) 3000 fs

Figure 6.4: The simulation of photo structural change of parallel Se chain. We maintain light excitation before 1500 fs, after 1500 fs, we relax the light excited conformation to optimal structure

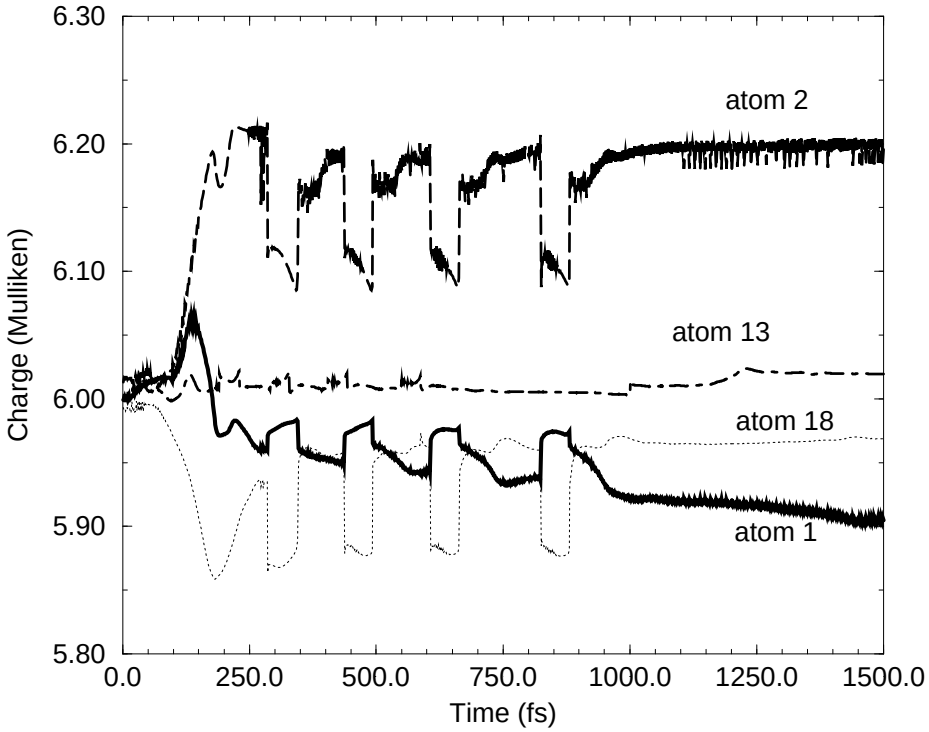

Figure 6.5: Time evolution of Mulliken charge for the active atoms during the photo-excitation. (Parallel chain case). Atom 13 has charge near 6.0 and is shown as a reference atom which was inactive during the simulation. Charges larger than 6 are electron rich, smaller are deficient.

The chemistry behind this process can be understood by looking at the charge evolution of the relevant atoms during the photo-excitation. The charges of the atoms are calculated by the standard Mulliken population analysis [92]. The time evolution of the Mulliken charge of relevant atoms during the photo-excitation is shown in Fig. 6.4. Initially, all the atoms in this two-chain configuration are equivalent. The net effect of random thermal fluctuation and the photo-excitation process, is to move the electrons at atom 18 and 17 to atoms 1 and 2. This process can be

seen from Fig. 6.4 at the beginning of the simulation (from 0 fs to 150 fs), where the charge of atom 1 and 2 increase (more negative [electron rich]) and the charge of atom 18 decrease (more positive [electron deficient]). However, with atoms 1 and 2 becoming more negatively charged, atom 18 becomes more positively charged, and the Coulomb interaction between atoms 18 and 1 will attract atom 1 to atom 18. After atom 1 moves close to atom 18, atom 1 is not geometrically equivalent to atom 2. *As atom 1 becomes a three-fold coordinated site due to Coulomb interaction, the role of atom 1 changes after the transfer. As shown in Fig. 6.4, the charge of atom 2 has a transition around 150 fs. The dynamical bond shown in Fig. 6.4b is formed around this time. This means that electron charge will move away from atom 1 during the photo excitation process, after atom 1 makes the transition from two- to three- coordination.* So, we can see that the dynamical bond formation is a intermediate process for defect creation by photo excitation. The origin of this dynamical bond is the positive and negative charge centers formed by the photo excitation. The residual Coulomb interaction during the photo-excitation causes atom 1 become three-fold coordinated.

Fig.6.4b-e shows the reaction $2C_3 \rightarrow C_3^+ + C_1^-$. The two C_3 centers are atom 1 and atom 4 shown in Fig. 1b, and C_3^+ and C_1^- are atom 1 and 2 respectively shown in Fig. 6.4(f). This dynamical process involves relaxation of the photo-created VAP defect under the condition of the photo-excitation. This relaxation process is also

shown in the Fig. 6.4 from time 150 fs- 250 fs. From time 250 fs-800 fs, we can still see some fluctuation of the charge of those relevant atoms. The photo-excited system is rather stable. It is interesting to observe that the VAP defects are somewhat charged even for the photo-excited system. During the time from 250 fs - 1500 fs, the light excitation persists but the system is stable and no new defects are created.

After we "turn off the light", i.e. restore ground state occupation, the structure with light-created VAP defects takes roughly the same amount time (after 350 fs) to relax back to the initial structure as the time (around 300 fs as shown in Fig. 6.4.) spent to create these defects. This can also be observed by tracking the time evolution of the total energy of the system. Since the VAP defect created by light is a local bond rearrangement in this simulation, the structural change is reversible. In the real situation, the bond rearrangement is not necessarily local and the structural change is also not necessarily reversible. We will discuss this in the next section.

The light induced effects for a simplified parallel chain model can give us some intuitive physical insight on the physical mechanism of structural change and LESR in *a*-Se. In this subsection, we further analyze the light induced ESR in a realistic *a*-Se model. We use a defect free 64 atom selenium model to study the possible mechanism for the fast ESR component observed experimentally.

Similar to the simulation scheme for the parallel chain, we "turn on" the light for 1.5 ps (maintain the electronic promotion from HOMO to LUMO) and relax the

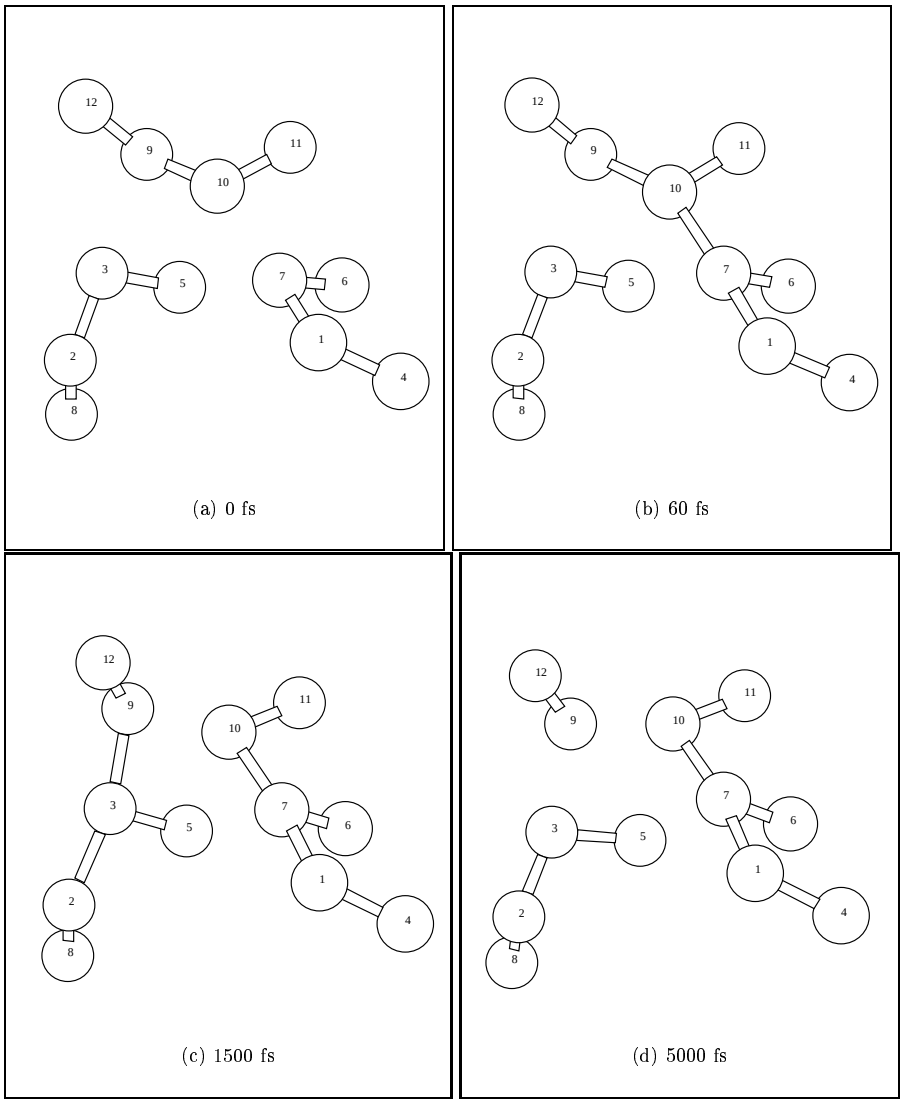

Figure 6.6: The simulation of photo structural change in a defect free *a*-Se model. We do the photo excitation before 1500 fs, after 1500 fs, the structure is relaxed to the optimal structure.

light excited state for 6 ps. Fig. 6.6 shows the whole process. For the *a*-Se model, the dynamical bond formed very quickly (60 fs shown in Fig. 6.6b) . By checking the time evolution of the charge for the atoms, we observe that the extra bond between atom 7 and 10 is formed due to the Coulomb repulsion. The charge transfer due to photo excitation makes atom 1,7,9 and 10 negatively charged. The unbalanced Coulomb interaction between atoms 9 and 10 and between atoms 1 and 7 will propel atom 10 and 7 close each other, making a dynamical 7-10 bond. *Atom 7 prefers to be three-fold coordinated after forming the dynamical bond. Its role in the charge transfer changed. In this time, it gives charge to other atoms rather than taking charge from other sites.* The role change of atom 7 can be seen by time evolution of the charge of atom 7. It initially increases and after 60 fs the charge decreases. The final configuration under the influence of light is equilibrated through forming two charge transfer regions: atoms pair (3,9) and (7,10).

Compared to what happened in the parallel chain, the situation in the *a*-Se is more complex. Although our initial *a*-Se model is defect free, not all atoms are equivalent in term of their charges. Initially, atom 3 is positively charged and atom sites 7,9 and 10 are slightly negatively charged. The very small charge makes the major bond breaking/rearrangement activity happen near these sites. Atom 3 is a two-fold coordinated site but it behaves like a three coordinate defect due to its positive charge. In amorphous selenium, the light created VAP defects are locally

optimized sites. So, even after we turn off the light, those VAP defects still have a chance to survive. The VAP defect in the final structure reflects the fast ESR signal observed in the experiment for the second laser irradiation samples. We also carefully anneal our final structure of a-Se model at higher temperature, we found a carefully annealing scheme can anneal the light created defect away. As a matter of fact, one novel annealing scheme is the "photo annealing" scheme which was presented in our previous work[29].

We presented two simulations to model the LESR recently observed in the experiment: photo-structural change in an infinite parallel chain and photo-structural change in a 64 atom a-Se model. For the parallel chain model, the ESR center is a VAP defect. However, the ESR centers for the a-Se model are two C_3 centers. These centers have all been observed in the experiment. The important observation in our simulation is: the residual Coulomb interaction (attraction or repulsion depending on the environment of those atoms) between the atom sites affected by the light excitation cause the dynamical bond formation; the light created defects are charged defects which is only ESR active under the light excitation; the role of the defect center in the charge transfer will change according to its bonding; the light created defect center will have some possibility to remain in the annealed sample causing the fast ESR signal.

6.4.1 Light Induced Electron Spin Resonance

The most direct way to study the light induced electron spin resonance (LESR) is to calculate the spin polarization. Due to the difficulty to achieve the self-consistency and huge amount of CPU time for SIESTA to accurately reproduce the properties of selenium, we adopt a simple approach to study the LESR for selenium. We still use Fireball to generate the trajectory of the configuration for selenium parallel chain, and then we use the SIESTA to calculate the spin polarization every 10 configurations. Fig. 6.7 shows the time evolution of the spin polarization of relevant atoms of selenium parallel chain. For comparison, we also plot the Mulliken charge calculated by SIESTA. It is quite clear that those light excited defects carry net spin. It also should be noted that although there is only a VAP defect geometrically generated by the light illumination, the three-fold coordinated site is more appropriate to be explained as a one-fold coordinated defect (atom 17) in terms of its charge. Although the absolute charge calculated by SIESTA is not the same as that calculated by Fireball, they show the similar trend suggesting that our understanding of dynamical bond formation by weak Coulomb interaction is correct.

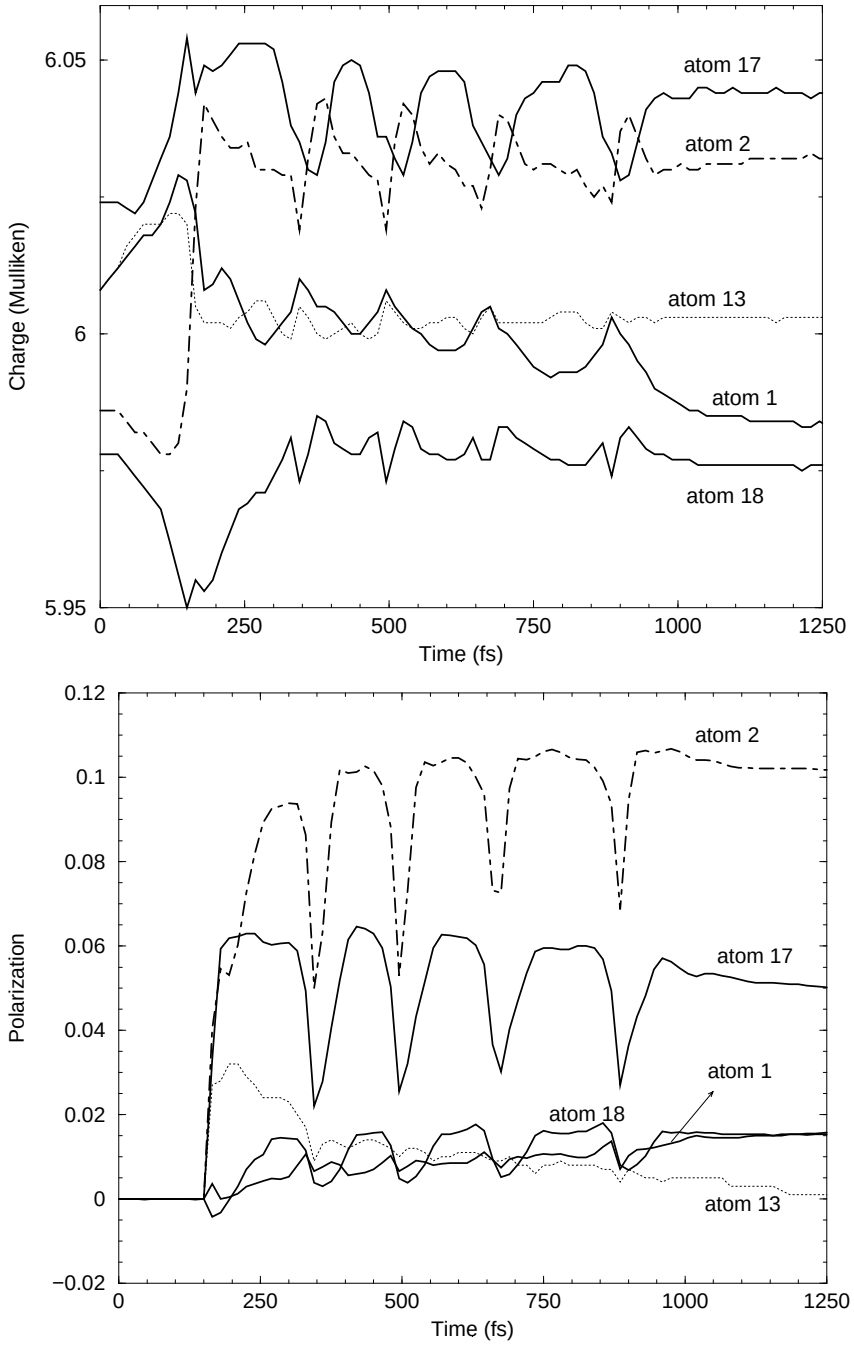

Figure 6.7: Time evolution of the spin-polarization and Mulliken charge for selenium parallel chain during the light illumination.

Chapter 7

Structural and electronic properties of glassy $GeSe_2$ surfaces

7.1 Introduction

Amorphous Ge-Se semiconductors have potential applications for optical storage devices, solar cells, and other devices that require materials which are photosensitive. [107] As a classic glass former, g-$GeSe_2$ has been intensely studied[108, 14,

88, 109, 110]. The material has been thoroughly reviewed by Boolchand[111], and applications of this and related glasses are discussed by Ovshinsky[112].

One of the principal remaining puzzles for bulk $GeSe_2$ glass is the nature of the celebrated "first sharp diffraction peak" (FSDP), which is often interpreted as arising from *some* type of ordering on an intermediate range ($\sim 6 - 10\mathring{A}$) scale. In experiments on liquid $GeSe_2$ [113] and glassy $GeSe_2$ [110], it was demonstrated that a FSDP also occurred in the Bhatia-Thornton [115] concentration-concentration partial structure factor S_{CC}. However, some molecular dynamics simulations [14, 109] did not yield concentration fluctuations in liquid $GeSe_2$. Massobrio *et al*[109] have argued that gradient corrections "GGA's" to the local density approximation of density functional theory are required to get a FSDP even in the total structure factor. More recently, these authors suggested that a simple effect of increased ionicity (a byproduct of the using a larger number of plane waves) was required to obtain a weak FSDP in S_{CC} for l-$GeSe_2$ using plane wave methods[117]. We explicitly demonstrate here by direct comparison to new experiments[110] that the FSDP *and other experimental attributes of g-$GeSe_2$* are well reproduced by a 216 atom model[88], computed with Harris functional LDA as described below.

Little is known about the structural and electronic properties of g-$GeSe_2$ surfaces. We propose atomistic models of these surfaces which are interesting both in their own right, and also, to our knowledge, as the first *ab initio* model of the surface of

a glass. The nature of the "surface reconstruction" for a binary glass is elucidated for the first time and found to largely proceed by ring formation. Atomic force microscopy (AFM) has some potential to attack the unresolved questions about the atomic surface structure of amorphous insulators, although currently not with atomic-level resolution. We will show here that there are clear manifestations of the bulk structure, including even a FSDP, from the first few surface layers.

The rest of this paper is organized as follows: In Section II we discuss the computational methodology of the study, in Section III we discuss the models obtained and compare to experiment, in Section IV and V the electronic properties of the surfaces are discussed with some emphasis on the metal-insulator (Anderson) transition, and the interplay between bulk and surface localized electron states.

7.2 Preliminary theoretical considerations

Structural calculations for the surface model have been performed with a local orbital first principles quantum molecular dynamics (QMD) method designed for application to large complex systems[83]. The method employs density functional theory within the local density approximation and hard norm-conserving pseudopotentials. The method is entirely real space (except for a simple Ewald summation). A short-range non-orthogonal single-ζ local orbital basis of compact, slighty excited

"Fireball" orbitals of Sankey and Niklweski offers an accurate description of the chemistry with a significant computational advantage [84], ideal for this complex material. Applications of the technique to several materials problems are reviewed in Ref. [118, 106].

Using this method, Cobb, Drabold and Cappelletti[88] constructed a 216-atom bulk g-$GeSe_2$ model which correctly reproduced the first sharp diffraction peak (FSDP) around 0.91 $\mathring{A}$, the total structure factor, vibrational density of states, dynamical structure factor and electronic density state were in good agreement with experimental data. This work also revealed that defective threefold Ge atoms were correlated with onefold Se atoms at a distance of about 3.2 $\mathring{A}$ suggesting that the threefold Ge atoms are mostly defective $Ge(Se_{1/2})_4$ tetrahedra. This weaker correlation between defective Ge and Se correlation was recently confirmed by the experiment[110]. Satisfactory agreement with several independent measurements recommends the bulk model and Hamiltonian as suitable for studies of the surface.

To construct a model of the surface we initially break the periodicity along the z direction to transform the periodically extended cube into an infinite slab with two free surfaces (one labeled as the "top" and the other as the "bottom"). Then the slab is relaxed with our molecular dynamics code to search for the the new minimal energy configuration with the slab geometry.

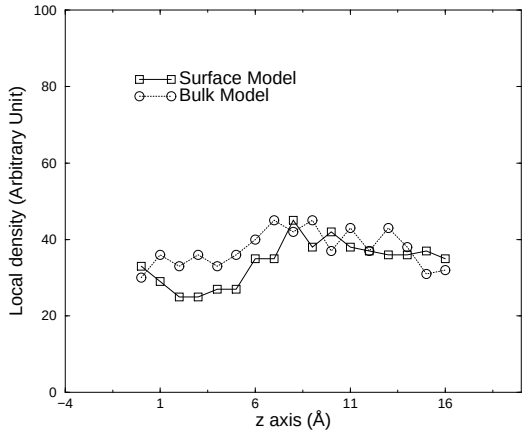

Figure 7.1: Local density (averaged over at a 3 $\mathring{A}$ thickness) at different depths of bulk and surface models of g-$GeSe_2$

After the periodic boundary condition along the z axis is broken, dangling bonds will appear on the surface. Structural relaxation will lead to some major local bonding rearrangements near the surfaces. The total energy of our slab model is about 0.15 eV/atom lower than the unreconstructed g-$GeSe_2$ model. Initially at the bulk density, our slab models expand slightly along the normal direction of the surface during the relaxation. In Fig. 7.1, we show the local density (averaged in the neighborhood of 3 $\mathring{A}$) at different depths of the bulk model and surface model. Our slab model is nearly as homogeneous as the bulk phase with only a small local density fluctuation.

7.3 Structure from Quantum Molecular Dynamics

In this section, we present a rather detailed comparison of our earlier bulk model[88] to very recent experiments, and discuss the structure of the slab models obtained from the preceding section. The structure of these models is analyzed through the partial structure factors. The detailed description of the structural factors used in this chapter is presented in chapter 3.

Figure 7.2 shows the calculated Faber-Ziman partial structure factor for our bulk and slab models. The calculated results show pleasing agreement with (bulk) experiment for both bulk model and surface model. The first sharp diffraction peak at Q=1.00 $\mathring{A}^{-1}$ arises predominantly from the Ge-Ge correlations.

In Fig.7.3, the calculated Bhatia-Thornton structure factors are compared with experimental data. The number-number structure factor S_{NN} resembles the total structure factor since the scattering lengths of Se and Ge are very close. So, our bulk model and surface model describe the experimental total structure factor rather well. Most molecular dynamic investigations failed to reproduce the concentration concentration partial structure factor S_{CC} [109, 14] (in liquid $GeSe_2$). In our bulk and surface model, we clearly observe the FSDP feature in S_{CC}. We note that the

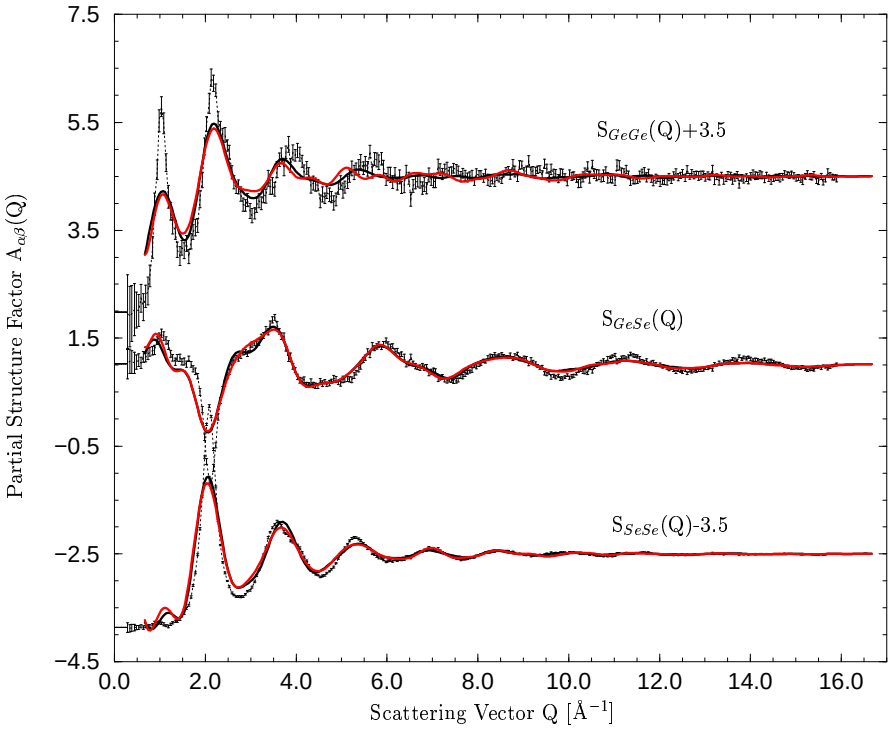

Figure 7.2: The calculated partial structure factors, $A_{\alpha\beta}(Q)$ for g-$GeSe_2$ compared to experimental data from ref.[6]. The dark line and gray line are calculated data for bulk model and slab model respectively.

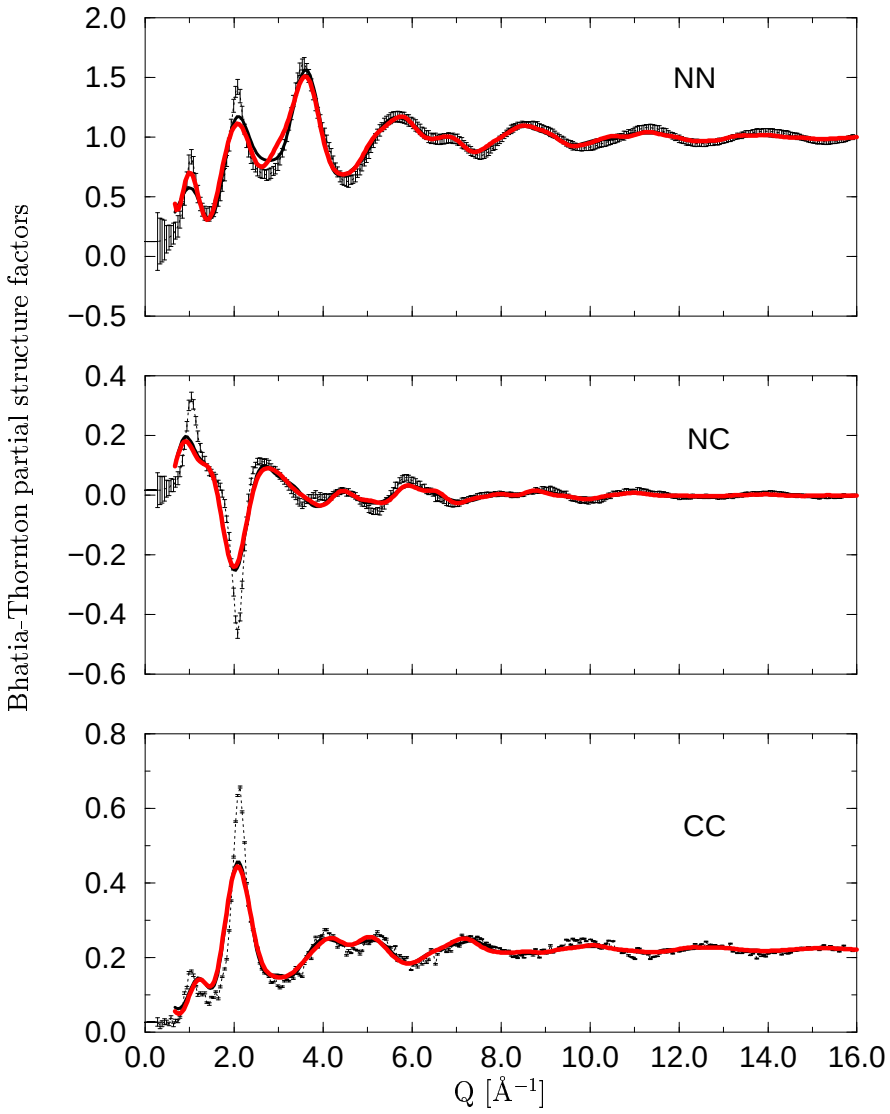

Figure 7.3: The Bhatia-Thornton partial structure factors, for g-$GeSe_2$ compared to experimental data from ref.[6] The dark line and gray line are calculated data for bulk model and slab model respectively.

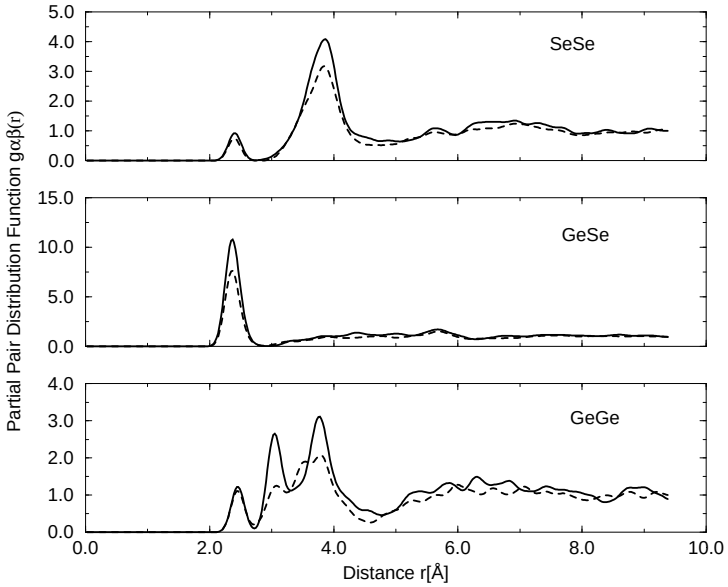

Figure 7.4: The partial pair correlation functions for bulk g-$GeSe_2$ and slab g-$GeSe_2$ model. The dashed line and solid line are calculated data for bulk model and slab model respectively.

intensity of the FSDP in the slab model is somewhat weaker and slightly shifted, probably due to finite-size artifacts.[119].

Some characteristics of surface reconstruction can be seen from the partial pair correlation function for both surface model and bulk model. Similar to the bulk phase, the Ge-Se bond length of $2.37\mathring{A}$ is quite close to the crystal Ge-Se bond length of $2.355\mathring{A}$. There are still Ge-Ge and Se-Se bonds. A significant feature of the slab model is the strong enhancement at 3.05 $\mathring{A}$ in the Ge-Ge correlation function. The 3.05 $\mathring{A}$ peak in g_{Ge-Ge} is due to correlation between edge sharing tetrahedra. The increase of the strength of this peak in the slab model indicates

that the surface atoms of the g-$GeSe_2$ are reconstructed in part through forming the edge-sharing tetrahedra. The fraction of the edge sharing atom Ge atoms in the bulk model is 47% which is close to experimental values 40% [120] and 35(5)% [110]. However, this increases to 69% in the slab surface model. Vashishta et al. [13] found that there was significant improvement in the FSDP as the fraction of edge-sharing tetrahedra increased. Our previous study [88] also indicated that FSDP had a strong dependence on the fraction of edge-sharing tetrahedra.

The surface reconstruction of the g-$GeSe_2$ model can be seen more clearly from the microstructure of the surface layers. To focus on the surface character of our slab model, we choose the 50 atoms closest to vacuum above (or below) as the top (or bottom) surface. Fig. 7.5 shows the surface structure of our slab model. There is a clear tendency for ring formation in both surfaces. Earlier, Dong and Drabold[121] studied the surface reconstruction of ta-C. They found that planar ring or chain formation was the dominant surface reconstruction mechanism. It is quite interesting that for a binary amorphous material like g-$GeSe_2$, the atoms at the surface still reconstruct through ring formation. The enhancement of ring formation can be seen explicitly through the ring statistics.

ring size	3	4	5	6	7	8	9	10	11
bulk	3	20	10	23	3	12	7	9	20
surface	5	27	10	25	6	20	9	27	26

Table 7.1: Ring statistics: the number of n-order rings, n=3 through 11 for bulk and surface $GeSe_2$ model.

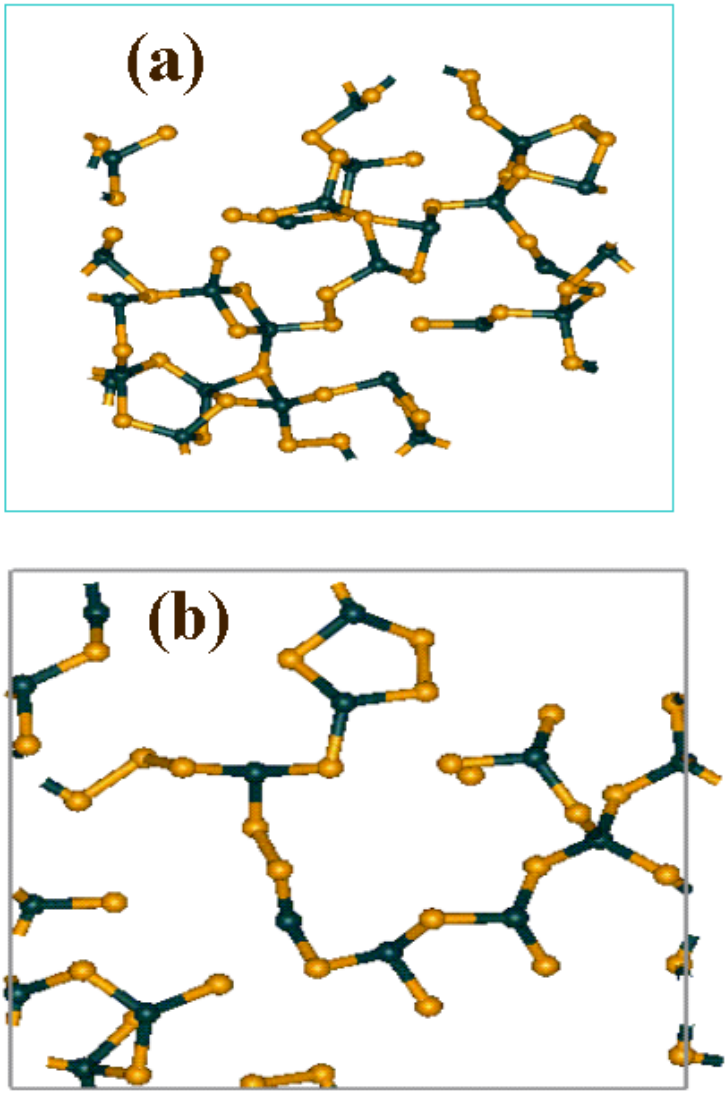

Figure 7.5: The microscopic structure of the surface(a) and bulk region(b) for the slab model. The dark color represents the Ge atoms and grey color represents Se atoms. The periodic boundary conditions are imposed in the plane of the figures. The ring formation can be seen in surface region (a).

From Table 7.1, we can see that the number of 4-, 8-, and 10-member rings exhibit a major increase indicating more edge-sharing tetrahedra are formed during the surface reconstruction. These mechanisms can be intuitively understood by the fact that a ring is a relatively planar structure and it is a very reasonable structure to enable the atoms maintain their preferred coordination at surface plane.

		No. of atoms		
atoms	Coordination	Surface only	Whole slab	Bulk
Se	1	12(12%)	18(8%)	15(7%)
	2	36(36%)	92(43%)	101(47%)
	3	20(20%)	33(15%)	28(14%)
Ge	3	10(10%)	13(6%)	13(6%)
	4	22(22%)	59(27%)	58(27%)

Table 7.2: Coordination number distribution in the slab model and bulk model. The number in the parenthesis denotes the percentage of the atoms in this configuration. For the bulk model, there is a five-fold coordinated Ge atom which is not listed in the table.

The statistics of the number of atoms of each type of coordination for the slab model and bulk model is listed in table. 7.2. An interesting feature is that the fraction of three and four-fold coordinated Ge atoms is similar in the bulk and surface model. However, undercoordinated Ge atoms segregate in the surface layer. This suggests that some undercoordinated Ge atoms in the bulk region become ideally (4) coordinated Ge atoms during surface reconstruction. This result shows that the "sp^2" concentration will be higher in the surface region. Experimental result on the *ta*-C surface confirmed much more sp^2 contents on surface region[122].

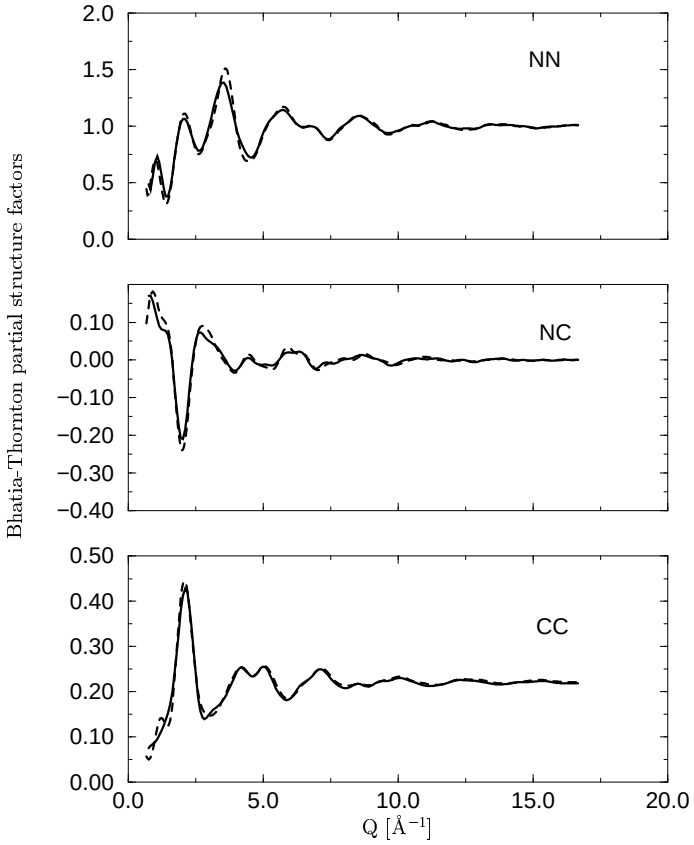

Figure 7.6: The surface projected Bhatia-Thornton partial structure factors for the slab model. The dashed line and solid line are the Bhatia-Thornton partial structure factors for whole slab and surface region respectively. The surface region was defined as the 70 atoms closest to vacuum for bottom surface of slab model.

The first sharp diffraction peak (FSDP) observed in g-$GeSe_2$ is often interpreted as a consequence of an ordering on an appropriate intermediate length scale. However, which intermediate order structure govern the FSDP has not been certainly determined. The difficulty in determining the microscopic origin of the FDSP originates from the fact that no experiment can measure the structure in sufficient detail. Fig. 7.6 shows the surface projected Bhatia-Thornton partial structure factors. This surface was formed by choosing 70 atoms closest to vacuum. The thickness of this surface is about 6.5 $\mathring{A}$. The S_{NN} structure factor of this surface region almost reproduces S_{NN} of the whole slab model, and the FSDP in S_{CC} was not seen from this slab. Thus, to a significant degree, the 70 surface atoms carry the overall structural information of the entire $GeSe_2$ model. This result hints that it may be possible to experimentally determine the origin of the FSDP by studying the microscopic structure information of the surface atoms. We hope future AFM experiments can confirm this conjecture.

7.4 Electronic Properties

The electronic properties of our slab model are analyzed through the electronic density of states and inverse participation ratio. A point of interest in this section is the nature of localized "surface states" for an amorphous material. Their formation

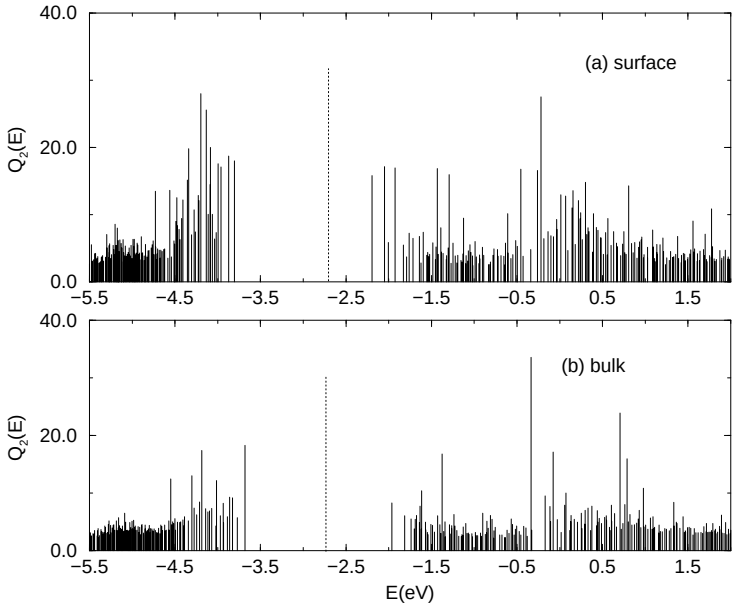

Figure 7.7: Inverse participation ratio in the band gap region for the slab model and bulk model. The vertical dotted indicates the position of Fermi Level.

of "surface bands" and resonant mixing with bulk defects are interesting features of this study.

For both the slab and bulk model, we did not see an obvious change of electronic density of states. Although there are more defects in the slab model compared to the bulk model, the Γ-point bandgap in the slab model is 1.61 eV which is only slightly smaller than the gap 1.72 eV in the bulk model. There are still no states in the fundamental band gap despite the overall increase in defects for the slab. To connect localized eigenstates to particular topological/chemical irregularities, we

compute the inverse participation ratio:

$$Q_2(E) = N \sum_{n=1}^{N} q(n, E)^2. \tag{7.1}$$

where N is the number of atoms in the slab model and q(n,E) is the Mulliken charge [92] localized on atom site n in a certain eigenstate E. Larger $Q_2(E)$ means that the eigenstate is more localized in real space, and the individual contributions to the sum indicate which sites are most responsible for the localization. Fig. 7.7 shows the individual electronic eigenstates near the band gap for both slab model and bulk model. In the slab model, there are more localized states near the valence band and conduction band edges.

By examining the localized states at the band edges, we found that the localized states at the valence band edge derive mostly from undercoordinated Ge atoms and one-fold coordinated Se atoms. The localized states at the conduction band edge are mostly due to three-fold coordinated Se atoms. The defect states in the slab model reveal that the valence alternation pair model, which explains most electronic properties of elemental amorphous Se, [7, 29, 28] still plays the important role in this binary chalcogenide glasses. But in the g-$GeSe_2$ model, the undercoordinated Ge atoms and one-fold coordinated Se atoms together served as the C^- center and the three-fold coordinated Se atoms plays the role of C^+ center. Compared to bulk model, many localized states in the slab model exhibit surface character. Table. 7.3

lists the localization and defect type for the atoms at the conduction band edge and valence band edge.

	Valence Band Edge				Conduction Band Edge			
Reg.	atom	E(eV)	q(n,E)	Coord.	atom	E	q(n,E)	Coord
1	3(Se)	-4.73	7.3	1	9(Ge)	-0.46	6.80	4
	18(Se)	-4.42	5.74	1	10(Ge)	0.24	7.40	3
	21(Se)	-3.96	6.31	1	23(Se)	-0.21	19.03	3
	25(Ge)	-3.99	6.72	3	25(Ge)	0.23	6.15	3
	185(Se)	-4.77	7.17	2	29(Ge)	0.16	6.11	3
	198(Ge)	-4.20	12.83	3	31(Se)	-1.43	8.30	3
	210(Se)	-4.08	6.06	2	34(Se)	-1.43	7.29	3
	211(Ge)	-4.08	6.11	3	47(Se)	-1.93	6.50	3
	213(Ge)	-4.13	8.52	3	193(Ge)	-0.26	8.54	3
	215(Se)	-4.13	10.61	1				
2	69(Ge)	-3.87	8.67	3	69(Ge)	0.80	9.48	3
	76(Se)	-4.56	7.67	1	63(Se)	-1.93	5.61	2
	112(Ge)	-3.80	8.33	4				
	133(Se)	-4.33	13.65	2				
	164(Se)	-4.35	7.76	2				

Table 7.3: The coordination and localization of atoms causing the localization at the conduction band edge and valence band edge. Reg.1 indicates the top and bottom surface region and Reg.2 indicates the bulk region.

From Table 7.3, we can see that the localization of electronic states near the band edge derives mostly from surface atoms. Some strained, ideally coordinated atoms and defective atoms make a contribution to the localization of electronic states. If we take a close look at the atoms which contribute to localization, we observed that most of these are connected with some defect sites. For example, a Se atom (number 185) with strong localization is very close to the undercoordinated Ge atom (number 211). Ge (number 9) contributes to the localization at the conduction band edge and is a neighbor of three-fold coordinated Se (number 34) atom. Thus, we infer that

the undercoordinated Ge and Se atoms lead to the localized states at the valence band edge and overcoordinated Se atoms cause the localization at the conduction band edge. This seems to confirm the valence alternation model by Kastner et al. [7].

For a tetrahedral amorphous carbon surface and a 4096-atom a-Si[123], Dong and Drabold found that the spatial character of the eigenstates from the Fermi level into the interior of the valence states goes through a Anderson (localized-to-extended) transition. We find a qualitatively similar transition in this binary glass.

To examine the atomistic spatial structure of an electronic eigenstate, we use the same visualization scheme as Dong and Drabold[123]. The basic procedure is as follows. For a given electronic eigenstate, we compute the electron charge associated with each atom. Each atom is drawn in one of the four levels of the gray scale according to the amount of charge associated with it. Black atoms depict strong localization centers that contribute more than 10% of total charge each, less dark atoms are sites that contribute more than 2.5%, light atoms are sites that contribute more than 1% each, and white atoms contribute rest. For clarity, 99% of the total charge is present and those atoms that contribute the remaining 1% charge for the given eigenstates are omitted in the figure.

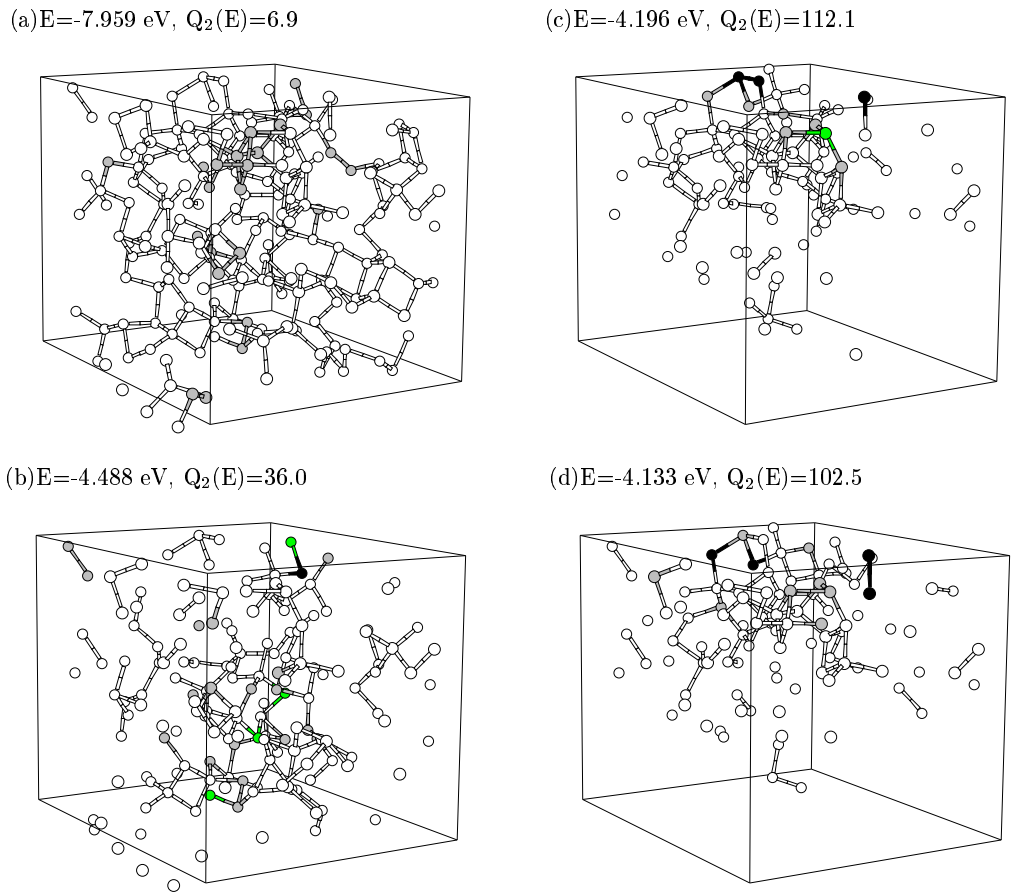

Figure 7.8: Spatial character of the bulk-to-surface transition of valence electronic states in the surface slab model. The electronic states evolve from (a) a bulklike extended states in the middle of the valence band to (b) a less extended state, to (c) a more surfacelike state, to (d) a surface like localized state. The color is coded according to the fraction of total charge: black ($\geq$ 10%), less dark ($\geq$ 2.5%),light ($\geq$ 1%) and white ($\leq$ 1%). 99% of the total charge is shown.

We can see from Fig. 7.8 that the extended-to-localized transition (for energies ranging from midband to midgap) of electronic eigenstates proceeds from the "bulk-to-surface" transition on the g-$GeSe_2$ surface. In our slab model, the states from inside the valence band are bulk-like extended states. In this region (Fig.7.8a), we did not observe any significant charge localization caused by surface atoms. When we approach an energy near -4.5 eV, the surface localized defect begins to be manifested in the charge localization(Fig.7.8(b)). However, the states are still quite extended. When the energy approach -4.2 eV (Fig.7.8(c)), the influence from surface atoms become dominant. Fig.7.8(d) shows a strong localized surface states and most charges are localized at the surface region.

7.5 Defects and Charge Localization

For both slab model and bulk model, there are many defect sites. However, we did not observe any states in the fundamental band gap. Our model also correctly reproduces the FSDP in the structure factor with a fairly large number of defect sites. It is important to know how the defect sites manifest themselves in the electronic eigenstates. Fig. 7.9 shows the inverse participation ratio for the whole energy range and typical defect structure causing the localization of the eigenstates. The localized states at -18.4 eV, -8.8 eV and -13.7 eV are due to overcoordinated Se influenced by an undercoordinated Ge atom (defect type (a) in the right panel

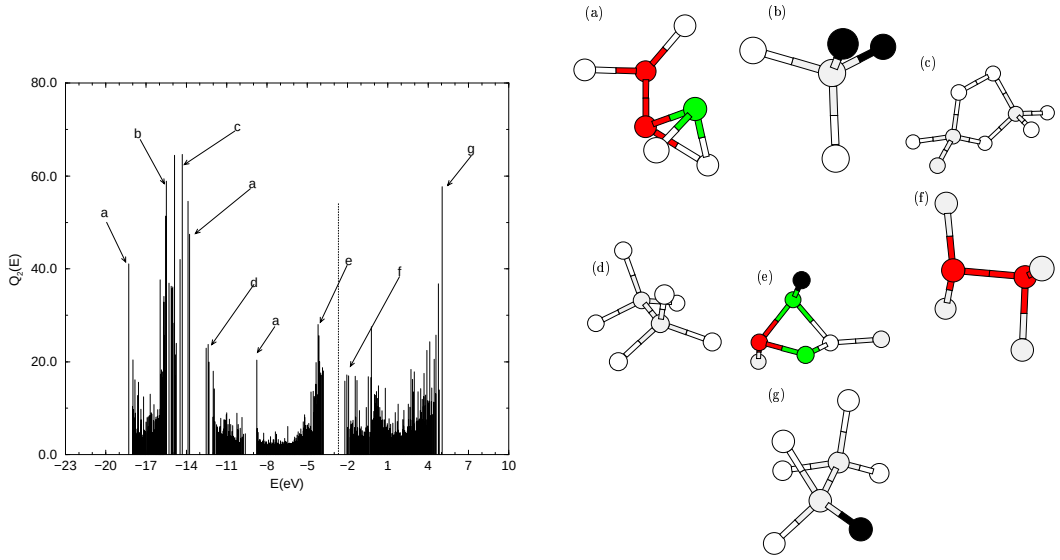

Figure 7.9: The characteristic defect types causing the localization state in the electronic eigenstates in the slab model. The defects are visualized as: onefold Se atoms (black), three fold Se atoms (less dark), threefold Ge atoms (grey), fourfold Ge atoms (light grey), twofold Se atoms (white). The vertical dotted line indicates the position of Fermi level.

of fig. 7.9.). The localized states around -15.7 eV to -14.7 eV are mainly due to undercoordinated Se atoms (defect type (b)), Se-Se wrong bonds (defect type (c)) and overcoordinated Se atoms (defect type (a)). The state at -12.43 eV is caused by Ge-Ge wrong bonds (defect type (d)). The localization at the top of valence band is caused by a ring structure consisting of two undercoordinated Ge atoms, one onefold Se atoms and one threefold Se atoms (defect type (e)). We notice that this state is not as localized as defect type (a), (b), (c), (g). The localization at the bottom of the conduction band is caused by the overcoordinated Se atoms (defect type (f)). The state at 5.02 eV derives from a Ge-Ge wrong bond influenced by onefold Se atoms. The most defective structures do not cause localized states in the fundamental band gap but make some localized states far inside the valence band and conduction band. At the band edge, the defect-defect interaction makes the electronic eigenstates less localized. This kind of delocalization is explained by Dong and Drabold's resonant cluster proliferation model. The delocalization is via the clusters with similar electronic energies. The defect type (e) and (f) in our slab $GeSe_2$ model confirmed this resonant tunneling mechanism. This is the reason why defect type (c) only with a Se-Se wrong bond causes much more localized states than the geometrically more defective structure (e) and (f) do.

7.6 Conclusion

We have reported a structural model of g-$GeSe_2$ surfaces constructed with first principles molecular dynamics simulation. The full partial structure factors are compared with experimental data. Especially, the feature of FSDP in Bhatia-Thornton concentration-concentration partial structure factor S_{CC} is first observed in a first principle theoretical study. We also find that the feature of FSDP will be emerged at 6.5 Å thickness of surface closest to vacuum. So, it maybe possible to explore the FSDP structure by AFM or perhaps STM (if the material can be made at least weakly conducting). Compared to bulk g-$GeSe_2$ model, the slab $GeSe_2$ model has more edge sharing tetrahedra. Similar to the case of ta-C, planar rings are formed in the surface of slab model. We also observe that electronic states evolve from bulklike extended states inside the bands to surfacelike localized states in the band tail. The surface localized states can be delocalized through the resonant cluster proliferation mechanism.

Chapter 8

Structural Models of amorphous tertiary glass by *ab-initio* molecular dynamic simulation

8.1 Introduction

The elemental and alloyed chalcogenide glasses have attracted attention for years. These materials exhibit classic generic features of glasses: Urbach (exponential) optical absorption tails, linear specific heat at sufficiently low temperatures, a first sharp diffraction peak, which carries information about intermediate range order, a Bose

peak in the vibrational spectrum and often pronounced sensitivity to light. Certain compositions such as $GeSe_2$ are classic glass formers, and since there are broad glass forming regions for several of the chalcogen alloys it is possible to experimentally "tune" the composition to suit the study at hand[124]. Two recent examples exploiting this continuously variable composition included a study of isocoordination behavior in vibrational spectra (for tertiary GeAsSe glasses with fixed average coordination $\langle$ r $\rangle$; the first vibrational band is strikingly similar up to about 20 meV[125]), and a direct observation of the floppy to rigid transition in Ge_XSe_{1-X} behavior in complex (and topologically/chemically very distinct) systems[125]. There are experimental indications that chemical order is broken in chalcogenide glasses [126, 110]. Taylor's group also reported the dependence of the number of wrong (As-As) bonds on the fiber draw rate from Nuclear Quadruple Resonance (NQR) on the spin 3/2 nucleus ^{75}As (faster draw rate, more As-As bonds[126]). Very recently, Petri et al. [110] reported the wrong bond formation in g-$GeSe_2$ by careful study of the partial pair correlation function of this material[110]. To make a further advance, there is a need for realistic atomistic models of these glasses.

For complicated glasses such as tertiary alloys, it sometimes happens that standard MD "cook and quench" methods are unable to obtain the correct structure. Our earlier work on GeAsSe glasses shows that with no *a priori* information of a random network with the correct numbers of atoms, rather unrealistic models are

obtained (a clear signature of this is a large number of unphysical gap states). There are methods now being developed to overcome the sampling limitations of MD, especially the Activation Relaxation Technique "ART", pioneered by N. Mousseau and G. Barkema [20] and already applied with considerable success to *a*-Si, *v*-SiO_2 , and other systems.

Since there is good reason to believe that the chemical order of the glassy phases of these materials *g*-$GeSe_2$[88] and *g*-As_2Se_3[127] are much like the crystal and liquid, it is likely that realistic models of *g*-$GeSe_2$ and *g*-As_2Se_3 will be constructed after a long equilibrium of the liquid and a slow cooling since the local chemical order is present from the beginning. However, it is of great interest to develop a method which will successfully handle systems for which little is known *a priori* about the chemical and topological order, as for example in most of the tertiary chalcogenides . We have tried "brute force" methods of attempting to equilibrate a liquid of the right composition and cooling it and have usually been disappointed in the results. One reason for this problem is overly short MD simulations (a problem greatly exacerbated by the choice of any *ab initio* method). The other reason is that the complexity of this kind of optimization problem will exponentially increase with the increase of the size of the system. Especially the latter reason will inhibit any realistic model to be built by brute force calculation even with the best parallel computer in the world.

Here, we describe a systematic method of constructing realistic models of tertiary chalcogenide glasses. The idea is based on the following assumptions: the local short range chemical order does not change dramatically between large system and small system; the chemical order of a small cell of a material can be correctly obtained by long *ab-initio* molecular dynamic simulation. Basically, we first produce a nearly perfect sub-unit cell by arbitrary long MD simulation. Using this sub-unit cell as the "pseudo crystal", we build the large cell. Then we melt this large cell at liquid temperature to eliminate the artifact between the sub-unit cells. Then we slowly cool this large cell to the room temperature and quench this cell to 0K. The detailed description of the procedure will be described in next section. By applying this method, we generate two tertiary chalcogenide glasses, $Ge_{0.2}As_{0.4}Se_{0.4}$ and $AsGe_{0.8}Se_{0.8}$. We compare the static structure factor, pair correlation function and vibrational density of state with available experimental data. It is quite amazing that these cells correctly reproduce experimental data. Especially the feature of the first sharp diffraction peak is correctly reflected in our model. More importantly, the band gap around 0.8 eV for $Ge_{0.2}As_{0.4}Se_{0.4}$ and 0.6 eV for $AsGe_{0.8}Se_{0.8}$ is observed in the electronic density of state. From analysis of the topological structure, we found: the majority of selenium atom are three-fold coordinated and positively charged; the germanium and arsenic defects are negatively charged. The VAP alternation model [7] which explains most unusual properties of chalcogenide glasses is still valid for these tertiary glasses.

8.2 Model

8.2.1 Theory

We use a simplified density functional quantum molecular dynamic (QMD) method Fireball96 [84, 83]. The method uses local density and pseudopotential approximations, is self-consistent and entirely real space (a local orbital basis is employed). For a recent review of the technique the reader is refereed to Ref.[118].

8.2.2 MD procedure

We first randomly put small numbers of atoms according to the correct stoichiometry (for $Ge_{0.2}As_{0.4}Se_{0.4}$ 5 germanium atoms, 10 arsenic atoms and 10 selenium atoms; for $AsGe_{0.8}Se_{0.8}$ 10 arsenic atoms , 8 germanium atoms and 8 selenium atoms) in a small cubic cell. The size of the cubic cells were chosen to make the density of these glasses close to experimental data. The box size of the 25 atom cell of $Ge_{0.2}As_{0.4}Se_{0.4}$ is 8.75 $\mathring{A}$ and this corresponds to density 4.687 g/cm^3. The box size of the 26 atom cell of $AsGe_{0.8}Se_{0.8}$ is 9.00 $\mathring{A}$ and this correspond to density 4.459 g/cm^3. Using these random configurations as the initial cells, the cells were annealed at 5000 k for 1ps, equilibrated at 2000 K for 15 ps, cooled over 1000 K for 15 ps, cooled over 300 K for 15 ps and quenched to 0K. After the final configuration

was obtained, we melted this sample and repeat the "melting and quench" procedure for several cycles until the minimum energy did not change at all. At this stage, we concluded that we had a "best" structure for the small unit cell of these tertiary glasses. Using this sub-unit cell as the "pseudo crystal", we build the larger cubic cell (200 atoms cell for $Ge_{0.2}As_{0.4}Se_{0.4}$ and 208 atoms cell $AsGe_{0.8}Se_{0.8}$.) Then we melt this large cell at 1500 K for 7.5 ps, cool over 300 K for 3 ps and quenched to 0K. All of our calculations were done using only Γ point to sample the Brillouin zone.

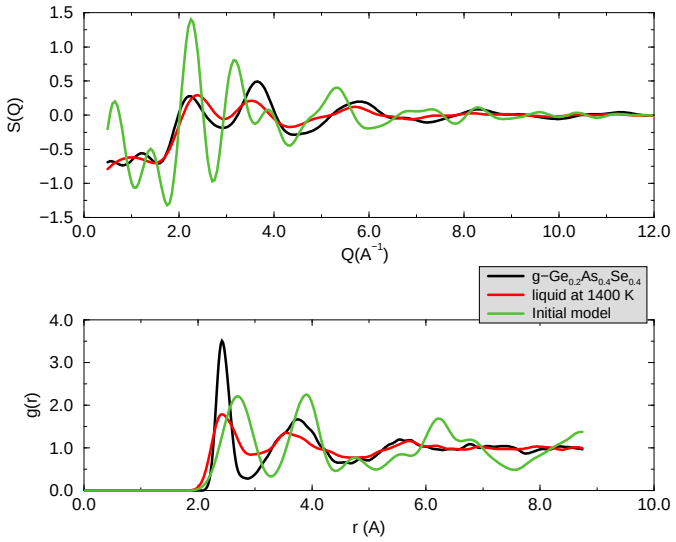

Figure 8.1: The static structure factor and pair correlation function for g-$Ge_{0.2}As_{0.4}Se_{0.4}$ at different stage of simulation.

Figure. 8.1 shows the pair correlation function g(r) of g-$Ge_{0.2}As_{0.4}Se_{0.4}$ for the small unit cell, liquid state for the larger cell at 1400 K and final glass state for larger cell. The peak around 4.4$\mathring{A}$ in the g(r) of sub-unit cell is due to the artifact

between sub-unit cells. This artifact disappeared in the liquid state after we melt the cell at 1400 k for 6 ps. This fact is more evidently shown in the static structure factor at low Q value (less than $2\mathring{A}^{-1}$). The first two peaks in the initial model was due to the correlation between the sub-unit cells and these two peaks were completely melted away. So, we believe that our final glass model does not contain the correlation between the sub-unit cell. It is interesting to see that first sharp diffraction peak emerged at the position of experimental data came out naturally at the liquid temperature.

8.3 Structural Properties

8.3.1 static structure factor

Fig. 8.2 shows the static structure factor and pair correlation function for $Ge_{0.2}As_{0.4}Se_{0.4}$ from our simulation and the comparison with the experiment. The experiment data is from [128]. Our calculation shows quite pleasant agreement with experiment data. Considering that the simulation was done without knowing any *a priori* information of this tertiary glass, the fact that all the peak position and most spectral weight of S(Q) agree with data is quite encouraging. The second, third and fourth peaks are a result of the short range order of the model. These peaks as well as peaks at higher Q depend primarily on the nearest neighbors. The second peak

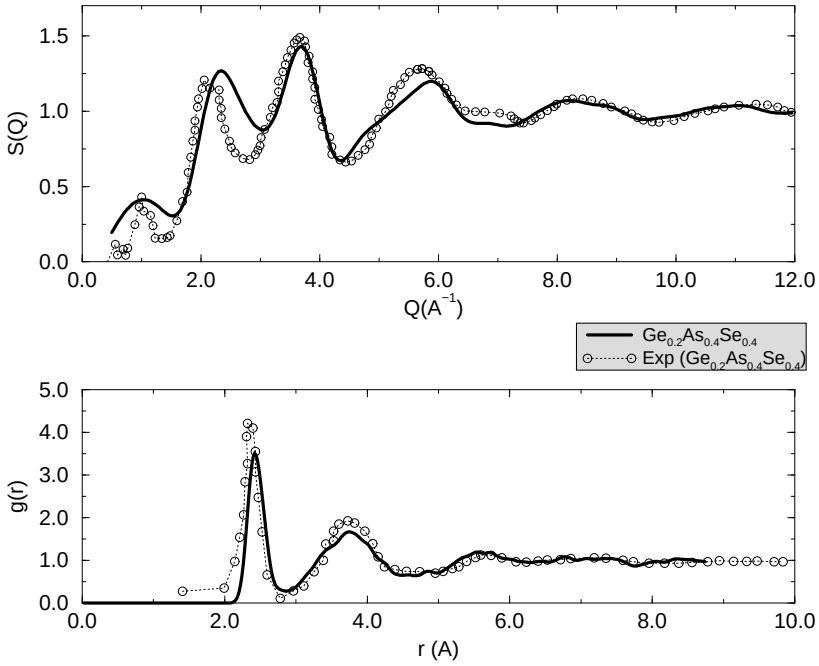

Figure 8.2: Static structure factor and radial distribution function for g-$Ge_{0.2}As_{0.4}Se_{0.4}$. The experimental value is from reference [128]

depends on next nearest neighbors at approximately 3.8$\mathring{A}$. From partial structure factor, we see that the S_{GeGe} (Q) and S_{GeSe} (Q) tends to cancel each other. This feature also appears in the partial structure factor of g-$GeSe_2$ [88]. But for the tertiary glass, the As atom make a strong correlation to both Ge and Se atoms around this distance as seen from the partial structure factor.

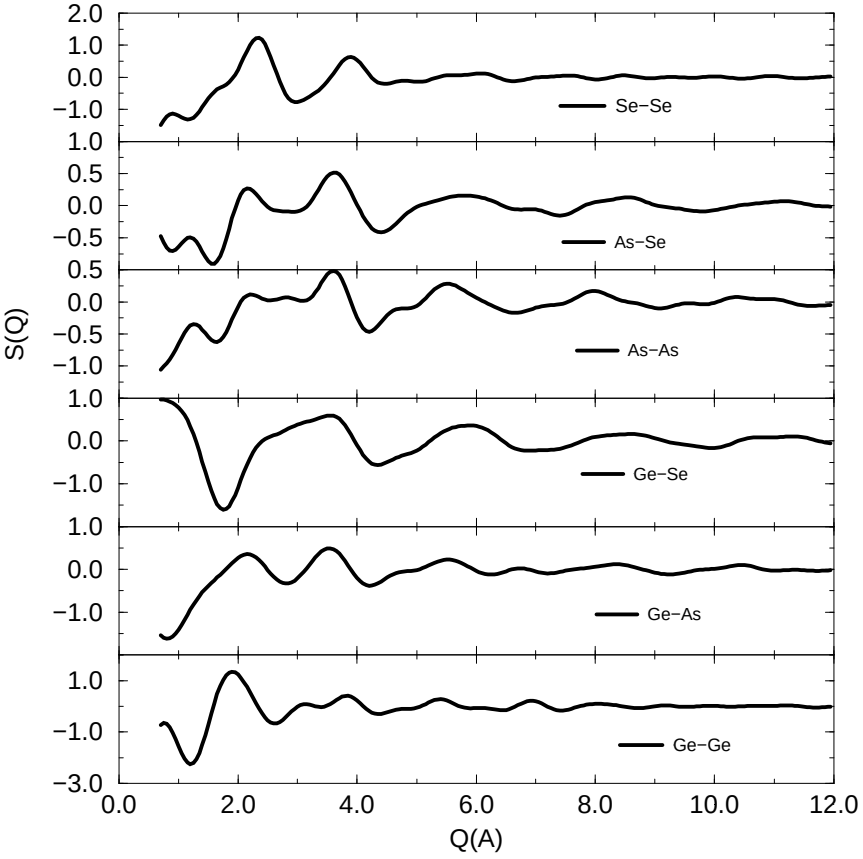

Figure 8.3: Partial structure factor for computer generated g-$Ge_{0.2}As_{0.4}Se_{0.4}$ model.

The position of the first sharp diffraction peak (FSDP) in our model is about 1.0$\mathring{A}$ and is at the position of experimental value. The FSDP is the result of correlations on a length scale of approximately 6.5 $\mathring{A}$ (this length is obtained from the

FSDP's wave vector using $r = 2\pi/|Q|$). From the $S_{\alpha\beta}(Q)$ it is apparent that FSDP has contributions from all of the partial. It is also interesting to see from figure 8.1 that the FSDP peak actually emerged at liquid temperature 1400 K. Earlier calculation on g-$GeSe_2$ also indicated that FSDP is seen at liquid temperatures. This fact indicates that liquid model contains most part of the information of its glass counterpart. There is no dramatic structure change during the liquid to glass transition. This is a reason why it is a good glass former.

There are still slight discrepancies between the experimentally observed strength of the FSDP and second peak and those of our S(Q). Considering the maximum correlation length in our model is $8.75\mathring{A}$ which is not far from the correlation length $6.5\mathring{A}$ of FSDP, the larger model is still needed for give a better description of the experimental data. However, Overall our S(Q) is impressively in agreement with the experimental result.

8.3.2 Pair correlation function

Our total pair distribution function shows good agreement with experiment. From $g_{\alpha\beta}(r)$ the nearest-neighbor and next neared neighbor peaks are easily determined. Table. 8.1 shows the averaged bonding distances (ABD) of different bonds present in the model.

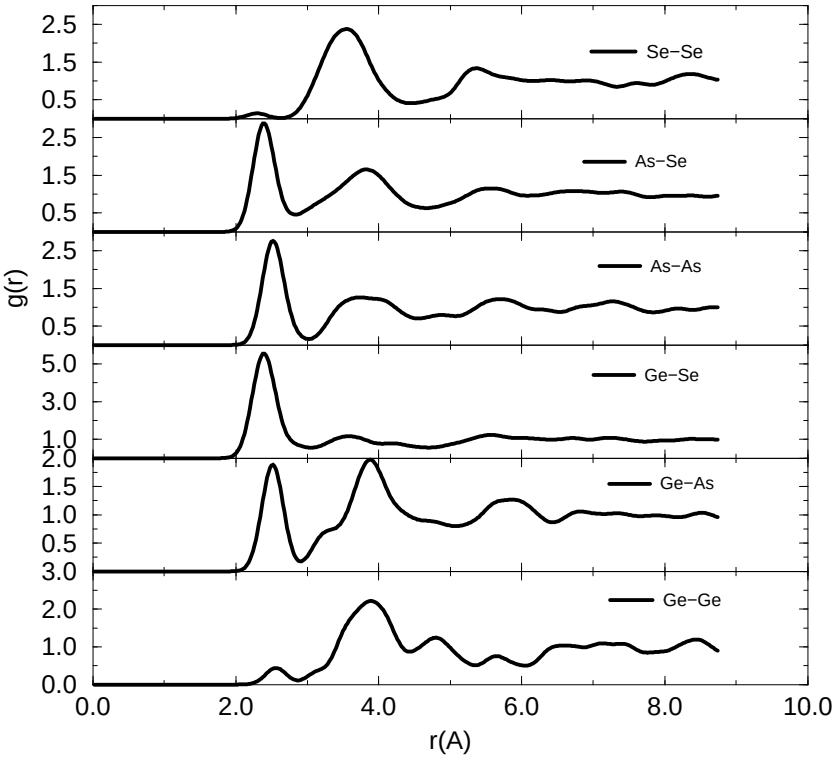

Figure 8.4: Partial pair correlation function for g-$Ge_{0.2}As_{0.4}Se_{0.4}$ model.

Bond type	Distance $\AA$	Nicolas et al. [128] $\AA$	Std. Dist. $\AA$
Ge-Ge	2.56	2.51 ± 0.19	2.54 a-Ge
Ge-As	2.54	2.44 ± 0.14	2.45 c-$GeAs_2$
Ge-Se	2.40	2.48 ± 0.15	2.35 α-$GeSe_2$
As-As	2.52	2.41 ± 0.07	2.52 Rhombohedric As
As-Se	2.40	2.41 ± 0.06	2.41 c-As_2Se_3
Se-Se	2.36	2.40 ± 0.06	2.40 a-Se

Table 8.1: Averaged bonding distances of different bonds in tertiary glassy model $Ge_{0.2}As_{0.4}Se_{0.4}$. St. Dist. is the abbreviation of the standard distance. The standard distance is from reference [128]

All this bonding is consistent with the earlier study by Nicolas et al[128] and with some standard distances in compounds formed by these elements. In the Nicolas model, the As-As ABD is 4% lower than the standard distance in the amorphous As -2.49 $\AA$ (Ref. [129]) - as well as the in the rhombohedric one -2.51 $\AA$ (ref. [130]). Our model is closer to these standard values. It is interesting to notice that the feature of the g_{GeGe}, g_{GeSe} and g_{SeSe} are quite similar to the g-$GeSe_2$ [88]. As readily bonds with both the Ge and Se. This does not support the conjecture of the low probability of Ge-As bond formation by Borisova[124]. The g_{AsX} partial correlation function all have a small peak around 5.7$\AA$. These peaks indicate the existence of intermediate range order within our model.

Table 8.2 collects the resulting coordinations of the atoms. The remarkable feature in this result is that Se atoms tend to be three-fold coordinated while majority defect Ge atoms are also three-fold coordinated. Also, we noticed that As atoms

element	Coordinations			
	5	4	3	2
Ge	2	12	26	0
As	0	2	69	9
Se	0	0	41	39

Table 8.2: Coordination number distribution in computer generated $Ge_{0.2}As_{0.4}Se_{0.4}$ model.

keep it natural coordination. This result is contradictory to most people's hypothesis. In addition, we did not observe the molecular unit in this model.

8.4 Dynamical Properties

The dynamical properties of our model are analyzed through the vibrational density of states (VDOS) and inverse participation ratio. The supercell normal mode eigenvalues and eigenvectors were obtained from the dynamical matrix. The dynamical matrix is determined by displacing each atom by 0.03 $\mathring{A}$ in three orthogonal directions and then performing *ab-initio* force calculations fro all the atoms for each such displacement. Each such calculation yields a column of the force constant matrix.[97] The vibrational eigenvectors and eigenvalues of the supercell are then easily obtained. The VDOS was determined from the vibrational eigenvalues by summing Gaussian centered at each eigenvalue.

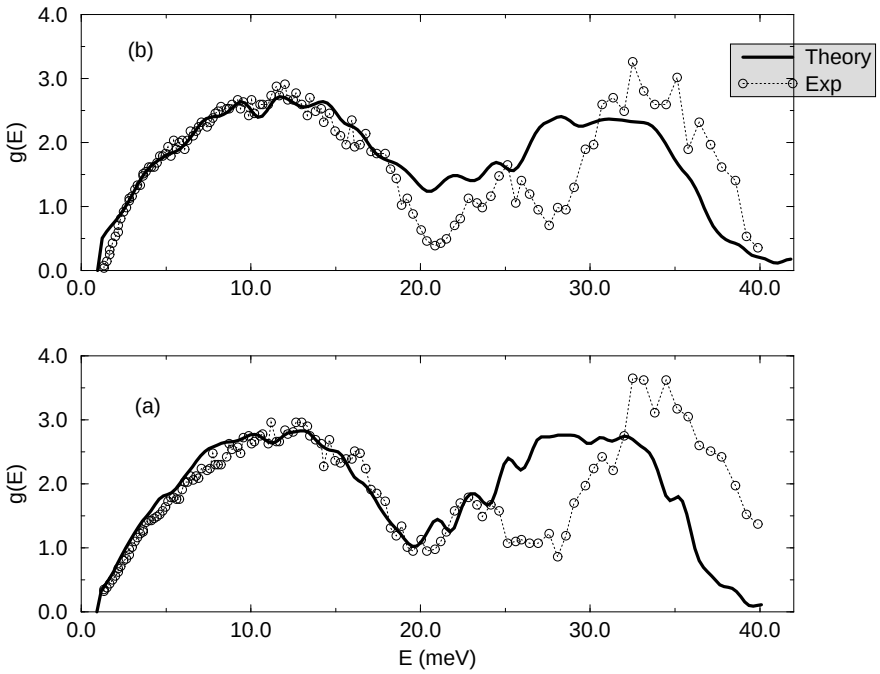

Figure 8.5: Vibrational density of state of g-$Ge_{0.2}As_{0.4}Se_{0.4}$ (a) and $AsGe_{0.8}Se_{0.8}$ from our calculation and the comparison with the experimental data [125].

Fig. 8.5 shows the vibrational density of states of g-$Ge_{0.2}As_{0.4}Se_{0.4}$ and g-$AsGe_{0.8}Se_{0.8}$. At low frequency range E $<$ 15 meV. Our simulation gives the perfect agreement with experiment data. The A1 modes centered around 23 meV in these two glass models is also reproduced. Beyond 27 meV, the calculated VDOS of our model and the experimental results disagree. *The high frequency discrepancy is probably the fault of the Fireball confinement radius r_c. That is r_c was not "tuned" to reproduce the bond lengths to correctly give the spring constants.* Experimental results [125] indicated that the broadband below 20 meV of GeAsSe chalcogenide glasses is sensitive only to connectivity and not to network topology. The broadband is dominated by modes extending widely over the network and not by modes localized on robust "molecular" features in the glass. So, the clue for the discrepancy between experimental data and our simulation result is that our Hamiltonian does not describe the molecular-molecular interaction quite well. For the mode beyond 20 meV, the local SRO begins to matter. This experimental connection can be seen from the IPR analysis of vibrational modes. We observed that for both two glass models, the modes below 20 meV are essentially extended state. However, the mode beyond 20 meV the modes begin to localize on some atom sites.

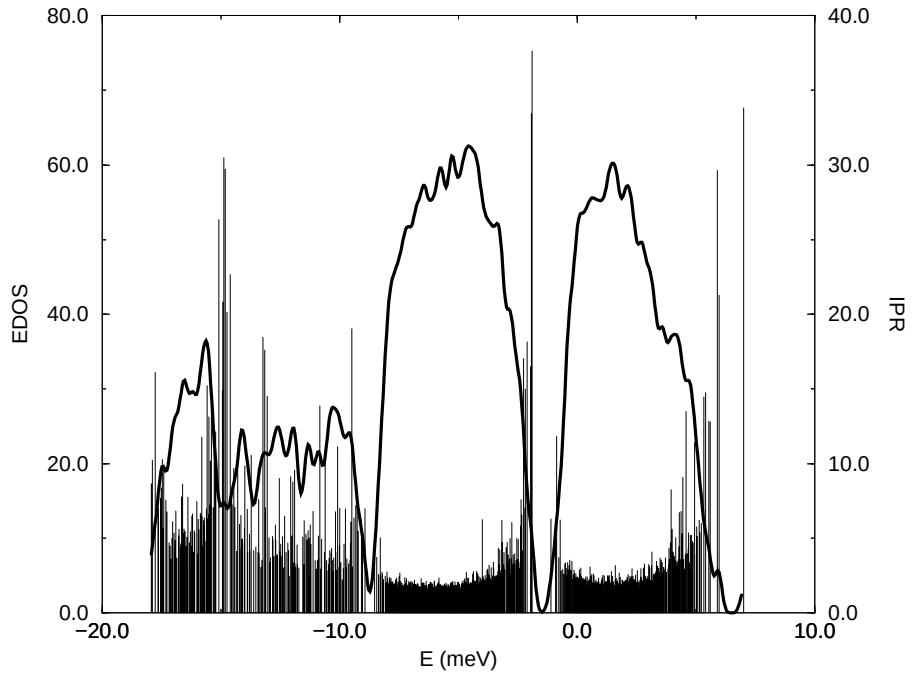

Figure 8.6: Electronic density of State(EDOS) and inverse participation ratio for the electronic eigenstate of g-$Ge_{0.2}As_{0.4}Se_{0.4}$. For the definition of the inverse participation ratio, see chap.2

8.5 Electronic Properties

Fig. 8.6 shows the electronic density of state of g-$Ge_{0.2}As_{0.4}Se_{0.4}$ and inverse participation ratio. The Γ-point band gap of our model is 0.8 eV. It is also noticeable that there are no states in this small band gap considering the number of topological defects in our model. The localization of our electronic eigenvalues are analyzed through the inverse participation ratio. Around the valence band edge, there are very localized states. We found that this is mainly due to undercoordinated As atoms. Considering the relatively low percentage of the two-fold coordinated As atoms, we think that undercoordinated As defect might be annealed away by slow, long and careful relaxation.

By inspecting the species-projected IPR (fig. 8.7), we can see that localization around -14.5 $\sim$ -18.0 eV is on Se atoms, -10.5 $\sim$ -14.5 eV is on As atoms and -9. $\sim$ -10.5 eV is on Ge atoms. Eigenstates of valence band peak between -2 $\sim$ -8 eV are quite extended, but as one approaches the valence band edge the eigenstates become increasingly localized. The undercoordinated As atoms contributed most part of localization of the conduction band edge and valence band edge.

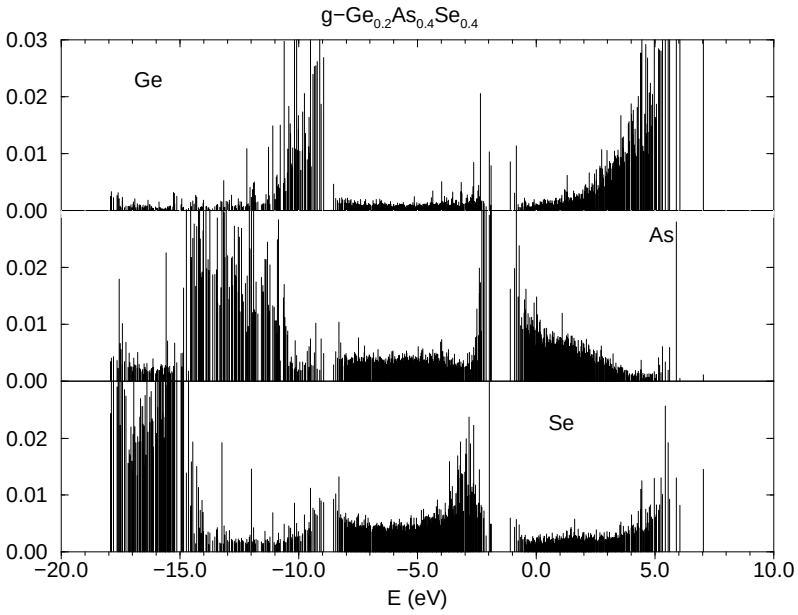

Figure 8.7: Species projected inverse participation of g-$Ge_{0.2}As_{0.4}Se_{0.4}$.

8.6 Discussion

8.6.1 Modeling Method

The method of modeling amorphous material from a sub-unit cell is not a new method. Ouyang and Ching [131] constructed the amorphous Si_3N_4 materials by systematic assemblage of a small number of fundamental building blocks. Some other researchers believe that this method can not provide satisfactory amorphous materials[132]. However, our method is different from their method in several aspects. First, the sub-unit cell was built truly from first principle. The bonding requirement for the sub-unit cell was satisfied by the arbitrary long *ab-initio* MD simulation. This means that the bonding of the atoms in the sub-unit cell does not necessarily satisfy the $8-n$ rule. This is very important for modeling chalcogenide glass materials since ample evidence suggested that normal bonding requirement for the elements in chalcogenide glass will not hold. We will discuss this point in next section in detail. Second, the unphysical correlation between the sub-unit cell was destroyed through the physical melting of the pseudo-crystal. From our simulation on the tertiary glass and other binary glasses such as g-$GeSe_2$, not only short range order but also intermediate range order of the glass is manifested in the liquid state. The melting procedure will significantly shorten the computation time compared to the method of searching the optimum structure from random configurations.

8.6.2 Structural properties

We have to admit that spectral weight of the structure factor S(Q) at low Q range and vibrational density of state at the mode greater than 20 meV do not agree with experiment very well. For the structure factor, the long range correlation will have some contribution on the spectral weight of the S(Q). This is shown by Nicolas et al.[128] that maximum correlation length $10\mathring{A}$ could not reproduce the FSDP totally for $g\text{-}Ge_{0.2}As_{0.4}Se_{0.4}$. We also do not exclude the possibility that a better Hamiltonian could improve this. However, our experience on modeling the a-Se structure indicated that better Hamiltonian shows very little effect on obtaining the better structure model of selenium. We expect that simulation time and size of the system is the key to get a good model.

An important finding in our calculation is that the average coordination for g-$Ge_{0.2}As_{0.4}Se_{0.4}$in our model is 2.86 which is very close to the coordination $\langle r \rangle = 2.8$ of the perfect glass for this model. The coordination for $AsGe_{0.8}Se_{0.8}$ is 3.04 which is close to the coordination $\langle r \rangle = 3.0$ of the perfect glass for this stoichiometric configuration. Experiment[125] indicated that vibrational mode below 20 meV is mainly determined by the average coordination number. Our model confirmed this experimental fact. More importantly, in our both glassy models, there is a fair number of overcoordinated Se sites and undercoordinated Ge sites. The overcoordinated Se sites are compensated by the undercoordinated Ge sites to give the

correct average coordination number. If we take a close look at the $GeSe_2$ theoretical model and experimental result, we will find this "compensation mechanism" in most chalcogenide glasses. Cobb and Drabold[88] found: 15% of Ge atoms in g-$GeSe_2$ are threefold coordinated; 20% of Se atoms are three-fold coordinated and 10% of Se atoms are one-fold coordinated. This gives the average coordinated number $\langle r \rangle = 2.683$ which is very close to the perfect coordination $\langle r \rangle$=2.667 for g-$GeSe_2$. Massobrio, Pasquarello and Car [109] simulated l-$GeSe_2$ by using plane wave based first principle MD simulation with GGA correction. In their calculation, 23% Se of atoms are three-fold coordinated and 30% of Ge atoms are undercoordinated. This roughly gives rise to the average coordination number $\langle r \rangle = 2.72$. Considering that more defects may appear in the liquid state, this coordination is also close to the perfect coordination number. All the result from g-$GeSe_2$ and our tertiary glass indicate one physical mechanism: valence alternation model is still valid in the binary and tertiary chalcogenide glasses.

Electrical resistivity measurements on chalcogenide glasses generally find that the Fermi energy is strongly pinned near mid-gap. Also, these materials are extremely difficult to dope. But this electronic evidence of a density of states in the gap is contradicted by magnetic measurements: ESR and magnetic susceptibility studies fail to find substantial numbers of free spins in the chalcogenides [1]. As we have already seen in the case of a-Se, these unusual properties could be explained by VAP model.

The VAPs model for the elementary chalcogen glass *a*-Se was essentially confirmed by theoretical calculation[29, 28] and experiment[8]. For the complex chalcogenide glass such as the tertiary glass we studied, it is not clear whether the VAP picture is still valid. The tertiary glasses we generated emerge naturally without any *a priori* information. All the structural properties agree with experiment. It turns out that the three-fold coordinated Se atoms and undercoordinated Ge atoms "seemingly" form the VAPs. This conclusions is further enhanced by the Mulliken charge analysis. We found that three-fold coordinated Se atoms bear the positive 0.1-0.2e charge while undercoordinated Ge atoms bear the negative charge around 0.2e. Here, we say they are "seemingly" VAPs is due to the fact that all the normally coordinated Se and Ge atoms are actually charged but with a less value. This indicated that overcoordinated Se atoms and undercoordinated Ge atoms are actually not defects. If this is true, any empirical modeling of these complex tertiary glass will doomed to be failed since normal switching and breaking algorithm will rely on the correct coordination number. In this sense, *ab-initio* calculation is the only way to build these complex glasses.

8.7 Summary

In this study, two tertiary chalcogenide glasses $Ge_{0.2}As_{0.4}Se_{0.4}$ and $AsGe_{0.8}Se_{0.8}$ were constructed by *ab initio* MD simulation. By judicious construction of short range

order in the initial model, we made the tertiary glass models with pair correlation function, structure factor simultaneously agree with experiment. The FSDP in the structure factor which indicates the intermediate range correlation emerges in our model naturally. We found that all the bonds in the tertiary glass model are saturated despite the abundance of overcoordinated Se atoms and undercoordinated Ge atoms. This is the first work to show that VAP model which explains the unusual property of chalcogenide glass such as no ESR signature, pinned Fermi energy still could play the most important role in the complex tertiary chalcogenide glasses.

Chapter 9

Concluding Remarks and Further Considerations

9.1 Summary

In this work, we have presented structural models of elementary chalcogenide amorphous material, *a*-Se, binary glassy surface, *g*-$GeSe_2$ surface and ternary amorphous materials *a*-$Ge_{0.2}As_{0.4}Se_{0.4}$. through *ab-inito* molecular dynamic simulation. *a*-Se model and *g*-$GeSe_2$ models are by far the best models yet presented through the *ab-inito* molecular dynamic simulation as evidenced by the uniform agreement with all the structural properties such as pair correlation function, static structure

factors, vibrational spectrum and electronic density of state. We made a first try on the ternary glassy $Ge_{0.2}As_{0.4}Se_{0.4}$ and obtained a reasonable structural model of this very complex ternary amorphous material. For the *a*-Se, we unambiguously show that valence alternation , i.e., negative U , is the major mechanism to explain the exotic properties of *a*-Se. For the *g*-$GeSe_2$ surface, we show that ring formation is the major mechanism for the surface reconstruction. Through defect analysis of the bulk *g*-$GeSe_2$, *g*-$GeSe_2$ surface, bulk $Ge_{0.2}As_{0.4}Se_{0.4}$, we show that more than 30% of defects in those model can still make electronic structure of those materials have no mid-gap states. We also show that valence alternation is the one of the possible mechanism for the nature to allow so many defects exist in the binary and ternary chalcogenide glasses.

Having the reliable structural models available, we are able to study how those chalcogenide glasses respond to light illumination from first principles. Using the 64- and 216-atom *a*-Se model we built, we show how light selectively attack the defect sites in the materials. We describe the bond switching and rearrangement by the photo-excitation and explain the physical mechanism of the photo-structural change. We also show the possibility of fine-tuning the structure of the a material through light excitation. We further link our MD simulation to the recent experiment by Kolobov et al. [8] to explain the physical mechanism of the dynamical bond formation observed experimentally.

9.2 Further Considerations

9.2.1 Modeling method

We discussed the method to build the amorphous materials. Through extensive simulation, we believe that the bottle-neck for MD simulation to get the credible structure model is that the time of the simulation can not match the time scale of nature to form those materials. But judicious selection of the initial structure from the *a priori* knowledge can expedite our search of a satisfactory model of amorphous material. But the method which we used to build the initial structure (selenium chain model from lattice random walk, a larger structure from the small unit cell) is somehow *ad hoc*. As we have discussed, some static algorithms such as WWW bond switching algorithm for constructing *a*-Si has some similarity between the algorithm used for solving NP hard problems in computer science. One obvious work is to extend the scope of WWW bond-switching scheme to the field of amorphous chalcogenide materials. Actually, the neighbour-hood structure which is the key for "local search" algorithm in computer science for selenium is very like the corresponding structure for TSP problem. The implementation of this idea is not very hard but the applicability of this idea needs to be tested by extensive simulations. Of course, if the Activation Relaxation Technique (ART) is implemented in the *ab*

initio simulation, "time scale problem" in the MD simulation is essentially overcome. This research is underway and we are working to obtain a good model for the the tertiary glassy material $Ge_{0.2}As_{0.4}Se_{0.4}$ through the combination of *ab initio* MD and ART technique.

9.2.2 Hamiltonian

Most crystalline chalcogenide materials belong to the category of molecular solids. We need the Hamiltonian which can describe the short range covalent force and long range *var der Walls* force equally well to model the chalcogenide materials. For the selenium, we made a first try on using the state of art *ab initio* MD code SIESTA to better describe the crystalline selenium and amorphous selenium. Although the gain on the structural properties of *a*-Se is very little by this new Hamiltonian, we can extend our research scope to describing the spin polarization of the defect sites. We still need to implement our light excitation method in the SIESTA to see how the structure will respond to the polarized light excitation. The vibrational density of state for our tertiary glassy model $Ge_{0.2}As_{0.4}Se_{0.4}$ does not agree with experimental data well at high frequency range. In that range, vibrational mode is probably sensitive to molecule-molecule interaction. Whether a better Hamiltonian could improve our model needs to be carefully studied.

9.2.3 VAP model for complex amorphous chalcogenide materials

We explicitly shows that VAP defect can explain most properties of elementary amorphous chalcogenide material, *a*-Se. We also see some evidence that VAP defect is also an important defect type in binary and tertiary chalcogenide materials. It is a very interesting question to study how the VAP defect behaves in complex amorphous chalcogenide materials. We want to use our *g*-$GeSe_2$ model and future *g*-$Ge_{0.2}As_{0.4}Se_{0.4}$ model to study this problem.

Bibliography

[1] Richard Zallen, *The Physics of Amorphous Solids*, John Willey % Sons Inc., 1983.

[2] F. Wooten, K. Winer and D. Weaire, Phys. Rev. Lett. **54**, 1392 (1985).

[3] G. T. Barkema and N. M. Mousseau, Phys. Rev. **B62**, 4985 (2000).

[4] N. E. Cusack, *The Physics of Structurally Disordered Matter,* IOP Publishing Ltd 1987.

[5] P. W. Anderson, Phys. Rev. Lett. **34**, 953 (1975);

[6] R. A. Street and N. F. Mott, Phys. Rev. Lett. **35** 1293 (1975).

[7] M. Kastner, D. Adler and H. Fritzsche, Phys. Rev. Lett. **37** 1504 (1976).

[8] A. V. Kolobov, M. Kondo, H. Oyanagi and A. Matsuda, Phys. Rev. B **58**, 12004,(1998); A.V. Kolobov, M. Kondo, H. Oyanagi, R. Durny, A. Matsuda and K. Tanaka, Phys. Rev. **B56**, R485 (1997).

[9] B. R. Djordjevic, M. F. Thorpe and and F. Wooten. Phys. Rev. **B52**, 5685 (1995).

[10] Yuhai Tu, J. Tersoff and G. Grinstein, Phys. Rev. Lett. **81**, 4899 (1998).

[11] Yuhai Tu, J. Tersoff, Phys. Rev. Lett. **84**, 4393 (2000).

[12] O. F. Sankey, T. Allen, Phys. Rev. B**33**, 7164 (1986).

[13] P. Vashishta, R. K. Kalia, J. P. Rino, and J. Ebbsjö, Phys. Rev. Lett **62**, 1651,(1989).

[14] P. Vashishta, R. K. Kalia, J. P. Rino, and J. Ebbsjö, Phys. Rev. B **41**, 12197,(1990).

[15] R. Car and M. Parrinello, Phys. Rev. Lett. **55**, 2471 (1985).

[16] P. Hohenberg and W. Kohn Phys. Rev. bf 136 864 (1964); W. Kohn and L. J. Sham, Phys. Rev bf 140 1133 (1965).

[17] L. H. Thomas L. H. Proc. Cambridge Phil. Soc. **23**, 542, (1927); E. Fermi Z. Phys. **48**, 73, (1928).

[18] W. H. Press, S. T. Teukolsky, W. T. Vetterling and B. P. Flannery, *Numerical Recipes in C*, Cambridge University Press.

[19] D. S. Johnson, L. A. Mcgeoch, in *Local Search in Combinational Optimization* ed. by Emile Aarts and J. K. Lenstra, John Wiley & Sons Inc.

[20] G. T. Barkema and N. Mousseau, Phys. Rev. Lett. **77** 4358 (1996); Comp. Sci. Eng. **1** 74 (1999).

[21] R. M. Martin, Phys. Rev. B **1** 4005 (1970).

[22] V. Poborchil, A. Kolobov and Ka. Tanaka, App. Phys. Lett. **74** 215 (1999).

[23] C. A. Spence and S. R. Elliott, Phys. Rev. B **39** 5452 (1989).

[24] H. Hisakuni and Ke. Tanaka, *Optical Microfabrication of chalcogenide glasses*, Science **270** 974 (1995).

[25] Ke. Tanaka, *Photoexpansion in As_2S_3 glass*, Phys. Rev. B **57** 5163 (1998); K. Tanaka and N. Yoshida, Sol. State Phen. **55** 153 (1997).

[26] For example, V. M. Lyubin and V. K. Tikhomihrov, J. Non. Cryst. Sol. **135** 37 (1991).

[27] Private Communication.

[28] Xiaodong Zhang and D. A. Drabold, J. Non. Cryst. Sol. (letter) **241** 195 (1998).

[29] Xiaodong Zhang and D. A. Drabold Phys. Rev. Lett. **83** 5042, 1999.

[30] Xiaodong Zhang and D. A. Drabold Int. J. Mod. Phys., (to be published)

[31] Xiaodong Zhang and D. A. Drabold, Phys. Rev. B, (to be published)

[32] Xiaodong Zhang and D. A. Drabold, unpublished.

[33] N. F. Mott *Electronic proceses in non crystalline materials* Oxford, Clarendon (1978).

[34] H. Fritzsche, Phil. Mag. B **68** 561 (1993).

[35] D. H. Vanderbilt and J. D. Joannopolous, *Theory of defect states in glassy Se*, Phys. Rev. B **22** 2927 (1980).

[36] S. R. Elliott, J. Non-Cryst. Sol **81** 71 (1986).

[37] Ke. Tanaka, Current Opinion in Solid State and Materials Sci. **1** 567 (1996).

[38] K. Shimakawa *et al* Adv. Phys. **44** 475 (1995).

[39] P. A. Fedders, Y. Fu and D. A. Drabold, Phys. Rev. Lett. **68** 1888 (1992).

[40] D. M. Ceperley and B. J. Alder. Phys. Rev. Lett., **45**, 566, (1980).

[41] J. P. Pedrew and K. Burke, Int. J. Quant. Chem. **57**, 309 (1996).

[42] J. P. Perdew. In P. Ziesche and H. Eschrig, editors, Electronic Structure of Solids. Akademie Verlag, Berlin, 1991.

[43] Martin Fuchs and Matthias Scheffler, Computer Physics Communications. **119** 67, (1999).

[44] D. R. Hamann Phys. Rev. **B40** 2980, (1989).

[45] N. Troullier, J. L. Martins Phys. Rev. **B43** 1993, (1991).

[46] Xiaodong Zhang and D. A. Drabold, Phys. Rev. B, submitted 10/00.

[47] P. Ordejon, D. A. Drabold, R, M. Martin, M. Grumbach, Phys. Rev. B **51** 1456 (1995), ibid. **48** 14646 (1993).

[48] F. Mauri, G. Galli and R. Car, Phys. Rev. B **47** 9973 (1993).

[49] N. Mazari and D. Vanderbilt, Phys. Rev. B **56** 12847 (1997).

[50] P. E. Maslen, C. Ochsenfeld, C. A. White, M. S. Lee and M. Head-Gordon, J. Phys, Chem A **102** 2215 (1998).

[51] W. Kohn, Phys. Rev. Lett. **76** 3168 (1996).

[52] X.-P. Li, R. W. Nunes, and D. Vanderbilt, Phys. Rev. B **47**, 10 891 (1993);

[53] M. Daw, Phys. Rev. B **47**, 10895.

[54] Gordon Baym *Lectures on Quantum Mechanics* The Benjamin/Cummings Publishing Company, Inc., p 424 (1969).

[55] E. M. Landau and L. P. Lifshitz, *Statistical Physics, part 1,* 3rd edition (Pergamon, New York) 1980.

[56] Stefan Goedecker, Rev. of Mod. Phys., **71** 1085, (1999).

[57] P. Ordejón, Comp. Mater. Sci. **12** 157 (1998).

[58] S. Ismail-Beigi and T. Arias, Phys. Rev. Lett. **82** 2127, (1999).

[59] J. W. Gibbs, Nature **59** pp 200 and 606 (1898-1899) quoted from R. Courant and D. Hilbert, *Methods of Mathematical Physics* Vol. 1, Wiley Interscience, New York, (1953), p. 105.

[60] J. des Cloizeaux, Phys. Rev. **135** A685 (1964); ibid. A698 (1964).

[61] W. Kohn Phys. Rev. **115** 809, (1959); W. Kohn Chem. Phys. Lett. **208** 167, (1993).

[62] W. Kohn Chem. Phys. Lett. **208** 167, (1993).

[63] U. Stephan and D. Drabold Phys. Rev. **B57** 6391, (1998).

[64] U. Stephan , R. M. Martin and D. Drabold Phys. Rev. **B62** 6885, (2000).

[65] G. T. Barkema and N. Mousseau, Phys. Rev. B **62** 4985 (2000); For electron states and localization: M. Durandurdu, D. A. Drabold, and N. Mousseau, ibid. 15307.

[66] J. J. Rehr and W. Kohn, Phys. Rev. B **10** 448 (1974).

[67] W. Kohn and J. R. Onffroy, Phys. Rev. B **8** 2495 (1973).

[68] R. G. Parr and W. Yang, *Density Functional Theory of Atoms and Molecules.* Oxford University Press, Oxford.

[69] http://www.plmsc.psu.edu/ www/matsc597c-1997

[70] T. Krügner and W. B. Holzapfel, Phys. Rev. Lett. **69**, 305 (1992).

[71] J. Mort, Physics Today **47**, 32 (1994).

[72] J. Rowlands and S. Kasap, Physics Today, **50**, 24 (1997).

[73] E.H. Henninger, R.C. Buschert and L. Heaton, J. Chem. Phys. **46**, 586 (1967).

[74] J. Robertson, Philos. Mag. **B51**, 183(1985).

[75] C. K. Wong, G. Lucovsky, and J. Bernholc, J. Non-Cryst. Solids bf 97&98, 1171(1987).

[76] R. Kaplow, T.A. Rowe and B.L. Averbach, Phys. Rev. **168**, 1068 (1968).

[77] M. Misawa and K. Suzuki, J. Phys. Soc. Jpn. **44**, 1612(1978).

[78] M. Misawa and K. Suzuki, J. Phys. Soc. Jpn. **44**,

[79] R. .A. Street, *Hydrogenated Amorphous Silicon.* Cambridge University Press p102. (1991).

[80] D. Hohl and R. O. Jones, Phys. Rev. B **43** 3856 (1991).

[81] R. Car and M. Parrinello, Phys. Rev. Lett. **55** 2471 (1985).

[82] C. Bichara, A. Pellegatti and J. -P. Gaspard, Phys. Rev. **49** 6581 (1994).

[83] A.A. Demkov, J. Ortega, O.F. Sankey and M. Grumbach, Phys. Rev. **52**, 1618 (1995).

[84] Otto F. Sankey, D.J. Niklewski, Phys. Rev. **B40**, 3979 (1989); Otto F. Sankey, D.A. Drabold and G.B. Adams, Bull. Am. Phys. Soc. **36**, 924 (1991).

[85] R. Bellissent, Nucl. Instr. and Meth. **199**, 289 (1982).

[86] F. Kirchhoff, G. Kresse and M.J. Gillan, Phys. Rev. **B57**, 10482 (1998); G. Kresse, F. Kirchoff and M. J. Gillan, Phys. Rev. B **59** 3501 (1999) and references therein.

[87] E.H. Henninger, R.C. Buschert and L. Heaton, J. Chem. Phys. **46**, 586 (1967).

[88] M. Cobb and D. A. Drabold, Phys. Rev. B **56** 3054 (1997), ibid **54** 12162 (1996).

[89] D. A. Drabold, P. A. Fedders, S. Klemm and O. F. Sankey, Phys. Rev. Lett. **67** 2179 (1991).

[90] P. Stumm and D. A. Drabold, Phys. Rev. Lett. **79** 677 (1997).

[91] P. Stumm, D. A. Drabold and P. A. Fedders, J. App. Phys. **81** 1289 (1997).

[92] Attila Szabo and Neil S. Ostlund, *Modern Quantum Chemistry* (McGraw-Hill, New York, 1989), p.151.

[93] P. Ordejón *et al.* Phys. Rev. B **53** R10441 (1996); D. Sanchez-Portal *et al* Int. J. Quant. Chem. **65** 453 (1997).

[94] P. Ordejón *et al.* Phys. Stat. Sol. **217** b, 335 (2000).

[95] Masanori Inui, Kenji Maruyama, Shinícchi Takeda, Shigeru Tamaki and Yoshio Waseda, Journal of the Physical Society of Japan. **63**, 1378 (1994).

[96] W. Wei, B. W. Corb and B. L. Averbach, J. Non-Crystalline Solids **53**, 19 (1982).

[97] O. F. Sankey (unpublished).

[98] Kamitakahara et al., private communication.

[99] W. A. Phillips, U. Buchenau, N. Nücker, A. -J. Dianoux, and W. Petry, Phys. Rev. Lett. **63**, 2381(1989).

[100] D. A. Drabold and F. A. Fedder, Phys. Rev. B Rapid (in press).

[101] G. Kresse, J. Furthmüller, and J. Hafner, Phys. Rev. B **50**, 13181 (1994).

[102] F. Mauri and R. Car, Phys. Rev. Lett. **75** 3166 (1995); J. Song *et al*, phys. Rev. B **53** 8042 (1996); O. Pankratov and M. Scheffler, Phys. Rev. Lett. **71**, 2797 (1993); For transport, G. Galli *et al.* Phys. Rev. Lett. **42** 7470 (1990)

[103] B. W. Corb , W. D. Wei and B. L. Averbach, J. Non-Crystalline Solids **53**, 29 (1982).

[104] We promoted either one or two electrons from the HOMO level; relaxations were similar. We report the two electron case here. The single electron promotion is probably best handled at LSDA level.

[105] For example, B. Delley, "DMol, a Standard Tool for Density Funct ional Calculations: Review and Advances". In J. M. Seminario and P. Politzer, eds., "Modern Density Functional Theory: A Tool for Chemistry", vol. 2 of Theoretical and Computational Chemistry, Amsterdam, 1995. Elsevier Science Publ.

[106] D. A. Drabold, S. Nakhmanson, Xiaodong Zhang in *Properties and applications of amorphous materials*, Ed. by M. F. Thorpe and L. Tichy, NATO ASI Series, Kluwer, Dordrecht (to be published, 2001).

[107] K. M. Kandil et al., Phys. Rev. B **51**, 17565,(1995).

[108] P. Boolchand, J. Grothaus, W. J. Bresser, and P. Suranyi, Phys. Rev. B **25**, 2975,(1982).

[109] C. Massobrio, A. Pasquarello, and R. Car, Phys. Rev. Lett. **80**, 2342, (1998).

[110] I. Petri, P. S. Salmon and H. E. Fischer, Phys. Rev. Lett. **84**, 2413, (2000).

[111] See for example, P. Boolchand in "Insulating and semiconducting glasses", World Scientific, Singapore (2000). p 191, especially section 4.1

[112] S. Ovshinsky in "Insulating and semiconducting glasses", World Scientific, Singapore (2000). p 729.

[113] I. T. Penfold and P. S. Salmon, Phys. Rev. Lett. **67**, 97, (1991).

[114] T. E. Faber and J. M. Ziman, Phil. Mag. **11**, 153,(1965).

[115] A. Bhatia and D. Thornton, Phys. Rev. B **2**, 3004,(1970)

[116] K. S. Krishnan and A. Bhatia, Proc. Nat. Acad. Sci. india **14**, 154,(1944)

[117] C. Massobrio, A. Pasquarello and R. Car, Comp. Mats. Sci. **17** 115 (2000).

[118] O. F. Sankey, A. A. Demkov, W. Windl, J. H. Fritsch, J. P. Lewis, and M. Fuentes-Cabrera, Int. Journ. of Quant. Chem. **69**, 327 (1998).

[119] For a recent discussion, S. R. Elliott, Phys. Rev. Lett. **67** 711 (1991); S. R. Elliot, Nature **354** 445 (1991).

[120] S. Susman et al., J. Non-Cryst. Solids **125**, 168 (1990).

[121] Jianjun Dong, and D. A. Drabold Phys. Rev. B **57**, 15591,(1998)

[122] C. A. Davis, K. M. Knowles, and G. A. J. Amaratunga, Suf Coat. Technol. **76-77**. 316,1995.

[123] J. Dong and D. A. Drabold, Phys. Rev. Lett. **80**, 1928, 1998.

[124] Z. U. Borisova, Glassy Semiconductors Plenum, New York (1981).

[125] B. Effey and R. L. Cappelletti, Phys. Rev. B 59 4119 (1999).

[126] P. Hari et al J. Non-Cryst. Sol. 200 736 (1996).

[127] J. Li, D. A. Drabold , Phys. Rev. B, (2000)

[128] N. de la Rosa et al, Phys. Rev. B 33 4094 (1986).

[129] G. N. Greaves and E. A. Davis, Philos. Mag. **29**, 1201 (1974).

[130] X. Wyckoff, in *Crystal Structure* (Wiley, New York, 1963).

[131] L. Ouyang and W. .Y. Ching, Phys. Rev. **B54**, R15594 (1996).

[132] N. Mousseau, Phys. Rev. B **56**, 14190 (1997).

[133] For example, O. Gerben and L. Pusztai, Phys. Rev. B 50 14136 (1994).

Appendix A

Publications directly and indirectly from this work

(1) Xiaodong Zhang and David Drabold, *Evidence for valence alternation and new model for amorphous Selenium,* J. Non. Cryst. Sol. 241 195. (Letter to the Editor). Nov. 11, 1998. [chapter 5]

(2) Xiaodong Zhang and David Drabold, *ab-initio* simulation of photo-structural change in amorphous selenium,Phys. Rev. Lett. **83**, 5042 (1999). [chapter 6]

(3) Xiaodong Zhang and David Drabold, Simulation of the response of amorphous selenium to light, to be published in Int. J. Mod. Phys. B. [chapter 6]

(4) Xiaodong Zhang and David Drabold, *Structural and electronic properties of amorphous $GeSe_2$ surfaces,* Phys. Rev. B **61**, 15695, 2000. [chapter 7]

(5) D. A. Drabold, S. Nakhmanson and Xiaodong Zhang, *Electronic structure of amorphous insulators and photostructural effects in chalcogenide glasses,* NATO ASI proceedings, M. Thorpe and L. Tichy, Eds., Kluwer (2000). [chapter 5,6]

(6) Xiaodong Zhang and David Drabold, *Properties of the density matrix from realistic calculations,*, Phys. Rev. B, submitted. [chapter 3]

(7) A. A. Demkov, Xiaodong Zhang and David Drabold, *First principle simulation and current-voltage characteristic of atomistic metal-oxide-semiconductor structures,* Phys. Rev. Lett, submitted

(8) A.A. Demkov, R. Liu, Xiaodong Zhang and Heater Loechelt, *Theoretical and experimental investigation of ultra-thin oxynitrides and the role of nitrogen at the Si-SiO_2 interface.*, J. Vac. Sci. Technol B **18:** 2388,2000.

(9) A.A. Demkov, Xiaodong Zhang and Heater Loechelt, *Theoretical investigation of ultrathin gate dielectrics,* VLSI Design, (to be published)

(10) A. A. Demkov, Xiaodong Zhang *Theoretical investigation of gate dielectrics* Proceedings of the 27th International symposium on Compound Semiconductors. (to be published)